Structural and electronic properties of transition metal nanoalloys and magnetic compounds

Genehmigte Abhandlung
zur Erlangung des akademischen Grades
eines Doktors der Naturwissenschaften (Dr. rer. nat.)
im Promotionsprogramm
Physik Weicher Materie, Nichtlineare Dynamik und Festkörperphysik
der Bayreuther Graduiertenschule für Mathematik und Naturwissenschaften

von
Linn Leppert
geboren in Chemnitz

1. Gutachter: Prof. Dr. Stephan Kümmel
2. Gutachter: Prof. Dr. Matthias Schmidt
3. Gutachter: Prof. Dr. Paul-Gerhard Reinhard

Tag der Einreichung: 28. Mai 2013
Tag des Kolloqiums: 5. September 2013

I might be wrong
I could have sworn
I saw a light coming on
(Radiohead)

Abstract

In transition metal clusters, potentially profitable technological applications and fascinating fundamental questions are closely connected. Bimetallic nanoalloys, e.g., have become increasingly popular as their performance in catalysis is often superior to their pure counterparts. Exemplary for this are gold-platinum (Au-Pt) nanoalloys that have been used as highly potent catalysts in electrocatalysis and in a variety of oxidation reactions. However, the mere existence of Au-Pt nanoalloys is astonishing, as Au and Pt cannot be mixed in bulk over a wide range of compositions. Furthermore, how a combination of Au and Pt in nanoalloys results in their special properties has not yet been determined conclusively.

It has been shown in empirical simulations and first-principles density functional theory (DFT) calculations that Au-Pt nanoalloys preferably arrange in a core-shell mixing pattern with Au forming a shell around a Pt core. This is in contradiction to many experimental studies that report the formation of solid solutions of Au and Pt. In the present work, this seeming discrepancy is addressed by simulating x-ray diffraction patterns that are experimentally used to characterize nanoalloys. It is shown that the interpretation of the diffraction patterns relies on questionable assumptions and therefore does not suffice as a definite characterization tool for Au-Pt nanoalloys.

To shed light on the special catalytic properties of Au-Pt nanoalloys under rather different experimental conditions, a thorough investigation of their electronic and structural properties has been carried out. It is found that features favorable for catalysis in Au-Pt nanoalloys emerge as a consequence of combining two fundamental properties: Pt contributes a high density of states close to the Fermi level, which promotes chemical activity. Au increases the structural flexibility of the Au-Pt system, which might be beneficial for the formation of active and element-specific binding sites as well as regeneration of the catalyst after the reaction.

Although DFT offers an attractive compromise between computational effort and accuracy for a theoretical description of Au-Pt nanoalloys, other transition metal compounds severely challenge existing DFT approximations. Manganese (Mn) doped silicon (Si) clusters represent an ideal model system to study the interaction of a single magnetic impurity with a semiconducting host both experimentally and theoretically. The transition from exohedral (lowly coordinated) to endohedral (highly coordinated) doping that occurs for Si clusters with more than ten atoms, is accompanied by complete quenching of the magnetic moment of Mn. We show that $MnSi_{11}^{+}$, the smallest endohedral cluster found in experiment, suffers strongly from a well-known general problem of most DFT approximations: the self-interaction error. Finally, a universal correlation between magnetic moment and the coordination of the Mn dopant is established that can be generalized to extended systems and suggests a route to stabilize the magnetic moment of bulk Mn-Si compounds.

Kurzdarstellung

In Übergangsmetallclustern liegen gewinnbringende technische Anwendungen und fundamentale Fragen oftmals nah beieinander. Dimetallische Nanolegierungen erfreuen sich beispielsweise großer Beliebtheit, weil sie in diversen katalytischen Reaktionen den entsprech-enden reinen Metallen überlegen sind. Gold-Platin (Au-Pt) Nanolegierungen wurden als äußerst wirksame Katalysatoren in der Elektrokatalyse und für eine Reihe von Oxidationsreaktionen identifiziert. Genau genommen ist jedoch die bloße Existenz dieser Nanolegierungen erstaunlich, da Au und Pt in ausgedehnten Systemen kaum mischbar sind. Bislang ist zudem nicht klar, auf welche Weise eine Kombination von Au und Pt in einer Nanolegierung zu speziellen Eigenschaften führt.

In empirischen Simulationen und nicht-empirischen Dichtefunktionaltheorie (DFT) Rechnungen konnte gezeigt werden, dass Au-Pt Nanolegierungen ein $\mathrm{Au}_{\mathrm{Schale}}\mathrm{Pt}_{\mathrm{Kern}}$ Mischungsmuster bevorzugen. Dies steht im Widerspruch zu experimentellen Studien, in denen homogen gemischte Cluster beobachtet wurden. In der vorliegenden Arbeit wird diese scheinbare Diskrepanz durch Simulation von Röntgenbeugungsmustern untersucht. Es wird gezeigt, dass die übliche Auswertung dieser Beugungsmuster auf mehrdeutigen Annahmen beruht und somit nicht zur alleinigen Charakterisierung von Au-Pt Nanolegierungen ausreicht.

Um Aufschluss über die hohe katalytische Aktivität von Au-Pt Nanolegierungen zu erlangen, wurden ihre elektronischen und strukturellen Eigenschaften untersucht. Es wird gezeigt, dass sich die günstigen Eigenschaften von Au-Pt Nanolegierungen als Konsequenz der Kombination zweier fundamentaler Eigenschaften ergeben können: Pt trägt zu einer hohen Zustandsdichte am Ferminiveau bei, welche förderlich für die chemische Aktivität sein kann. Mit steigendem Au-Anteil steigt wiederum die strukturelle Flexibilität der Au-Pt Systeme. Dies kann für die Bildung aktiver und elementspezifischer Katalysezentren sowie zur Regeneration des Katalysators nach der Reaktion von Nutzen sein.

DFT bietet für die Behandlung von Au-Pt Nanolegierungen einen guten Kompromiss zwischen rechnerischem Aufwand und Genauigkeit. Im zweiten Teil dieser Arbeit geht es jedoch um eine andere Übergangsmetallverbindung, welche existierende Näherungen der DFT auf eine harte Probe stellt. Siliziumcluster (Si) dotiert mit einem einzelnen Manganatom (Mn) sind ein ideales Modellsystem um die Frage zu untersuchen, wie eine magnetische Verunreinigung mit einem halbleitenden Wirtsmaterial wechselwirkt. Der Übergang von exohedraler (niedrige Koordination) zu endohedraler (hohe Koordination) Dotierung findet für Cluster mit mehr als zehn Si-Atomen statt und wird von einer kompletten Auslöschung des magnetischen Moments begleitet. In dieser Arbeit wird gezeigt, dass MnSi_{11}^{+}, der kleinste experimentell identifizierte endohedrale Cluster, besonders stark unter einem wohlbekannten Problem vieler DFT Näherungen leidet: dem Selbstwechselwirkungsfehler. Abschließend wird ein universeller Zusammenhang zwischen dem magnetischen Moment und der Koordination des Mn-Dotieratoms gezeigt, der auch auf Festkörpersysteme übertragen werden kann. Dieser Zusammenhang eröffnet die Möglichkeit das magnetische Moment von ausgedehnten Mn-Si Verbindungen zu stabilisieren.

Contents

1

Introduction

It seems to be pure understatement that the elements at the center of the periodic table are called transition elements or, even more modestly, subgroup elements. All transition elements are metallic in the bulk, exhibit rich physical and chemical properties and have been used for tool, weapon and jewelry manufacturing for thousands of years. Among many other fascinating features such as the nobility of copper, silver and gold, transition metals possess unique catalytic and magnetic properties both as free ions and in the bulk.

In between atomic physics and solid state physics lies the regime of cluster physics. Clusters have been called "strange morsels of matter" [1] to point out their unusual electronic, magnetic and optical properties that often change discontinuously upon going from very small systems consisting of not more than three atoms to clusters containing thousands of atoms that can already be considered to behave bulk-like in some respects. These special features emerge as a consequence of two basic effects. Firstly, in clusters or nanoparticles (NP) a larger fraction of the atoms can occupy positions at the surface as compared to extended systems. Secondly, the small size of clusters directly influences the electronic structure by quantum confinement. The electronic structure of small gold (Au) clusters can, e.g., be described remarkably well by delocalized states in an electron-in-a-box model [2].

Transition metal clusters are a particularly interesting field of study and much research activity has been devoted to exploring their fundamental and often technologically useful properties. Fig. 1.1 shows a table of those elements that belong to the class of transition metals. A general and slightly more restrictive definition states that the free transition element atoms possess an incomplete d-shell in the ground state or in excited states of small energy [3]. For our purposes the overview that Fig. 1.1 provides shall be sufficient. In the following paragraphs the unusual properties of transition metal clusters are illustrated using two examples: the high catalytic activity of small Au clusters and the size-dependence of spin and orbital moments of free $3d$ transition metal clusters.

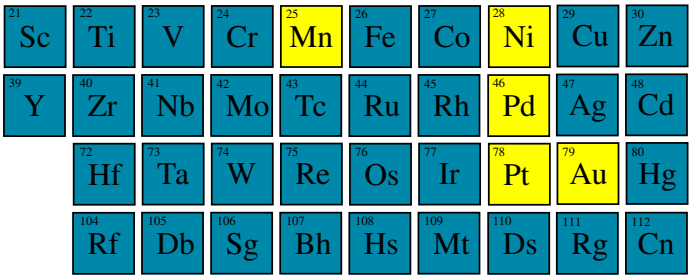

Figure 1.1: The periodic table of the transition metal elements. The elements marked in yellow, Mn, Ni, Pd, Pt and Au are relevant for the present work. Their rich electronic structure featuring open $3d$ and $5d$ shells manifests itself, e.g., in special catalytic and magnetic properties.

Au is best known as a noble, but ductile metal, well suited for the use as coin or jewelry. This view, however, only applies to smooth Au surfaces and large ($> 10\,\text{nm}$) Au particles. In 1987 the pioneering work of Masatake Haruta showed that both highly dispersed Au particles and scratched Au surfaces exhibit high catalytic activity in a variety of industrially important reactions [4]. In the original work it was shown that Au NP catalyze the oxidation of carbon monoxide at temperatures below $0\,^{\circ}\text{C}$ [5]. This discovery was followed by a scientific "gold rush" and an ongoing quest for further catalytically active nanomaterials [2, 6]. Haruta's Au particles had a diameter of $\approx 5\,\text{nm}$. It was later observed by Sanchez et al. that also very small Au clusters are catalytically active and that the smallest catalytically active NP is Au_8 [7]. The influence of the support [8] and the NP's structure [9] on the catalytic activity have been studied intensively. In the past years Au has become less expensive than other catalysts used in large scale technological processes such as palladium (Pd) or platinum (Pt). A pointed statement of A. Stephen K. Hashmi illustrates the growing significance of Au NP for catalysis: "Overall, a change of paradigm has taken place. While the ancient alchemists investigated the question of how to make gold, now the question is what to make with gold." [10]

The strict definition above characterizes a transition element by having an open d-shell. Consequently, as free atoms, most transition elements carry a spin- and an orbital magnetic moment. The size of this moment can (assuming only one incomplete subshell) be estimated using *Hund's rules*. The $3d$ elements iron (Fe), cobalt (Co) and nickel (Ni), e.g., have in compliance with Hund's first rule electronic valence configurations of $4s^2 3d^6$, $4s^2 3d^7$ and $4s^2 3d^8$, resulting in $4\,\mu_B$, $3\,\mu_B$ and $2\,\mu_B$ spin magnetic moments and $2\,\mu_B$, $3\,\mu_B$ and $3\,\mu_B$ orbital magnetic moments, respectively. In the bulk Fe, Co and Ni are the commonly known elements that exhibit ferromagnetic order at room temperature. The magnetic moment of these systems arises almost entirely from the electron spins, as the orbital magnetic moment is quenched due to the symmetry of the crystal lattice. The question of how the orbital and spin magnetic moment as well as magnetic order phenomena develop upon going from single atoms to the bulk is of fundamental interest and another typical example for the unusual properties of transition metal clusters. Fe, Co and Ni clusters have been investigated using Stern-Gerlach deflection experiments for clusters consisting of up to 700 atoms and it has been found that even clusters with several hundreds of atoms still carry larger magnetic moments than the corresponding bulk [11, 12]. Yet smaller, size-selected Fe clusters have been studied using x-ray circular dichroism spectroscopy (XMCD). This technique allows to obtain information about spin and orbital magnetic moments separately and showed that the orbital magnetic moment in free Fe clusters is strongly quenched even for very small clusters [13]. The size-dependence of spin and orbital magnetic moments of

Fe clusters exemplifies that the transition to bulk-like behavior very much depends on the property of interest.

In the present work the elements marked in yellow in Fig. 1.1 will be brought into focus. The main two parts of this thesis are concerned with the structural and electronic properties of Au-Pt and Au-Pd nanoalloys and of manganese (Mn) doped silicon (Si) clusters. Au-Pt(Pd) nanoalloys have special qualities that make them attractive for their use as catalysts. Mn doped Si clusters, on the other hand, represent a system with interesting magnetic properties. Most results presented in this thesis stem from density functional theory (DFT) calculations, a method that offers an excellent trade-off between computational cost and accuracy. Following a discussion of the basic principles of ground state DFT, important approximations to it and some of its exact properties, I present computational methods relevant for this work in Chapter 2. Subject of Chapter 3 are the structural and electronic properties of binary Au-Pt and Au-Pd clusters, also called nanoalloys or NP in the following. The theoretical description of $3d$ transition metal compounds and the correct prediction of magnetic moments is a challenge for existing approximations to DFT. This point is illustrated in Chapter 4 by a study of the magnetic-to-nonmagnetic transition that has experimentally been observed in small Si clusters doped with a single Mn impurity. Chapter 5 summarizes the results and gives an outlook to Ni-Pd NP, the all-rounder transition metal nanoalloy, as this system combines high catalytic activity with interesting magnetic properties. Finally, three appendices are attached to this work in which the effects of a finite temperature and of the NP interaction with a support material on electronic and structural properties of Au-Pt nanoalloys, their optical absorption spectra simulated within Mie theory and computational and technical details are discussed.

2

Theoretical and technical framework

Most of the results presented in this thesis rely on calculations using DFT in conjunction with a variety of computational methods, such as pseudopotentials and several geometry optimization schemes to determine ground state geometries or transition states. The following pages therefore give a short introduction to DFT and the approximations used in typical DFT calculations. Furthermore, the physical meaning of the Kohn-Sham (KS) and generalized Kohn-Sham (GKS) eigenvalues, as the main output from such calculations, is discussed. Three different schemes for the generation of pseudopotentials are presented in Sec. 2.4. Finally, in Sec. 2.5, I discuss two methods for global geometry optimization and one for the determination of transition states.

2.1 Foundations of Density Functional Theory

When Walter Kohn received the Nobel Prize for chemistry in 1998 for the development of DFT he said: "In my view DFT makes two kinds of contributions to the science of multiparticle quantum systems [...]. The first is in the area of fundamental understanding [...]. The second contribution is practical." [14]. In fact, it is mostly this practicability that has made DFT a standard tool in chemistry and physics for calculating, e.g., binding energies of molecules and clusters or the band structure of solids.

The foundations of DFT were laid in 1964 by Hohenberg and Kohn in their seminal paper [15], in which they proved that the ground state electron density $n(\boldsymbol{r})$ can serve as a basic variable containing all information about an N-electron system. The Hamiltonian of a stationary system of such interacting electrons has the form $\hat{H} = \hat{T} + \hat{V}_{\text{ext}} + \hat{W}$, where $\hat{T} = \sum_{i=1}^{N} \hat{p}_i^2/2m$ is the kinetic energy operator, $\hat{V}_{\text{ext}} = \sum_{i=1}^{N} v_{\text{ext}}(\hat{r}_i)$ characterizes

the interaction of the electrons with all external potentials and $\hat{W} = \sum_{i<j} w(\hat{r}_i, \hat{r}_j)$ is the electron-electron interaction.

The Hohenberg-Kohn theorem can be subsumed in two statements: First, for a given electron-electron interaction $\hat{W}$ there is a one-to-one mapping between the external potential v_{ext} (up to a physically irrelevant constant), the (non-degenerate) ground state $|\psi_0\rangle$ resulting from Schrödinger's equation $\hat{H}|\psi_0\rangle = E_0|\psi_0\rangle$ and the ground state density $n(\boldsymbol{r})$. $|\psi_0\rangle$ is a unique functional of the ground state density, hence every ground state observable, and in particular the ground state energy, is a density functional, too. Second, using the Raleigh-Ritz variational principle one can obtain the exact ground state density and energy corresponding to v_{ext} by minimizing the energy functional

$$E[n] = F[n] + \int v_{\text{ext}}(\boldsymbol{r}) n(\boldsymbol{r}) d^3r. \tag{2.1}$$

$F[n] = \langle\psi[n]|\hat{T} + \hat{W}|\psi[n]\rangle$ is a universal functional, i.e., it is independent of $v_{\text{ext}}(\boldsymbol{r})$. This provides a simple and exact reformulation of Schrödinger's equation. However, as Hohenberg and Kohn noted already in 1964 [15]: "The major part of the complexities of the many-electron problem are associated with the determination of the universal functional $F[n]$."

The most successful approach to determine $F[n]$ was proposed in 1965 by Kohn and Sham [16], who reformulated the energy functional of a system of N interacting electrons as

$$E[n] = T_{\text{s}}[n] + E_{\text{H}}[n] + E_{\text{ext}}[n] + E_{\text{xc}}[n], \tag{2.2}$$

where $T_{\text{s}}[n]$ is the kinetic energy of a system of N non-interacting electrons. $E_{\text{H}}[n]$ is the classical electrostatic Hartree energy

$$E_{\text{H}} = \frac{e^2}{2} \int\int \frac{n(\boldsymbol{r}) n(\boldsymbol{r}')}{|\boldsymbol{r} - \boldsymbol{r}'|} d^3r d^3r' \tag{2.3}$$

and $E_{\text{ext}}[n]$ describes the interaction between the electrons and the external potential

$$E_{\text{ext}}[n] = \int v_{\text{ext}}(\boldsymbol{r}) n(\boldsymbol{r}) d^3r. \tag{2.4}$$

$E_{\text{xc}}[n]$, the *exchange-correlation* (xc) energy functional, is defined as consisting of every contribution not treated by E_{H} and T_{s}, i.e.,

$$E_{\text{xc}} = T - T_{\text{s}} + W - E_{\text{H}}. \tag{2.5}$$

Here, T is the full kinetic energy of the interacting electron system and W is the electron-electron interaction energy. Minimization of Eq. (2.2) with respect to n_σ, the total spin density, and comparison with the corresponding term for a system of N non-interacting electrons leads to the same ground state density if the N non-interacting electrons are subject to an effective, local, multiplicative potential

$$v_\sigma^{\text{KS}}(\boldsymbol{r}) = v_{\text{ext}}(\boldsymbol{r}) + v_{\text{H}}(\boldsymbol{r}) + v_{\text{xc},\sigma}(\boldsymbol{r}), \tag{2.6}$$

in which v_{H} is the Hartree potential $v_{\text{H}} = e^2 \int n(\boldsymbol{r}')/|\boldsymbol{r} - \boldsymbol{r}'| d^3r'$ and $v_{\text{xc},\sigma} = \delta E_{\text{xc}}/\delta n_\sigma$ the xc potential. Eq. (2.6) defines the so-called KS potential. Regarding the question of

whether such a potential exists for all densities (*v-representability* problem) the reader is referred to Ref. [17] and references therein. In most practically relevant cases the density is v-representable. This means that one can calculate the ground state density $n(\boldsymbol{r})$ of the many-electron system in an external potential $v_{\text{ext}}(\boldsymbol{r})$ by solving the Schrödinger-like one-particle equations

$$\left(-\frac{\hbar^2}{2m}\nabla^2 + v_\sigma^{\text{KS}}(\boldsymbol{r})\right)\varphi_{i\sigma}(\boldsymbol{r}) = \varepsilon_{i\sigma}\varphi_{i\sigma}(\boldsymbol{r}), \tag{2.7}$$

and summing over all occupied KS orbitals, $\varphi_{i\sigma}(\boldsymbol{r})$,

$$n(\boldsymbol{r}) = \sum_{\sigma=\uparrow,\downarrow} n_\sigma(\boldsymbol{r}) = \sum_{\sigma=\uparrow,\downarrow}\sum_{i=1}^{N_\sigma} f_{i\sigma}|\varphi_{i\sigma}(\boldsymbol{r})|^2. \tag{2.8}$$

The sum over all occupation numbers $f_{i\sigma}$ yields the total number of electrons

$$\sum_{\sigma=\uparrow,\downarrow}\sum_{i=1}^{N_\sigma} f_{i\sigma} = N. \tag{2.9}$$

Equations (2.6) – (2.8) constitute the KS equations, that have to be solved self-consistently in most practical applications of DFT.

The KS equations are in principle an exact reformulation of the full interacting many-body problem of quantum mechanics. However, all exchange and correlation effects that go beyond the Hartree energy E_{H} and the non-interacting kinetic energy T_{s} are by definition (Eq. (2.5)) included in the xc energy E_{xc}, which is in general not known exactly. The most important approximations to E_{xc} are discussed in the following section.

2.2 Exchange-correlation energy functionals

Approximations to the xc energy functional can roughly be divided into two groups: explicit and implicit density functionals. Commonly used functional approximations of the first kind are the *local density approximation* (LDA) and the *generalized gradient approximation* (GGA). Functionals of the second group do not explicitly depend on the density but on the orbitals, i.e., they possess an implicit dependence on the electron density by virtue of the Hohenberg-Kohn theorem. Prominent examples are so-called hybrid functionals and range-separated hybrid (RSH) functionals, meta-GGAs as well as the self-interaction correction (SIC). A thorough discussion of the properties and limits of all functionals is beyond the scope of this thesis. A comprehensive overview can be found in Ref. [18] and references therein. Relevant approximations for the present work are described in the following.

The LDA[1] is one of the most often used approximations to E_{xc} and was introduced already by Hohenberg and Kohn [15]. It is based on the simple idea that in a system in which the electron density varies only slowly in space, e_{xc}, the xc energy per electron, is approximately equal to $e_{\mathrm{xc}}^{\mathrm{hom}}$ in the homogeneous electron gas. One then obtains E_{xc} by integration of e_{xc} over space. The exchange contribution is exactly known to be

$$E_x^{\mathrm{LDA}}[n] = -\frac{3e^2}{4}\left(\frac{3}{\pi}\right)^{1/3}\int n(\boldsymbol{r})^{4/3}d^3r. \tag{2.10}$$

The correlation part has been computed with high accuracy using Monte-Carlo methods [19]. Many widely used LDA energy functionals, e.g., the ones by Vosko, Wilke and Nusair [20], Perdew and Zunger [21] and Perdew and Wang [22], are based on parametrizations of these early Monte-Carlo calculations extended by known limits and scaling laws derived from the exact E_c^{hom}. The large number of systems for which the LDA leads to qualitatively reasonable results[2] is surprising taking into account that for most systems the assumption of a nearly homogeneous electron density is an oversimplification. This can be rationalized by introducing the concept of the xc hole $n_{\mathrm{xc}}(\boldsymbol{r},\boldsymbol{r}') = \rho_2(\boldsymbol{r},\boldsymbol{r}')/n(\boldsymbol{r}) - n(\boldsymbol{r}')$ with $\rho_2(\boldsymbol{r},\boldsymbol{r}')$ representing the electron pair density. The xc hole has to obey the sum rule

$$\int n_{\mathrm{xc}}(\boldsymbol{r},\boldsymbol{r}')d^3r = -1. \tag{2.11}$$

The LDA's xc hole satisfies Eq. (2.11) even in rather inhomogeneous situations [23]. This leads to a subtle error cancellation between the exchange and the correlation part of $E_{\mathrm{xc}}^{\mathrm{LDA}}$.

A systematic way to improve on the LDA is to include not only information about the electron density at each point $\boldsymbol{r}$, but also on the rate of its spatial variation. Such GGA functionals have the form

$$E_{\mathrm{xc}}^{\mathrm{GGA}}[n] = \int f(n(\boldsymbol{r}), \nabla n(\boldsymbol{r}))d^3r. \tag{2.12}$$

The function $f(n(\boldsymbol{r}), \nabla n(\boldsymbol{r}))$ is constructed either by trying to satisfy as many exact constraints of the exact xc energy functional as possible (leading, e.g., to one of the most popular GGAs of Perdew, Burke and Ernzerhof (PBE) [24] or by fitting to large sets of test molecules (e.g., BLYP, consisting of the exchange functional of Becke [25] and the correlation functional of Lee, Yang and Parr [26]).

Although the LDA and the GGA perform satisfactorily in many practical calculations, their failure in others is dramatic. This qualitatively incorrect behavior can in most cases be traced back to one common source, the self-interaction error (SIE) [21], which is a problem that was recognized already in Thomas-Fermi theory [27, 28], an ancestor of DFT. The SIE is trivial to define in an one-electron system with density n^1, in which there is no electron-electron interaction. Here, the exact xc energy (potential) and the Hartree energy

[1] And the local spin density approximation (LSDA) for spin-polarized systems.

[2] Although being far from chemical accuracy, which would require an error of less than 0.04336 eV per particle as compared to the experiment.

(potential) have to cancel each other

$$\begin{aligned} E_{\mathrm{H}}[n^1] + E_{\mathrm{xc}}[n^1] &= 0 \\ v_{\mathrm{H}}[n^1](\boldsymbol{r}) + v_{\mathrm{xc}}[n^1](\boldsymbol{r}) &= 0 \end{aligned} \tag{2.13}$$

by definition. An approximate functional must therefore satisfy Eq. (2.13) in order to be free of one-electron self-interaction. This notion can be extended to many-electron systems by identifying single electrons with KS orbital densities $n_{i\sigma} = f_{i\sigma}|\varphi_{i\sigma}|^2$. According to Perdew and Zunger [21, 29] one can then define the one-electron SIE in a many-electron system as

$$e_{i\sigma} = E_{\mathrm{H}}[n_{i\sigma}] + E_{\mathrm{xc}}[n_{i\sigma}, 0]. \tag{2.14}$$

If

$$\sum_{\sigma=\uparrow,\downarrow} \sum_{i=1}^{N_\sigma} e_{i\sigma} = 0 \tag{2.15}$$

the approximate functional is considered free of one-electron self-interaction. This definition suggests a straightforward way of correcting $E_{\mathrm{xc}}^{\mathrm{approx}}$ for self-interaction by simply subtracting the erroneous terms from the approximate xc functional

$$E_{\mathrm{xc}}^{\mathrm{SIC}}[n_\uparrow, n_\downarrow] = E_{\mathrm{xc}}^{\mathrm{approx}}[n_\uparrow, n_\downarrow] - \sum_{\sigma=\uparrow,\downarrow} \sum_{i=1}^{N_\sigma} (E_{\mathrm{H}}[n_{i\sigma}] + E_{\mathrm{xc}}^{\mathrm{approx}}[n_{i\sigma}, 0]). \tag{2.16}$$

This so-called self-interaction correction (SIC) an example for an orbital-dependent, implicit density functional. Two conceptual intricacies are associated with such functionals. First, the functional derivative $\delta E_{\mathrm{xc}}/\delta n_\sigma$ cannot be evaluated as straightforwardly as for explicit density functionals. One way to deal with this problem and at the same time to stay within the conceptual realm of KS DFT, is to use a functional derivative chain rule

$$v_{\mathrm{xc},\sigma}^{\mathrm{OEP}} = \frac{\delta E_{\mathrm{xc}}[\{\varphi_{j\tau}\}]}{\delta n_\sigma(\boldsymbol{r})} \tag{2.17}$$

$$= \sum_{\alpha=\uparrow,\downarrow} \sum_{i=1}^{N_\alpha} \int \frac{\delta E_{\mathrm{xc}}[\{\varphi_{j\tau}\}]}{\delta \varphi_{i\alpha}(\boldsymbol{r}')} \frac{\delta \varphi_{i\alpha}(\boldsymbol{r}')}{\delta n_\sigma(\boldsymbol{r})} d^3r' + \text{c.c.} \tag{2.18}$$

$$= \sum_{\alpha,\beta=\uparrow,\downarrow} \sum_{i=1}^{N_\alpha} \int\int \frac{\delta E_{\mathrm{xc}}[\{\varphi_{j\tau}\}]}{\delta \varphi_{i\alpha}(\boldsymbol{r}')} \frac{\delta \varphi_{i\alpha}(\boldsymbol{r}')}{\delta v_\beta^{\mathrm{KS}}(\boldsymbol{r}'')} \frac{\delta v_\beta^{\mathrm{KS}}(\boldsymbol{r}'')}{\delta n_\sigma(\boldsymbol{r})} d^3r' d^3r'' + \text{c.c.}, \tag{2.19}$$

where α, β, σ and τ denote the spin polarization and c.c. the complex conjugate. From this expression one obtains the *optimized effective potential* (OEP) equation

$$\sum_{i=1}^{N_\sigma} f_{i\sigma} \int \varphi_{i\sigma}^*(\boldsymbol{r}')[v_{\mathrm{xc},\sigma}^{\mathrm{OEP}}(\boldsymbol{r}') - u_{\mathrm{xc},i\sigma}(\boldsymbol{r}')] G_{i\sigma}^{\mathrm{KS}}(\boldsymbol{r}', \boldsymbol{r}) \varphi_{i\sigma}(\boldsymbol{r}) d^3r' + \text{c.c.} = 0 \tag{2.20}$$

in which $G_{i\sigma}^{\mathrm{KS}}(\boldsymbol{r}', \boldsymbol{r})$ is the KS Green's function

$$G_{i\sigma}^{\mathrm{KS}}(\boldsymbol{r}', \boldsymbol{r}) = \sum_{\substack{j=1 \\ j\neq i}}^{\infty} \frac{\varphi_{j\sigma}(\boldsymbol{r}')\varphi_{j\sigma}^*(\boldsymbol{r})}{\varepsilon_{i\sigma} - \varepsilon_{j\sigma}} \tag{2.21}$$

and $u_{\mathrm{xc},i\sigma}(\boldsymbol{r})$ an orbital specific potential

$$u_{\mathrm{xc},i\sigma}(\boldsymbol{r}) = \frac{1}{f_{i\sigma}\varphi^*_{i\sigma}(\boldsymbol{r})}\frac{\delta E_{\mathrm{xc}}[\{\varphi_{j\tau}\}]}{\delta\varphi_{i\sigma}(\boldsymbol{r})}. \tag{2.22}$$

The $v_{\mathrm{xc},\sigma}$ that solves Eq. (2.20) is called the optimized effective potential, as it yields the KS orbitals that minimize the total energy. For practical applications, a full OEP calculation is often computationally too demanding, as Eq. (2.20) is an integral equation and contains the complete set of occupied and unoccupied KS eigenvalues. The approximation of Krieger, Li and Iafrate (KLI) [30]

$$v^{\mathrm{KLI}}_{\mathrm{xc},\sigma}(\boldsymbol{r}) = \frac{1}{2n_\sigma(\boldsymbol{r})}\sum_{i=1}^{N_\sigma}|\varphi_{i\sigma}(\boldsymbol{r})|^2[u_{\mathrm{xc},i\sigma}(\boldsymbol{r}) + (\bar{v}^{\mathrm{KLI}}_{\mathrm{xc},i\sigma} - \bar{u}_{\mathrm{xc},i\sigma})] + \text{c.c.} \tag{2.23}$$

with

$$\bar{v}^{\mathrm{KLI}}_{\mathrm{xc},i\sigma} = \int \varphi^*_{i\sigma}(\boldsymbol{r}')v^{\mathrm{KLI}}_{\mathrm{xc},\sigma}(\boldsymbol{r}')\varphi_{i\sigma}(\boldsymbol{r}')d^3r' \tag{2.24}$$

$$\bar{u}_{\mathrm{xc},i\sigma} = \int \varphi^*_{i\sigma}(\boldsymbol{r}')u_{\mathrm{xc},i\sigma}(\boldsymbol{r}')\varphi_{i\sigma}(\boldsymbol{r}')d^3r' \tag{2.25}$$

provides an alternative that reduces the computational effort, but can in many cases yield results very close to those from a full OEP calculation [18].

The second intricacy of orbital-dependent functionals such as the SIC, is intimately related to the quantum mechanical nature (indistinguishability) of the interacting many-electron problem itself: One-electron orbitals are an artificial concept introduced through the KS ansatz and the KS orbitals are in no way unique among other orbital sets that also sum up to the correct ground state density. This *unitary invariance problem* means that different OEP can be constructed depending on the chosen orbital set. A generalization of the OEP method can be employed to deal with the unitary invariance problem via a density-conserving unitary transformation of the KS orbitals [31]. A detailed discussion of the OEP and approximations to it can be found in Ref. [17] and [18]. The ambiguity of the one-electron orbital sets also directly affects the definition of a SIE in many-electron systems. Attempts have been made to define a many-electron SIE. The issue will be discussed in Sec. 4.2. Eq. (2.14) is useful even without carrying out an actual SIC calculation. It provides a simple criterion for whether the KS eigenvalue spectrum resulting from a given approximate xc functional is physically reliable (see discussion in Sec. 2.3 and a practical example in Sec. 4.3) [32, 33].

A second class of orbital-dependent functionals are meta-GGAs. They contain the KS kinetic energy density

$$\tau_\sigma(\boldsymbol{r}) = \frac{\hbar^2}{2m}\sum_{i=1}^{N_\sigma} f_{i\sigma}|\nabla\varphi_{i\sigma}(\boldsymbol{r})|^2 \tag{2.26}$$

(and sometimes terms $\nabla^2 n_\sigma$) and improve in some respects upon semilocal functionals, e.g., they in principle can achieve absence of the self-correlation error. However, as complete self-interaction absence is not guaranteed by meta-GGAs, they share conceptual difficulties

with the LDA and GGA. An example for a meta-GGA relevant for the correct description of the 2d-3d transition in small Au-cluster anions [34] is the one by Tao, Perdew, Staroverov and Scuseria [35].

Hybrid functionals are among the most often used xc functional approximations and have become a favorite tool of quantum chemistry. Such functionals are constructed of a fixed fraction of exact exchange $E_{\mathrm{x}}^{\mathrm{ex}}$ as well as semilocal exchange $E_{\mathrm{x}}^{\mathrm{approx}}$ and correlation $E_{\mathrm{c}}^{\mathrm{approx}}$[3]. The approach was first introduced in 1993 by Becke [36], who proposed a functional form

$$E_{\mathrm{xc}}^{\mathrm{hyb}} = bE_{\mathrm{x}}^{\mathrm{ex}} + (1-b)E_{\mathrm{x}}^{\mathrm{approx}} + E_{\mathrm{c}}^{\mathrm{approx}}, \tag{2.27}$$

in which $E_{\mathrm{x}}^{\mathrm{ex}}$ denotes the Fock integral

$$E_{\mathrm{x}}^{\mathrm{ex}} = -\frac{e^2}{2}\sum_{\sigma=\uparrow,\downarrow}\sum_{i,j=1}^{N_\sigma} f_{i\sigma}f_{j\sigma}\int\int \frac{\varphi_{i\sigma}^*(\boldsymbol{r})\varphi_{j\sigma}^*(\boldsymbol{r}')\varphi_{j\sigma}(\boldsymbol{r})\varphi_{i\sigma}(\boldsymbol{r}')}{|\boldsymbol{r}-\boldsymbol{r}'|}d^3r d^3r'. \tag{2.28}$$

The parameter b is determined either by fitting to extensive test sets of molecules or rationalized by virtue of the adiabatic connection formalism [37, 38]. An example for the latter approach is the one-parameter hybrid PBE0, based on the PBE GGA [24] in which $b = 0.25$ [39]. However, most of today's hybrid functionals employ even more parameters, the most prominent example being the 3-parameter B3LYP functional [40, 41], that contains fractions of the semilocal Becke functional [25] as $E_{\mathrm{x}}^{\mathrm{approx}}$, the GGA by Lee, Yang and Parr [26] as $E_{\mathrm{c}}^{\mathrm{approx}}$ and the LDA parametrization by Vosko, Wilke and Nusair [20].

Finally, I want to mention the range-separated hybrids (RSHs). The underlying concept of these functionals is to separate the electron-electron interaction into a long-range and a short-range part via

$$\frac{1}{|\boldsymbol{r}-\boldsymbol{r}'|} = \underbrace{\frac{\mathrm{erf}(\omega|\boldsymbol{r}-\boldsymbol{r}'|)}{|\boldsymbol{r}-\boldsymbol{r}'|}}_{\text{long range}} + \underbrace{\frac{1-\mathrm{erf}(\omega|\boldsymbol{r}-\boldsymbol{r}'|)}{|\boldsymbol{r}-\boldsymbol{r}'|}}_{\text{short range}}. \tag{2.29}$$

The screening function is for numerical reasons often chosen as the error function and ω is an adjustable parameter that determines at which length scale the short-range part of Eq. (2.29) decays to zero and the long-range part becomes dominant. The long-range part is given by the screened Fock integral, so that one preserves the advantages of employing semilocal exchange at short range, while incorporating 100% of the non-local exact exchange at long range and thus obtains the correct asymptotic behavior of the xc potential. Hence, RSHs are particularly useful for the description of charge transfer excitations, but they can also improve on ground state properties [42].

An example for such a functional is ωPBE, which is a RSH that models the exchange hole of the PBE GGA at short range [43]. The range-separation parameter can be obtained in different ways: One can empirically determine the value of ω that describes thermochemistry or charge transfer excitations best. However, evidence suggests that in fact considerably

[3] Prior to their formal justification via the generalized KS framework, these functionals had been seen as "hybrids" between DFT and Hartree-Fock.

different range-separation parameters might be necessary depending on the particular system and properties of interest. Another approach is therefore to tune ω for each system in such a way that certain properties of the exact functional (such as Eq. (2.33) in Sec. 2.3) are fulfilled [44].

Orbital-dependent functionals can be used in conjunction with the OEP method as explained above. The widely used hybrids (and RSHs) are practically always implemented in a way which leaves the grounds of the KS framework. This second approach is justified by the observation that it is possible to formulate a so-called *generalized* KS approach in which the interacting N-electron system is mapped onto another interacting auxiliary system, which can, however, still be represented by a single Slater-determinant [45].

2.3 Interpretation of (generalized) Kohn-Sham eigenvalues

Given their status as merely auxiliary quantities within the KS framework, it might be surprising that the KS eigenvalues should carry any physical meaning at all. However, the success of DFT partly relies on the fact that in an overwhelmingly large number of systems the eigenvalue spectra agree, apart from a shift of the complete spectrum, remarkably well with experimentally obtained quasiparticle energies. In the early days of DFT this agreement was regarded accidental. Later, Görling could show that KS eigenvalue differences have in fact a well-defined physical meaning as excitation energies of zeroth order in the electron-electron interaction [46]. The derivation is based on linking the interacting full Hamiltonian to the KS Hamiltonian through

$$[\hat{T} + \alpha\hat{W} + \hat{V}^{\alpha}]|\psi_n^{\alpha}\rangle = E_n^{\alpha}|\psi_n^{\alpha}\rangle. \tag{2.30}$$

The coupling constant α creates a continuous (adiabatic) connection between the fully interacting N-electron system with $\alpha = 1$ and $\hat{V}^{\alpha=1} = \hat{V}_{\text{ext}}$ and the non-interacting KS system with $\alpha = 0$ and $\hat{V}^{\alpha=0} = v^{\text{KS}}$ [37, 38]. Using Görling-Levy perturbation theory [47] one can then expand E_n^{α} in a Taylor series in α and show that excitation energies can rigorously be gained from ground state DFT. In particular, the zeroth order term connects the quasiparticle excitation energies to KS eigenvalue differences.

The practical usefulness of Görling's finding of course depends on the quality of this zeroth order approximation. Chong et al. could show that the energetically highest lying occupied KS levels can be interpreted as approximate, but rather accurate, relaxed vertical ionization potentials, provided that they are computed using a high-quality xc potential [48]. Already earlier it was observed by Janak [49] that

$$\frac{\partial E}{\partial f_{i\sigma}} = \varepsilon_{i\sigma}, \tag{2.31}$$

where $f_{i\sigma}$ is the (fractional) occupation of the i-th KS orbital. A rigorous physical meaning, however, can only be assigned to the highest occupied KS eigenvalue $\varepsilon_{\text{HOMO}}$, which is

identical to minus the ionization potential $I(N)$ of the fully interacting physical system. This was proved by Almbladh and von Barth [50] by deriving differential equations for the quasiparticle amplitudes

$$F_{n,\sigma}(\boldsymbol{r}) := \langle \psi_n^{N-1} | \hat{\Psi}_\sigma(\boldsymbol{r}) | \psi_0^N \rangle, \tag{2.32}$$

where $\hat{\Psi}_\sigma(\boldsymbol{r})$ is the electron-field operator which annihilates an electron of spin σ at $\boldsymbol{r}$ and ψ_n^N are the N-electron eigenstates of the full many-body Hamiltonian. A closer look at the asymptotic decay of this quasiparticle amplitude shows that the asymptotically leading amplitude is obtained for $n = 0$ and that the density itself is dominated by $F_{0,\sigma}(\boldsymbol{r})$ for $|\boldsymbol{r}| \to \infty$. By comparing this result to the asymptotic form of the KS density, which is dominated by the most weakly decaying KS orbital, one arrives at the identity

$$\varepsilon_{\mathrm{HOMO}}(N) = -I(N) = E(N) - E(N-1). \tag{2.33}$$

Similarly, one can show for the electron affinity $A(N)$, i.e., the energy gained by bringing in a particle from infinity that

$$\varepsilon_{\mathrm{HOMO}}(N+1) = -A(N) = E(N+1) - E(N). \tag{2.34}$$

$E(N-1), E(N)$ and $E(N+1)$ are the energies of the $N-1$, N and $N+1$ electron system, respectively.

In practical calculations one often faces the problem of not knowing whether the used xc functional describes the system of interest accurately or not. As a rule of thumb may count, that in systems in which the upper occupied KS orbitals are localized on a similar length scale, standard xc functionals result in eigenvalue spectra that are physically reliable [21]. The SIE in such systems, that can be evaluated using Eq. (2.14), affects all relevant orbitals in the same way and therefore only amounts to a common shift of the eigenvalue spectrum [32]. In systems in which the upper orbitals differ in their degree of localization, the spectrum will be distorted as a result of the SIE affecting the orbitals differently. In this sense, evaluation of Eq. (2.14) can serve as a warning for systems that are strongly affected by the SIE. Note, however, that the relation between orbital localization and the SIE is not trivial [51].

The close connection between the SIE and the reliability of an eigenvalue spectrum suggests that self-interaction free approaches (in the sense of Eq. (2.15)) should yield good agreement with experiment in cases in which semilocal functionals fail and indeed this has been shown for a number of systems (see e.g. Ref. [32]). However, these approaches are numerically expensive, especially in cases in which finding the energetically most favorable position of the nuclei poses additional problems (see Sec. 2.5). The commonly used hybrid functionals can at least partly cancel the SIE by employing a fraction of exact exchange.

As mentioned earlier, hybrid functionals are typically implemented in a GKS framework. The GKS equations

$$\begin{aligned} \Big(&-\frac{\hbar^2}{2m}\nabla^2 + v_{\mathrm{ext}}(\boldsymbol{r}) + v_{\mathrm{H}}([n],\boldsymbol{r}) + v_{\mathrm{c},\sigma}([n],b,\boldsymbol{r}) \\ &+ b\hat{v}_{x,\sigma}^{\mathrm{ex}}[n] + (1-b)v_{x,\sigma}([n],\boldsymbol{r})\Big)\varphi_{i\sigma}(\boldsymbol{r}) = \varepsilon_{i\sigma}^{\mathrm{GKS}}\varphi_{i\sigma}(\boldsymbol{r}), \end{aligned} \tag{2.35}$$

in which

$$\hat{v}^{\mathrm{ex}}_{x,\sigma}[n]\varphi_{i\sigma}(\boldsymbol{r}) = -e^2 \sum_{\sigma=\uparrow,\downarrow} \sum_{j=1}^{N_\sigma} \int \frac{\varphi_{j\sigma}(\boldsymbol{r})\varphi^*_{j\sigma}(\boldsymbol{r}')}{|\boldsymbol{r}-\boldsymbol{r}'|}\varphi_{i\sigma}(\boldsymbol{r}')d^3r' \tag{2.36}$$

denotes the non-local Fock operator, are by construction exact, just as the KS equations. The resulting eigenvalues $\varepsilon^{\mathrm{GKS}}_{i\sigma}$ differ from the exact KS eigenvalues by

$$b\Delta v_{x,\sigma,i} = b\langle\varphi_{i\sigma}(\boldsymbol{r})|\hat{v}^{\mathrm{ex}}_{x,\sigma}[n] - v_{x,\sigma}([n],\boldsymbol{r})|\varphi_{i\sigma}(\boldsymbol{r})\rangle, \tag{2.37}$$

if one neglects differences in the KS and GKS orbitals and the correlation potential [45]. As $\Delta v_{x,N} = 0$ for the highest occupied GKS eigenvalue, the relation $\varepsilon^{\mathrm{GKS}}_{\mathrm{HOMO}} = -I(N)$ holds also for the GKS case. There is again no such equality for all the other GKS eigenvalues. However, one can show that including a fraction of the non-local exchange mimics a partial self-interaction correction [52]. Consequently, GKS eigenvalues agree well with experimental results for many cases in which semilocal functionals fail.

2.4 Pseudopotentials

The basic idea of replacing the strong Coulomb potential of the nucleus and the screening effect of the tightly bound core electrons by an effective core potential (commonly refered to as pseudopotential), has its roots in the simple notion that only the valence electrons of an atom determine its chemical properties.

The approach was originally introduced by Fermi when he studied low energy electron scattering from atoms [53]. In fact, the aim of the pseudopotential construction is to find an effective potential that mimics the scattering properties of nucleus and core electrons reliably over a certain energy range. The degrees of freedom of pseudopotential generation then allow to devise them in such a way as to minimize the computational effort. Firstly, by reducing the number of electrons that have to be considered explicitly in the DFT calculation. Secondly, because pseudopotentials allow the numerical description of potentials and orbitals on much coarser grids or with fewer plane wave components than would be necessary if the highly oscillatory structure of the orbitals in the core-region had to be represented completely. In the present thesis pseudopotentials enter the stage at yet another point. When one deals with heavy-element transition metal compounds such as Au and Pt, relativistic effects such as spin-orbit coupling and the relativistic mass increase of electrons in the core region are crucial for the accurate description of the electronic, and thus also the geometric structure of the compounds [54]. Pseudopotentials offer ways in which these effects can be accounted for implicitly.

An important concept underlying most pseudopotential generation schemes is the *frozen-core approximation*: The core states, evaluated in an all-electron atomic reference calculation, are assumed not to change if in a different environment, i.e., in a molecule or solid. For this reason the radius of the core region r_c is a crucial parameter determining transferability and accuracy of the pseudopotential.

2.4.1 Norm-conserving pseudopotentials

The spirit of *norm-conservation* is to start the construction of the pseudopotential from the all-electron orbitals that stem from a self-consistent solution of the radial KS equation[4] (for a spin-unpolarized case)

$$\left(-\frac{\hbar^2}{2m}\frac{d^2}{dr^2}+\frac{\hbar^2 l(l+1)}{2mr^2}+v^{\mathrm{KS}}([n],r)\right) rR_{il}(r)=\varepsilon_{il} rR_{il}(r), \tag{2.38}$$

in which $rR_{il}=\varphi_{il}$ and l denotes the angular momentum quantum number. The pseudopotential has to fulfill four properties to be considered norm-conserving: First, all-electron (AE) and pseudo (PP) valence eigenvalues must agree for a chosen atomic reference configuration. Second, all-electron and pseudo orbitals agree beyond a chosen core radius r_c. Third, the integrated charge inside r_c of the all-electron and the pseudo charge densities agree for each valence state

$$\int_0^{r_c}|R_{il}^{\mathrm{PP}}(r)|^2 r^2 dr=\int_0^{r_c}|R_{il}^{\mathrm{AE}}|^2 r^2 dr, \tag{2.39}$$

as this ensures that the total charge in the core region is conserved. And last, the logarithmic derivatives of the all-electron and the pseudo orbitals and their first energy derivatives agree for $r>r_c$ [56]. The freedom that is left in constructing the pseudopotential can then be used to make it as smooth as possible at the same time ensuring transferability to as many different chemical environments as possible. Different schemes for pseudopotential generation were proposed, e.g., by Bachelet, Hamann and Schlüter [57] and by Troullier and Martins [58].

By inverting the radial KS equations one then obtains the screened pseudopotential from the pseudo wavefunction

$$v_{\mathrm{screened},l}^{\mathrm{PP}}=\varepsilon_l-\frac{\hbar^2}{2m}\left(\frac{l(l+1)}{r^2}-\frac{1}{rR_l^{\mathrm{PP}}(r)}\frac{d^2}{dr^2}[rR_l^{\mathrm{PP}}(r)]\right). \tag{2.40}$$

In the last step the screening of the valence electrons has to be removed to obtain an unscreened ("bare") ionic pseudopotential

$$v_{\mathrm{ionic},l}^{\mathrm{PP}}(\boldsymbol{r})=v_{\mathrm{screened},l}^{\mathrm{PP}}(\boldsymbol{r})-v_{\mathrm{H}}^{\mathrm{PP}}[n^{\mathrm{val}}](\boldsymbol{r})-v_{\mathrm{xc}}^{\mathrm{PP}}[n^{\mathrm{val}}(\boldsymbol{r})] \tag{2.41}$$

The resulting pseudopotential differs for every angular momentum component l, i.e., the effective external potential in the KS equations is not local anymore. A further transformation suggested by Kleinman and Bylander brings Eq. (2.41) in a separable non-local form that reduces computation time and storage space. Troullier-Martins pseudopotentials in Kleinman-Bylander form are used throughout this work for calculations on real-space grids using a local version of the PARSEC program package [59], e.g., for the calculation of the SIE of Mn-doped Si clusters in Sec. 4.3.

[4] If relativistic effects are to be included one has to use Dirac's formulation of the kinetic energy. The Schrödinger-like Eq. (2.38) is then replaced by a pair of coupled equations for minor and major orbital components, which outside the core radius reduce approximately to a Schrödinger-type equation for the major orbital component [55].

A final remark on norm-conserving pseudopotentials concerns their applicability to spin-polarized systems. In Eq. (2.41), it is implicitly assumed that core and valence charge density do not significantly overlap and that the xc potential can thus be written as

$$v_{\mathrm{xc},\sigma}[n^{\mathrm{val}} + n^{\mathrm{core}}, \xi] = (v_{\mathrm{xc},\sigma}[n^{\mathrm{val}} + n^{\mathrm{core}}, \xi] - v_{\mathrm{xc},\sigma}[n^{\mathrm{val}}, \xi^{\mathrm{val}}]) + v_{\mathrm{xc},\sigma}[n^{\mathrm{val}}, \xi^{\mathrm{val}}], \tag{2.42}$$

where

$$\xi(\boldsymbol{r}) = \frac{n_{\uparrow}^{\mathrm{val}}(\boldsymbol{r}) - n_{\downarrow}^{\mathrm{val}}(\boldsymbol{r})}{n^{\mathrm{val}}(\boldsymbol{r}) + n^{\mathrm{core}}(\boldsymbol{r})} \tag{2.43}$$

and

$$\xi^{\mathrm{val}}(\boldsymbol{r}) = \frac{n_{\uparrow}^{\mathrm{val}}(\boldsymbol{r}) - n_{\downarrow}^{\mathrm{val}}(\boldsymbol{r})}{n_{\uparrow}^{\mathrm{val}}(\boldsymbol{r}) + n_{\downarrow}^{\mathrm{val}}(\boldsymbol{r})}. \tag{2.44}$$

Since $v_{\mathrm{xc},\sigma}$ is a non-linear function of the charge density the ionic pseudopotential will depend on the valence configuration. This feature is particularly worrisome for magnetic elements, whose spin density distribution is highly sensitive to their environment. An ionic pseudopotential depending on the valence charge density would thus be not transferable from the atomic to a condensed matter case. A straightforward solution to this problem was suggested by Louie, Froyen and Cohen by introducing a so-called non-linear core correction

$$v_{\mathrm{ionic},l,\sigma}^{\mathrm{PP}}(\boldsymbol{r}) = v_{\mathrm{screened},l,\sigma}^{\mathrm{PP}}(\boldsymbol{r}) - v_{\mathrm{H}}^{\mathrm{PP}}[n^{\mathrm{val}}](\boldsymbol{r}) - v_{\mathrm{xc},\sigma}^{\mathrm{PP}}[n^{\mathrm{val}} + n^{\mathrm{core}}, \xi(\boldsymbol{r})](\boldsymbol{r}) \tag{2.45}$$

The resulting pseudopotential is essentially independent of spin polarization and reference atomic configuration and thus highly transferable [60].

The remaining drawback is connected to the construction of norm-conserving pseudopotentials for xc functionals containing exact exchange. In these cases the density in the core region affects the exchange potential in the valence region via the non-local xc potential. A spurious long-range tail in the ionic pseudopotential is the consequence which can cause erroneous bond lengths and binding energies. The issue is discussed in detail in Ref. [61] as well as in Ref. [18] and references therein.

2.4.2 Energy-adjusted pseudopotentials

Energy-adjusted pseudopotentials were used to treat Au and Pt (Pd) in all calculations using the TURBOMOLE program suite [62] (see Sec. 3.2 – 3.4.1). Here, an atomic model potential of the form

$$\begin{aligned} v^{\mathrm{PP}}(r_i) &= -\frac{Q}{r_i} + \sum_l \sum_k A_{lk} \exp(-\alpha_{lk} r_i^2) P_l \\ P_l &= \sum_m |lm\rangle\langle lm|, \end{aligned} \tag{2.46}$$

where Q is the charge of the nucleus, r_i the radial distance of the electrons from the nucleus and lm are the angular momentum quantum numbers, is used [63]. The pseudopotential parameters A_{lk} and α_{lk} are adjusted to total valence energies from numerical all-electron calculations. Relativistic effects are implicitly accounted for by fitting the pseudopotential parameters to the results of relativistic all-electron calculations. For optimal accuracy 18 (19) valence electrons have to be considered explicitly for Pt and Pd (Au).

2.4.3 Projector augmented waves

A natural choice of basis function for calculations of periodic solids are plane waves. These are often combined with the so-called *projector augmented wave* (PAW) formalism [64–66]. This method allows to remove the highly oscillatory core states from the calculation of energies, densities, etc. and at the same time keeping information about the full Bloch wavefunction in the core and valence region.

The Bloch functions $\Psi_{n\mathbf{k}}(\boldsymbol{r})$ are converted into smooth functions $\tilde{\Psi}_{n\mathbf{k}}(\boldsymbol{r})$ by virtue of a linear transformation $\mathcal{T} = \mathbb{1} + \mathcal{T}_0$, that is unity everywhere except in spherical regions with radius r_c^a around each nucleus denoted by a. Here $\mathbf{k}$ and n are the wave vector and the band index, respectively.

The transformation operator $\mathcal{T}_0$ can be represented by three sets of basis functions: the all-electron orbitals φ_i^a, which are obtained by solving the radial Schrödinger equation, smooth pseudo orbitals $\tilde{\varphi}_i^a$ that have to equal the all-electron orbitals outside the core region and so called projector functions $\tilde{p}_i^a$:

$$\mathcal{T}_0 = \sum_{i,a} \left[\varphi_i^a(\boldsymbol{r} - \boldsymbol{R}^a) - \tilde{\varphi}_i^a(\boldsymbol{r} - \boldsymbol{R}^a)\right] \langle \tilde{p}_i^a|. \tag{2.47}$$

Here $\boldsymbol{R}^a$ denotes the position of the nuclei. The projector functions have to vanish outside the core region and fulfill $\langle \tilde{p}_i^a | \tilde{\varphi}_j^a \rangle = \delta_{ij}$ [64]. The transformation between all-electron and pseudo Bloch functions $\tilde{\Psi}_{n\mathbf{k}}(\boldsymbol{r})$ can be expressed as

$$\Psi_{n\mathbf{k}} = \tilde{\Psi}_{n\mathbf{k}} + \sum_{i,a} c_i^a \left[\varphi_i^a(\boldsymbol{r} - \boldsymbol{R}^a) - \tilde{\varphi}_i^a(\boldsymbol{r} - \boldsymbol{R}^a)\right], \tag{2.48}$$

where

$$\tilde{\Psi}_{n\mathbf{k}} = \sum_{i,a} c_i^a \tilde{\varphi}_i^a \tag{2.49}$$

and the expansion coefficients fulfill

$$c_i^a = \langle \tilde{p}_i^a | \tilde{\Psi}_{n\mathbf{k}} \rangle. \tag{2.50}$$

With these definitions all operators can now be expressed as sums of three contributions. The electron density, e.g., is $n(\boldsymbol{r}) = \tilde{n}(\boldsymbol{r}) + n^1(\boldsymbol{r}) - \tilde{n}^1(\boldsymbol{r})$. Here $\tilde{n}(\boldsymbol{r})$ is the pseudo density, which can be expressed as a plane wave expansion throughout the unit cell

$$\tilde{n}(\boldsymbol{r}) = \sum_{n\mathbf{k}} f_{n\mathbf{k}} |\tilde{\Psi}_{n\mathbf{k}}(\boldsymbol{r})|^2, \tag{2.51}$$

where $f_{n\mathbf{k}}$ are the respective occupation numbers. $n^1(\boldsymbol{r})$ and $\tilde{n}^1(\boldsymbol{r})$ cancel each other for $r > r_c^a$ and are localized around each nucleus: $n^1(\boldsymbol{r}) = \sum_a n^a(\boldsymbol{r} - \boldsymbol{R}^a)$ and $\tilde{n}^1(\boldsymbol{r}) = \sum_a \tilde{n}^a(\boldsymbol{r} - \boldsymbol{R}^a)$, where

$$n^a(\boldsymbol{r}) = \sum_{n\mathbf{k},i,j} f_{n\mathbf{k}} \langle \tilde{\Psi}_{n\mathbf{k}} | \tilde{p}_i^a \rangle \langle \tilde{p}_j^a | \tilde{\Psi}_{n\mathbf{k}} \rangle (\varphi_i^a(\boldsymbol{r}))^* \varphi_j^a(\boldsymbol{r}) \tag{2.52}$$

and

$$\tilde{n}^a(\boldsymbol{r}) = \sum_{n\mathbf{k},i,j} f_{n\mathbf{k}} \langle \tilde{\Psi}_{n\mathbf{k}} | \tilde{p}_i^a \rangle \langle \tilde{p}_j^a | \tilde{\Psi}_{n\mathbf{k}} \rangle (\tilde{\varphi}_i^a(\boldsymbol{r}))^* \tilde{\varphi}_j^a(\boldsymbol{r}). \tag{2.53}$$

Similar expressions can be derived for other quantities. See, e.g., Ref. [65], for a detailed derivation of the KS Hamiltonian within the PAW formalism and methods for constructing the basis and projector functions.

Plane waves in conjunction with PAW were used to compute activation barriers for adatom diffusion on Au- and Pt-surfaces in Sec. 3.4.3 with the Vienna-Ab-inito-Simulation-Package (VASP) [67].

2.5 Methods of geometry optimization

Probably the most infamous characteristic of atomic clusters is that the search for their ground state geometric structure somewhat resembles searching a needle in a haystack. The potential energy surface even of comparably small clusters can exhibit hundreds of local minima, a situation additionally complicated for alloy clusters, in which for every possible geometric arrangement of the M cluster atoms of type A and B there are

$$P_{\mathrm{A,B}} = \frac{M!}{M_{\mathrm{A}}! M_{\mathrm{B}}!} \tag{2.54}$$

possible arrangements of the M_{A} A- and the $M_{\mathrm{B}} = M - M_{\mathrm{A}}$ B-type atoms. Clusters with the same geometry but different arrangements of atom types A and B are called *homotops*. Local geometry optimizations starting from structures either randomly generated or stemming from "educated guesses"[5] can yield the desired ground state. Most often, however, one needs to scan a much larger part of the cluster potential energy surface in an unbiased as possible way.

Optimization techniques accomplishing this task are called *global optimization* algorithms. Note however, that although a global optimization may in principle yield the correct ground state, in practice there is no way to ensure its success, but comparison with experimental data. Mn-doped Si-clusters, a system discussed in Chap. 4, are an example.

In the following, two methods of geometry optimization, namely simulated annealing and the "big bang" method, are presented. Additionally, an algorithm for searching transition states, the Nudged Elastic Band (NEB) method, is discussed.

2.5.1 Simulated annealing

The simulated annealing technique has a very descriptive equivalent in real-world physics. Consider, e.g., the growth of a single crystal from a melt, which is achieved by careful

[5] This could be highly symmetric geometries, such as icosahedra, tetrahedra, octahedra, etc. Such polyhedra indeed turn out to be the ground state structure of many transition metal clusters, e.g., Au_{20} which has tetrahedral geometry [68].

annealing. The material is melted and subsequently the temperature is decreased very slowly, especially near the freezing point of the material. This procedure prevents the substance from being trapped in metastable states, i.e., forming a glass or a crystal with a large number of defects.

A global optimization scheme inspired by this process was proposed in 1983 by Kirkpatrick, Gelatt and Vecchi [69] and two years later by Černý [70]. It can be applied to a variety of optimization problems, even if the concept of temperature is not immediately applicable.

For the optimization of cluster structures, temperature is defined via the equipartition theorem

$$T = \frac{2E_{\mathrm{kin}}}{k_{\mathrm{B}} N_{\mathrm{f}}}, \tag{2.55}$$

in which k_{B} is the Boltzmann constant, N_{f} is the number of degrees of freedom of the system and E_{kin} is the average kinetic energy of the atoms. In this work (using the TURBOMOLE program package), the energy of the electronic system as well as its gradients were calculated in a DFT framework. A Leapfrog Verlet algorithm [71] was used to compute the dynamical evolution of the atomic nuclei $\boldsymbol{R}^a$ according to Newton's equations

$$m^a \frac{d^2}{dt^2} \boldsymbol{R}^a = -\nabla_a \left[E^{\mathrm{KS}} \left(\{ \boldsymbol{R}^a \} \right) \right], \tag{2.56}$$

with E^{KS} being the energy resulting from a self-consistent solution of the KS equations for a set of fixed atomic positions $\boldsymbol{R}^a$. Starting with randomly generated velocities that are equivalent to some initial temperature which lies well beyond the system's melting point, the temperature is then reduced slowly, e.g., every 100 time steps by a factor of 0.95, until convergence of the geometry is reached. Although simulated annealing in principle allows to find the global minimum structure in the limit of infinitely slow cooling, in practice many different starting geometries and temperatures have to be tested to avoid trapping in local energy minima.

2.5.2 The "Big Bang" search

The optimization algorithm with the eccentric name "big bang" search represents a simple and unbiased method to scan the phase space of a cluster for its global minimum [72]. A large number of random configurations of the M cluster atoms is created in a volume highly compressed compared to the usual molar volume of the system. These geometries are then relaxed using a standard local gradient-based optimization procedure. If the volume of the initial configuration is chosen appropriately, the clusters will explode upon relaxation, but subsequently relax into a minimum of the potential energy surface. This method was e.g. used to determine the ground state structures of small neutral and cationic silicon [72] and copper clusters [73]. In this work a modification of the "big bang" search was used for searching the ground state structures presented in Sec. 4.3, in which instead of hundreds, only a few configurations were created randomly in a compressed volume. These were then used as the starting point for a molecular dynamics (MD) simulation at a moderate temperature of 300 K. The lowest energy geometries from these simulations were subsequently locally relaxed using a standard gradient-based optimization algorithm.

2.5.3 The Nudged Elastic Band method

A different optimization technique has to be applied if one is not interested in finding the global minimum of a system, but rather the minimum energy path (MEP) between two local minima. Examples are chemical reactions or diffusion events, e.g., on surfaces.

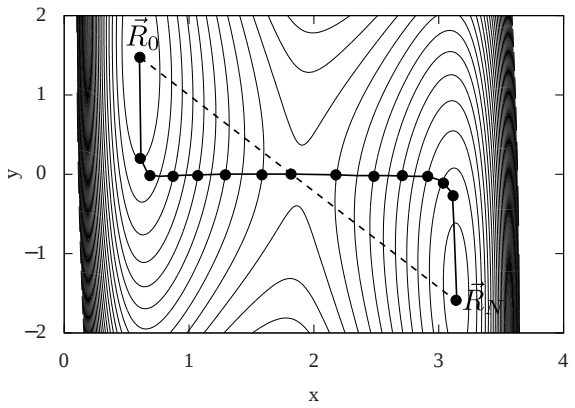

Figure 2.1: Contour plot of the potential energy surface of a simple model adapted from Ref. [74]. The dashed line is a linear interpolation between initial and final state of the system. The solid line represents the elastic band that is close to convergence to the MEP.

The height of the saddle point between these local minima can then be used to determine reaction rates using transition state theory [75]. For the so-called Elastic Band methods [74, 76], inital and final state of the reaction of interest have to be known. Fig. 2.1 shows an illustrative example.

Plotted are the contours of the potential energy surface of a simple model potential, that can, e.g., be used to describe an activated process (a chemical reaction) coupled to a medium (a solvent in which the reaction takes place). For details of this model that are of no interest here, I refer the reader to Ref. [74, 77]. The model illustrates a potential energy surface exhibiting two local minima and one saddle point between them. A string of images (black spheres), i.e., geometrical configurations, denoted by $\{\boldsymbol{R}_i\}$ with $i = 0...N$, connected by springs with spring constant k_i is used to describe the path. Typically a linear interpolation between inital and final state is sufficient as a first guess of the MEP.

The force acting on image i is

$$\boldsymbol{F}_i = -\nabla E(\boldsymbol{R}_i) + \boldsymbol{F}_i^{\mathrm{s}}, \tag{2.57}$$

with the spring force

$$\boldsymbol{F}_i^{\mathrm{s}} = k_{i+1}(\boldsymbol{R}_{i+1} - \boldsymbol{R}_i) - k_i(\boldsymbol{R}_i - \boldsymbol{R}_{i-1}). \tag{2.58}$$

This ”plain” elastic band method leads to some problems. If the spring constant is too high, i.e., the elastic band to stiff, it might cut a corner and thus might not be able to converge to the true MEP. For smaller spring constants the elastic band can approach the MEP, but in the crucial region around the saddle point the resolution of the elastic band can be too low, because images in this region tend to slide away from the saddle point due to the component of $\nabla E(\boldsymbol{R}_i)$ in the direction of the path.

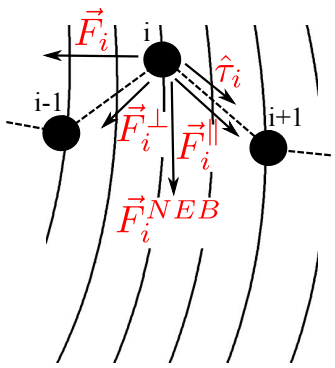

Figure 2.2: Forces acting on an image along the NEB. The resulting force F_i^{NEB} pulls the image in the direction of the MEP.

A simple force projection scheme, which is dubbed "nudging" the path, solves these problems. In this scheme, forces due to the potential only act perpendicular to the band, while spring forces act parallel to the band. This means that the total energy acting on image i in the NEB is

$$\boldsymbol{F}_i^{\mathrm{NEB}} = \boldsymbol{F}_i^{\perp} + \boldsymbol{F}_i^{\parallel} \tag{2.59}$$

$$\boldsymbol{F}_i^{\perp} = -\nabla E(\boldsymbol{R}_i) - (-\nabla E(\boldsymbol{R}_i) \cdot \hat{\boldsymbol{\tau}}_i \hat{\boldsymbol{\tau}}_i) \tag{2.60}$$

$$\boldsymbol{F}_i^{\parallel} = k(|\boldsymbol{R}_{i+1} - \boldsymbol{R}_i|) - |\boldsymbol{R}_i - \boldsymbol{R}_{i-1}|)\hat{\boldsymbol{\tau}}_i, \tag{2.61}$$

where k is the spring constant and $\hat{\boldsymbol{\tau}}_i$ the tangent along the path.

Fig. 2.2 illustrates the forces acting on each image along the NEB. $\boldsymbol{F}_i$ denotes the force due to the potential. The component $\boldsymbol{F}_i^{\perp}$ is obtained by subtracting out the component parallel to the tangent $\hat{\boldsymbol{\tau}}_i$. Nudging ensures that the resolution of the elastic band in the vicinity of a saddle point is better than for plain elastic band methods as described above. However, if the number of images is small, the NEB method can fail to locate the saddle point.

In cases where one needs to find the highest saddle point between $\boldsymbol{R}_0$ and $\boldsymbol{R}_N$, e.g., to determine activation barriers, the NEB method can be modified in such a way that the image l highest in energy does not feel any spring forces and climbs to the saddle point via a reflection in the force along the tangent

$$\boldsymbol{F}_l^{\mathrm{CI}} = \boldsymbol{F}_l - 2\boldsymbol{F}_l \cdot \hat{\boldsymbol{\tau}}_l \hat{\boldsymbol{\tau}}_l. \tag{2.62}$$

Next to this so-called climbing-image NEB (CI-NEB) other variations of the method exist. For a detailed comparison of these methods as well as a range of optimization algorithms for updating the forces in NEB and CI-NEB the reader is referred to Ref. [74].

3

The bimetallic effect in Au-Pt and Au-Pd nanoalloys

3.1 Au-Pt and Au-Pd nanoalloys in catalysis

Alloying of two (or more) elements is a promising route to enhance the catalytic activity of transition metal NP and improve their element-specific selectivity [78]. Loosely based on Aristotle's *bon mot* that "the whole is greater than the sum of its parts", these effects are frequently dubbed synergistic. Au-Pt nanoalloys are a prominent example of a system which exhibits increased turnover rates in a variety of oxidation reactions [79–81] as well as enticing properties in electrocatalytic applications [82–90] compared to their pure counterparts. Au-Pt nanoalloys are beneficial because they reduce the well-known problem of "poisoning" of Pt catalyst anodes used in direct methanol fuel cells with strongly adsorbed intermediate CO-species. Furthermore, increased turnover rates allow to carry out reactions at room temperature and without possibly toxic solvents, thus causing less impact on the environment. Finally, by changing the Au-Pt composition one can tune their catalytic properties which makes Au-Pt nanoalloys potentially useful for many different catalytic reactions. When looking deeper into these problems, several puzzles appear.

The first puzzle is the miscibility of Au and Pt on the nanoscale. It is well known that the bulk phase diagram of Au-Pt alloys exhibits a large miscibility gap for a wide range of Au-Pt compositions. In going to the nanoscale it has been reported that Au-Pt NP can form true solid solutions. Such Au-Pt nanoalloys have, e.g., been synthesized in thermally evaporated fatty amine films, where they were alloyed at low temperature [91], in spherical polyelectrolyte brushes (SPBs) [80] and in ionic liquids by a sputter deposition technique

[92]. Other groups have obtained stable Au-Pt nanoalloys by capping them with thiolates [82, 93] or by supporting them on silica [79].

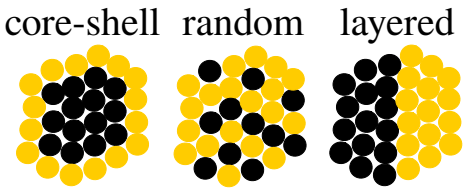

Figure 3.1: Three possible miscibility patterns in bimetallic NP. From left to right: core-shell, randomly mixed and layered. Other patterns such as several layers/shells or an ordered solid solution are possible.

Theory, in contrast, consistently predicts a Au_{shell}-Pt_{core} mixing pattern as energetically most favorable [94–97]. An illustration of different mixing patterns in NP is given in Fig. 3.1.

Theoretical studies of clusters in the experimentally relevant size range of several hundred up to thousands of atoms have been based on semiempirical MD simulations and were mostly concerned with the melting behaviour of the Au-Pt NP [98–101]. A global geometry optimization using a genetic algorithm with a semiempirical Gupta-many-body potential of Au-Pt clusters with 2–100 atoms has been performed by Logsdail et al. [102]. First-principles DFT studies existed, up to the beginning of this work, only for very small clusters with 2–13 atoms [103, 104]. However, more recent studies on larger clusters (including one that will briefly be presented in Sec. 3.2), have confirmed that Au-Pt NP prefer a core-shell mixing pattern [94–97]. This seeming discrepancy of theory and experiment is subject of Sec. 3.3.

The second Au-Pt nanoalloy puzzle is their enhanced catalytic activity as compared to their pure counterparts. Considering the known bulk electronic properties of Pt and Au[1] it is not *per se* clear, why a combination of Pt and Au should lead to enhanced catalytic activity at all (see also Sec. 3.4.1). Additionally, while it is known how the electronic structure of Au changes upon going from the bulk to small NP [2], similar insights into the electronic structure of Au-Pt nanoalloys are rare. Explanations for the special properties of Au-Pt nanoalloys have been attempted in several studies, mainly concentrating on the local electronic structure of Pt [85, 95, 104, 106]. A detailed understanding of the concurrence of Au and Pt leading to favorable catalytic properties in a variety of different reactions, i.e., independent of the type of support or matrix the NP are immobilized in, possible solvents and different reaction temperatures, is lacking. Puzzle number two will be subject of Sec. 3.4.

Although elements from the Pt-group are chemically similar, the above matters are slightly different for Au-Pd nanoalloys. The structural characterization of Au-Pd NP is much easier as compared to Au-Pt NP, as Au and Pd's atomic numbers are sufficiently different to allow for the use of high-resolution techniques, e.g., high-angle-annular-dark-field transmission electron microscopy [107]. Synergistic effects have been observed for Au-Pd NP catalysts in a variety of reactions. Two recent examples are Au-Pd nanoalloys used for electrocatalytic H_2O_2 production [108] and for solvent-free oxidation of primary carbon-hydrogen bonds [107]. As the following sections will focus primarily on Au-Pt nanoalloys, I refer the reader to Ref. [78] and references therein, for a summary of studies in which a synergistic effect of Au-Pd catalysts was observed. Insights into the electronic structure of Au-Pd nanoalloys and their impact on Au-Pd catalysis are discussed in Sec. 3.4.1.

[1] Presented in a nutshell in "Why gold is the noblest of all metals" by Hammer et al. in Ref. [105].

3.2 Geometric structure and mixing patterns of Au-Pt nanoalloys

This section gives a short summary of results that are discussed in detail in Ref. [109]. Most of the nanoalloy properties that will be identified in the following sections as being favorable for catalytic activity are to a large extend independent of the exact geometric structure of the clusters. Still, energetically low-lying Au-Pt isomers are a well-chosen starting point for the study of these properties. In combined efforts of theory and experiment, the ground state structure of many pure neutral and charged Au clusters has been determined. A prominent example are Au_{20} and Au_{20}^-, whose ground state structure is a regular tetrahedron as revealed by gas phase infrared spectroscopy [110] and photoelectron spectroscopy [68]. Au_{20} is an excellent toy model for the present study as it represents a cutout of the fcc lattice in which both bulk Au and Pt crystallize. Furthermore, many of the experimentally observed Au-Pt nanoalloys have been shown to be largely faceted and bulk-like (e.g. [80]).

By systematically replacing Au by Pt atoms in Au_{20} one finds that the energetically lowest lying homotop is always that in which Pt is as highly coordinated as possible. In going from Au_{20} to $Au_{19}Pt_1$, as illustrated in Fig. 3.2, the energetically lowest lying homotop is the one in which Pt occupies a position in the middle of one of the four facets. As a result of this growth pattern a $Au_{shell}Pt_{core}$ structure emerges naturally. That the core-shell mixing pattern is not a mere artifact was tested by comparing homotops and isomers with fixed Au-Pt composition especially for structural motifs other than the rather special tetrahedral structure as well as for larger clusters. The stability of a variety of structures was tested using simulated annealing (see Sec. 2.5). In these simulations the clusters were heated to a temperature of 600 K and subsequently slowly annealed. Importantly, the core-shell mixing pattern remains stable throughout the entire simulation and can therefore be regarded as being stable even at elevated temperatures.

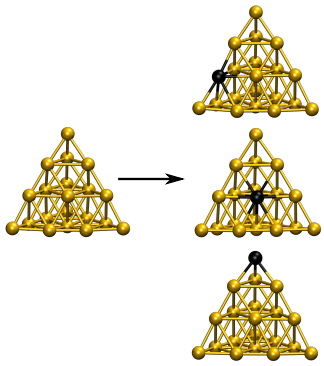

Figure 3.2: There are three symmetry-inequivalent ways how to replace one Au atom in the Au_{20} tetrahedron by a Pt atom.

Fig. 3.3 shows, as an example, different $Au_{20}Pt_{20}$ isomers from A to F with increasing total energy. Note that even a complete segregation of the Au and the Pt component (C and D) is energetically more favorable than the random mixing pattern (E and F). Computational details on the geometry optimization and the accuracy of the used xc functional and basis sets as well as structures of tetrahedral and amorphous Au_nPt_{20-n} clusters can be found in Ref. [109] and [94]. In this work, Au-Pt NP with ≈ 1000 valence electrons, i.e., 60-atom clusters, were the largest systems for which full local geometry optimizations were performed. The Gupta potential based $Au_{30}Pt_{30}$ structure [102] was used as a starting point for these calculations.

However, considering that experimentally relevant nanocatalysts range between sizes of

1 and 4 nm, we need even larger systems to exclude that the observed effects are only due to the comparably small size of the clusters.

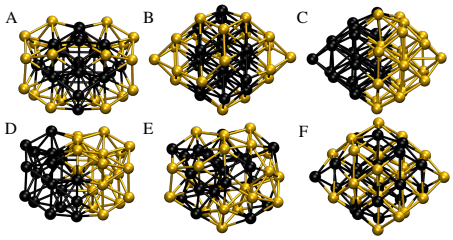

Figure 3.3: Structures are named after the geometry that served as a starting point of the geomtry optimization either "Gupta" [102] or "Sutton Chen" [111]. A: Gupta core-shell, B: Sutton-Chen core-shell, C: Sutton-Chen layered, D: Gupta layered, E: Gupta random, F: Sutton-Chen random.

Two strategies were used to overcome the computational limitations that first principles DFT calculations face for systems with significantly more than 1000 valence electrons. Firstly, we constructed truncated octahedral clusters with closed atomic shells, i.e., with 38, 201, 586 and 1289 atoms as illustrated in Fig. 3.4 and optimized them in empirical MD simulations. These clusters are, analogously to Au_{20}, cutouts of the fcc lattice and are used in the studies discussed in Sec. 3.3 and 3.4. Clusters with regular polyhedral structures and closed atomic shells are sometimes called "magic", in analogy to the magic electron numbers that were discovered by Knight et al. in 1984 in sodium clusters [112]. This seminal discovery triggered the development of cluster physics much beyond the realm of the simple spherical jellium model which was used to explain the abundance of sodium clusters containing 2, 8, 20, 40,... atoms. Electronic shell closure effects within the jellium model are responsible for the stability of these cluster sizes in the simple alkali metals and even in Au clusters, as their $6s$ states form a good free electron gas [2].

For larger clusters the electronic shell closure effect is superimposed by the closure of atomic shells, a prominent example again being sodium clusters that exhibit icosahedral shell closures [113]. In sodium clusters with a few tens of atoms, electronic and ionic shell closure effects work together in determining the structure of the clusters, while for larger clusters, starting with Na_{55}, ionic shell closure effects win over electronic ones resulting in near-ly spherical clusters [114]. However, I want to stress that truncated octahedral structures might not be a structural motif found in smaller Au clusters. The important point is that they are faceted and fcc-bulk-like, which makes them a valuable model for the catalysts observed experimentally.

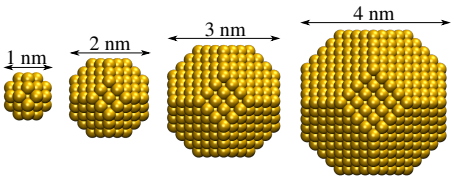

Figure 3.4: Truncated octahedra with (from left to right) 38, 201, 586 and 1289 atoms. These atomic numbers are called magic, because they correspond to clusters having only closed shells of atoms. The approximate diameters of these clusters are 1, 2, 3 and 4 nm.

A second approach to catalysis on Au-Pt NP is to model them as periodic surface slabs. The motivation for this is twofold: Firstly, much of the catalytic activity of NP can be attributed to their high surface to volume ratio. Secondly, a synergistic effect of Au and Pt has also been observed for bimetallic surfaces [115]. Au-Pt surfaces are studied in Sec. 3.4.

In summary, the following Au-Pt structures are used in the present thesis to determine structural and electronic properties of Au-Pt systems: 20-atom tetrahedral and amorphous low-energy isomers, 40-atom and 60-atom structures based on empirical potentials and fully

optimized using DFT, truncated octahedral model structures with 38, 201, 586 and 1289 atoms for which different arrangements of Au and Pt, e.g., in core-shell and random mixing patterns can be constructed, and finally bimetallic surface slabs.

3.3 Au-Pt alloys and Vegard's law on the nanoscale

All results of this section are published in Ref. [116]. In the previous two sections I discussed that first-principles DFT calculations confirm that low-energy structures of free Au-Pt clusters indeed exhibit an $Au_{shell}Pt_{core}$ mixing pattern and thus confirm the results of semi-empirical MD simulations mentioned in Sec. 3.1. The seeming discrepancy between theory (core-shell) and experiment (solid solution) must thus be searched for elsewhere.

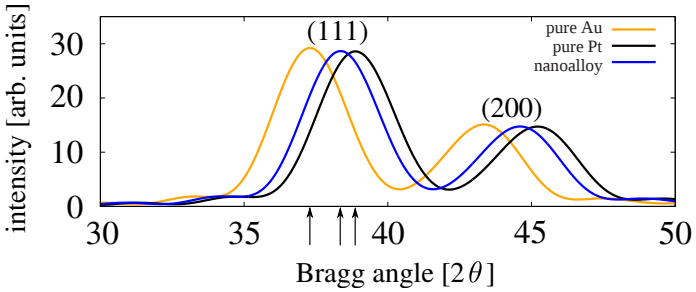

Figure 3.5: A sketch of the first two Bragg peaks as typically observed in XRD measurements on Au-Pt NP. From these diffraction patterns it can presumably be inferred that the system under study (blue line) is a true solid solution. The arrows indicate the position of the first Bragg peak.

The next step is to understand the assumptions that underlie the experimental characterization of Au-Pt NP. A prominent characterization method is the use of x-ray diffraction (XRD) techniques. The resulting diffraction patterns are typically analyzed as sketched in Fig. 3.5. The orange and black lines indicate the first two Bragg peaks of pure Au and pure Pt NP as observed in small angle x-ray scattering experiments. These peaks can be indexed into an fcc-type lattice. For each set of Miller indices (hkl) one can then use Bragg's equation $a = \frac{\lambda\sqrt{h^2+k^2+l^2}}{2\sin\theta}$ to determine a lattice parameter a from the scattering angle θ. Here, λ is the wave length of the incoming x-rays.

The same can be done for the diffraction pattern of the bimetallic NP. Additionally, depending on the experimental resolution, one can use the peak shape to determine, whether the system of interest shows any sign of demixing of Au and Pt (in which case one would expect distinct peaks for the Au- and the Pt-phase) or whether it forms a real alloy (only one clear peak). The blue line in Fig. 3.5 would, following this reasoning, belong to a randomly mixed Au-Pt NP.

Bulk alloys often obey Vegard's law [117], which states that the lattice parameter of a two-component alloy can be determined by linearly interpolating between the lattice parameters of the two components that form the alloy. Hence in an alloy that consists of 50% of both elements, the average lattice parameter would be just the average of the lattice parameters of both pure crystals. XRD characterization now reveals that the lattice

parameter of Au-Pt NP goes linearly with the Au-Pt ratio as well. This finding is taken as evidence that Au-Pt NP form true alloys (see, e.g., Ref. [80, 93]).

The "Vegard-analysis" thus assumes firstly that a phase separation must be visible in the diffraction pattern, secondly that Vegard's law is valid and can be used to determine the composition of the alloy and thirdly that Vegard's law is only valid for randomly mixed alloys. By simulating the XRD patterns of pure Au and Pt, as well as of randomly mixed and core-shell NP one can thus test the validity of these assumptions.

The scattering intensity I of an ensemble of atoms is given by Debye's equation

$$I = \sum_m \sum_n f_m f_n \frac{\sin kR_{mn}}{kR_{mn}}, \tag{3.1}$$

where f_n and f_m are the form factors of atoms n and m, $R_{mn} = |\boldsymbol{R}_m - \boldsymbol{R}_n|$ is the distance of two atoms at positions $\boldsymbol{R}_m$ and $\boldsymbol{R}_n$ and $k = 4\pi \sin\theta/\lambda$ is the wave number.

The general scattering equation (3.1) for atoms which are randomly oriented in space is easily derived by considering that one obtains the scattered x-ray intensity by summing over the scattering amplitudes of x-rays scattered by different atoms

$$\begin{aligned} I &= \sum_m f_m e^{(2\pi i/\lambda)(\boldsymbol{s}-\boldsymbol{s}_0)\boldsymbol{R}_m} \sum_n f_n e^{(-2\pi i/\lambda)(\boldsymbol{s}-\boldsymbol{s}_0)\boldsymbol{R}_n} \\ &= \sum_m \sum_n f_m f_n e^{(2\pi i/\lambda)(\boldsymbol{s}-\boldsymbol{s}_0)\boldsymbol{R}_{mn}}, \end{aligned} \tag{3.2}$$

where $\boldsymbol{s}$ and $\boldsymbol{s}_0$ are the directions of incoming and outgoing x-rays, as sketched in Fig. 3.6.

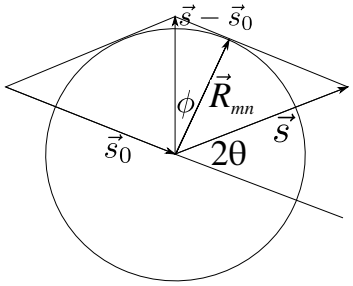

Figure 3.6: A sketch of the scattering of light at an ensemble of randomly oriented atoms, where the difference vector $\boldsymbol{R}_{mn} = \boldsymbol{R}_m - \boldsymbol{R}_n$ is allowed to take all orientations in space, i.e., all positions on the black circle with equal probability (adapted from [118]).

Eq. (3.2) is of course valid for scattering on any ensemble of atoms. We now assume that this ensemble takes all orientations in space with equal probability, i.e., that $\boldsymbol{R}_{mn}$ ends at all points of the sphere sketched in Fig. 3.6 (in 2d) with equal probability. The spatial average of the exponential term $\langle e^{2\pi i/\lambda(\boldsymbol{s}-\boldsymbol{s}_0)\boldsymbol{R}_{mn}}\rangle$ can with $k = 4\pi \sin\theta/\lambda$ and $(\boldsymbol{s} - \boldsymbol{s}_0)\boldsymbol{R}_{mn} = 2\sin\theta R_{mn}\cos\phi$ be written as

$$\begin{aligned} \langle e^{ikR_{mn}\cos\phi}\rangle &= \frac{1}{4\pi R_{mn}^2} \int dA e^{ikR_{mn}\cos\phi} \\ &= \frac{1}{4\pi R_{mn}^2} \int_0^{2\pi} d\varphi \int_0^{\pi} d\phi R_{mn}^2 \sin\phi e^{ikR_{mn}\cos\phi} \\ &= \frac{\sin kR_{mn}}{kR_{mn}}, \end{aligned}$$

and leads to Debye's scattering equation 3.1.

Additionally, temperature effects that cause atomic vibrations independent from each other could be taken into account by including a Debye-Waller factor [119, 120] in the Debye

Table 3.1: Average bond lengths and their standard deviations for core-shell and random $Au_{22}Pt_{38}$ (37% Au) as obtained from DFT and MD optimization.

DFT	Au-Au [Å]	Au-Pt [Å]	Pt-Pt [Å]
core-shell	2.88 ± 0.03	2.85 ± 0.03	2.76 ± 0.05
random	2.90 ± 0.05	2.82 ± 0.06	2.72 ± 0.06
MD	Au-Au [Å]	Au-Pt [Å]	Pt-Pt [Å]
core-shell	2.74 ± 0.03	2.70 ± 0.04	2.69± 0.04
random	2.73 ± 0.04	2.70 ± 0.04	2.67 ± 0.04

equation (3.1). We do not include this factor here, as we will explicitly take temperature into account by performing MD simulations at elevated temperatures.

A reasonable simulation of XRD patterns requires two important conditions to be met. Firstly, the size of the NP needs to be between 3 and 4 nm to conform with the experimental size range. Secondly, the interatomic bond lengths need to be realistic, as they are the decisive input to Eq. (3.1). As already mentioned, these requirements pose severe difficulties to DFT, as computational effort forbids to treat NP of such size, i.e., with more than 1000 Au and Pt atoms. On the other hand, the reliability of bond length estimates is best if a first-principles method is used for geometry optimization. We assess this problem in the following way. The 1289-atom truncated octahedron as shown on the right hand side of Fig. 3.4 is used as a starting point for geometry optimization. A pure Au and Pt, a $Au_{shell}Pt_{core}$ with one and two Au-shells (corresponding to the NP $Au_{484}Pt_{805}$ and $Au_{830}Pt_{459}$ respectively) and finally a randomly mixed NP with exactly the same Au-Pt ratio as the core-shell particle $Au_{484}Pt_{805}$ were constructed based on the truncated octahedral geometry. The geometry optimization of these systems was carried out using MD simulations, in which the potential energy was modelled by the many-body Sutton-Chen potential [121], that has been employed successfully in simulations of a variety of nanoalloys [100, 122–124]. The Sutton-Chen parameters for the Au-Pt interaction were obtained from the parameters for the Au-Au and Pt-Pt interaction using a combination rule [100]. Each system was first relaxed at 1 K and subsequently propagated for 500 ps at a temperature of 300 K in a canonical ensemble using Evans' thermostat [125] and vacuum boundary conditions. Every 20 ps a structure "snapshot", yielding a set of atomic positions $\{\boldsymbol{R}_m\}$, was taken. These structures were then optimized with a conjugate gradient procedure. For each system the optimized geometry with the lowest energy was taken as the final structure for further analysis. All MD simulations in this and Sec. 3.4.3 were carried out by Rodrigo Q. Albuquerque using the DL-POLY program package [126].

The second part of our strategy consists of determining the Au-Au, Pt-Pt and Au-Pt bond lengths of DFT-optimized core-shell and random geometries. We do not expect the bond lengths resuling from MD simulations to equal the DFT bond length, because the Sutton-Chen parameters are fitted to bulk properties and bulk bond lengths are typically slightly different from NP bond lengths. However, what is decisive here is, that the relative differences between the Au-Au, Pt-Pt and Au-Pt bond lengths resulting from MD and DFT optimization, respectively, are similar.

As one of the larger systems where structure optimization with DFT is still possible we chose the 60-atom cluster $Au_{22}Pt_{38}$. Its Au content of about 37% is similar to that of the 4 nm cluster $Au_{459}Pt_{830}$ that is the main focus of our study. We generated starting

Au content	method	Au-Au [Å]	Au-Pt [Å]	Pt-Pt [Å]
87 %	DFT	2.87 ± 0.02	2.83 ± 0.03	2.72 ± 0.02
	MD	2.75 ± 0.01	2.71 ± 0.02	2.73 ± 0.06
50 %	DFT	2.87 ± 0.08	2.83 ± 0.05	2.65 ± 0.05
	MD	2.73 ± 0.06	2.68 ± 0.05	2.65 ± 0.03
13 %	DFT	none	2.84 ± 0.04	2.72 ± 0.04
	MD	none	2.68 ± 0.04	2.65 ± 0.02

Table 3.2: Average bond lengths and standard deviations obtained from DFT and MD optimization of randomly mixed 38-atomic clusters with different Au-Pt mixing ratios.

structures by taking the coordinates from the 60-atomic cluster in Ref. [102] and distributed Au and Pt atoms once randomly and once in a Pt-core Au-shell fashion to these positions. The structures were then relaxed with DFT and MD separately. In the DFT calculations the relaxation was carried out without any symmetry constraints using a split valence basis set augmented by one polarization function (SVP). The use of larger basis sets changes the bond length by less than 2% [94] and does not affect the relative distribution of the lengths of Au-Au, Au-Pt and Pt-Pt bonds.

For the optimized structures we calculated the distance of every atom to its five nearest neighbors, at the same time determining whether these bonds were Au-Au, Au-Pt or Pt-Pt bonds. The average Au-Au bond length was then defined by the arithmetic mean of all resulting Au-Au distances. In the same way, Au-Pt and Pt-Pt bond lengths were calculated. The results stay qualitatively the same if one somewhat changes the averaging procedure, e.g., using four instead of five nearest neighbors.

Tab. 3.1 shows the average bond lengths thus obtained from DFT and MD for core-shell and for randomly mixed variants of $Au_{22}Pt_{38}$. The MD bond lengths are found to be consistently smaller than the DFT bond lengths. However, the trends with respect to bond length differences are similar. For both DFT and MD calculations the differences between the average length of Au-Au bonds, Au-Pt bonds and Pt-Pt bonds that one finds in randomly mixed and core-shell particles are small. In all cases Au-Au bonds are longest and Pt-Pt bonds are shortest, with Au-Pt falling in between.

In order to also test the MD bond length distribution for a faceted particle we chose the smallest truncated octahedron built from 38 atoms. Alloy particles with Au contents of 87 % ($Au_{33}Pt_5$), 50 % ($Au_{19}Pt_{19}$) and 13 % (Au_5Pt_{33}) were generated by distributing Au and Pt atoms randomly over the cluster. The structures were energetically optimized as described previously. Tab. 3.2 shows the resulting average bond lengths. We observe again that the MD and DFT average bond lengths are not identical, with the MD bonds generally being shorter than the DFT ones. Yet, again the trends are the same in both DFT and MD: Au-Au bonds are the longest and Pt-Pt bonds are the shortest, with Au-Pt bonds falling in between. The one exception that we found is shown in Tab. 3.2 for 87 % Au, where Au-Pt and Pt-Pt bonds in the MD are quite similar. We attribute this to the low Pt concentration and small particle size. We also performed the same type of analysis for the 20-atom tetrahedral and amorphous structures that are described in Ref. [94]. The results are in line with the conclusions drawn for the 38-atom and 60-atom structures shown above and are therefore not reported in detail here.

We can now analyze the average bond lengths of the $Au_{459}Pt_{830}$ core-shell and randomly

mixed truncated octahedron. In the core-shell cluster the large Pt core dominates the bond length distribution, with an average Pt-Pt distance of 2.77 Å. The mean Au-Au distance in the single Au shell is the same as the mean Pt-Pt bond length. This finding is reminiscent of the lattice deformation and matching that one encounters when growing single layers of one material on a substrate with a different lattice parameter. The Au-Pt distance of 2.78 Å is slightly larger, allowing the shell to wrap around the core. The bond length most often encountered in the randomly mixed NP is one that falls in between the Au-Au and the Pt-Pt bond length, with Au-Pt bonds on average being 2.76 Å, Au-Au bonds 2.79 Å, and Pt-Pt bonds 2.74 Å.

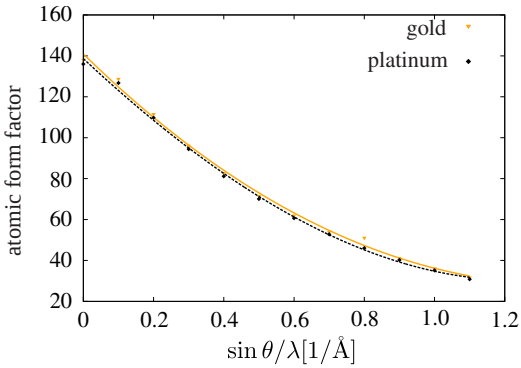

Figure 3.7: Atomic form factors for Au and Pt taken from Ref. [127] and polynomial least square fits to the data.

After these preliminary considerations we turn to simulating the XRD patterns of the NP using Eq. (3.1) with the incoming x-rays having a wave length of λ=1.5 Å. The form factors of Au and Pt are tabulated in Ref. [127] and fitted using a polynomial least squares fit to allow continuous representation of the data (see Fig. 3.7).

The top left panel in Fig. 3.8 shows the pattern that one obtains from pure Au or Pt NP with 1289 atoms in orange and black, respectively. The red line shows the x-ray pattern for the core-shell NP. As laid out above the expectation so far has been to find separate peaks for this type of structure, as the Au and Pt component are separated. Yet, no double-peak structure is observed at all; the peak shapes for the different NP are nearly identical. Our first important conclusion therefore is that a core-shell structure in NP does not necessarily lead to separate x-ray peaks for the different components. The lower left panel shows the second important result: The x-ray pattern for the core-shell NP (as above) and the one for the randomly mixed NP are very similar. Core-shell structures may thus be hard to identify via x-ray scattering.

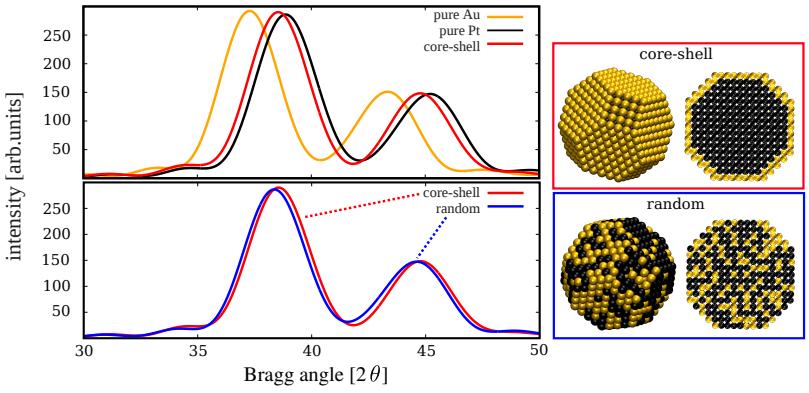

Figure 3.8: Left: Calculated XRD pattern of pure Au, Pt, and core-shell NP (top) and core-shell and randomly mixed NP (bottom). Right: View of the core-shell (top) and randomly mixed (bottom) NP (outside and cross section).

However, we now take the analysis one step further and go through the Vegard's-law-based analysis of the x-ray data as explained above. For pure NP the x-ray analysis leads

to a lattice parameter of 4.06 Å for Au and 3.90 Å for pure Pt. These are very close to the respective bulk values, i.e., the Vegard's-law-based analysis correctly identifies the NP as pure ones. This result also confirms the validity of our procedure for building the particles and calculating the x-ray patterns. The decisive question now is how well the procedure works when we translate the x-ray pattern obtained for the bimetallic NP into lattice parameters and the relative Au and Pt content using Vegard's law as explained above and in Fig. 3.5. If this interpretation is valid, then it should yield exactly 38% of Au and 62% of Pt, corresponding to the $Au_{484}Pt_{805}$ particles that we constructed. Yet, for the core-shell particle the value of a deduced from the x-ray pattern is 3.94 Å, and the Vegard's-law-based analysis translates this into an Au content of ca. 19%. Thus, it underestimates the Au content by a factor of 2. This is a serious misprediction. For the randomly mixed particle the situation is better, yet not perfect, with an a of 3.95 Å being translated into an Au content of 31%.

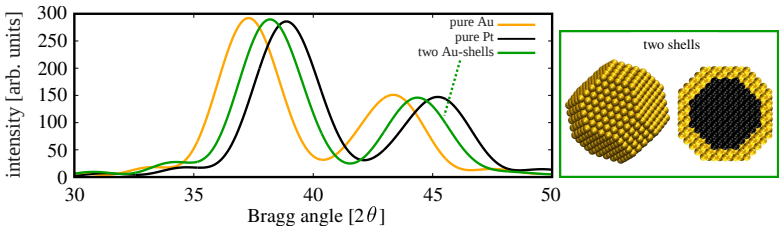

Figure 3.9: Calculated x-ray scattering patterns (left) and visualization (right) of a core-shell NP with two shells of Au.

In order to further elucidate the situation we also calculated the diffraction pattern of the core-shell NP with two layers of Au (see Fig. 3.9). This particle, $Au_{830}Pt_{459}$, has an Au content of 64%. A Vegard's-law-based analysis of the x-ray pattern is again far off the mark. It predicts a3.97 Å, corresponding to 44% of Au. Thus, instead of showing that the particle contains more Au than Pt, the x-ray analysis leads one to believe that the NP contains more Pt than Au.

In judging the significance of these results one should recall that our analysis so far has been conducted under ideal conditions, as our calculated x-ray patterns stem from monodisperse, zero-temperature particles. In actual experiments the uncertainties in determining the NP' Au and Pt content from Vegard's law can be larger than the discrepancies that we find here. One can thus imagine that an Au-Pt core-shell particle with roughly one shell of Au might be classified as almost-pure Pt. It may thus appear less puzzling that $Au_{shell}Pt_{core}$ NP have rarely been found in experimental x-ray analysis despite theoretical prediction of their existence.

In order to estimate the effects that temperature may have and to explicitly check what influence the presence of different structures has on the x-ray pattern, we performed constant temperature MD simulations as described above, in each case starting from the lowest energy configuration and thermalizing the particle for 1 ns at 1, 50, 100, 200, 250, 300, 600, and 1400 K, respectively. From the last 400 000 steps of each simulation we took 10 structures, each one being 40 000 time steps 1 fs distant from the previous one. For each of the structures we calculated the x-ray pattern and then averaged the patterns of a given temperature.

Fig. 3.10 shows these finite temperature diffraction patterns. A first, expected obser-

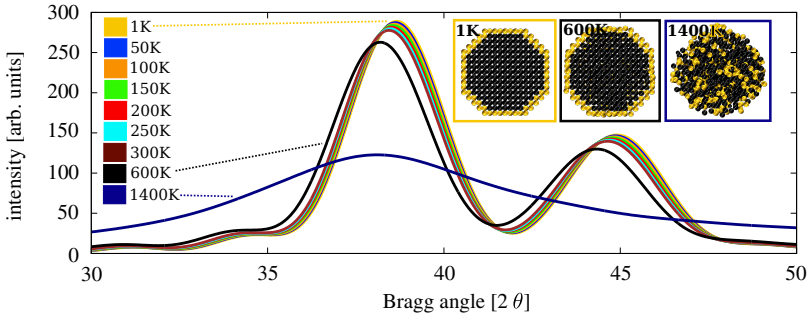

Figure 3.10: Average NP x-ray scattering patterns at temperatures of 1, 50, 100, 150, 200, 250, 300, 600, and 1400 K. Inset: NP cross sections at 1, 600, and 1400 K.

vation is that the peak heights are reduced. At 1400 K the pattern is also considerably broadened, corresponding to a much wider bond length distribution compared to that at lower temperatures. As the melting point of the core-shell particle lies at ca. 1200 K, we observe randomly mixed structures at 1400 K, whereas for the lower temperatures the core-shell mixing pattern is retained, though with an increasingly softening surface. A further observation to be made in Fig. 3.10 is that the peaks for elevated temperatures are shifted, and while some shift is expected due to thermal expansion, the magnitude of the shift is much larger than one would expect based on the bulk expansion coefficient. It has been noted that thermal expansion in small metal clusters is considerably larger than in the bulk [128]. Therefore, we calculated the linear thermal expansion coefficient

$$\beta = \frac{1}{L}\frac{\partial L}{\partial T} \tag{3.3}$$

by evaluating the temperature dependence of the mean interatomic distance

$$L = \frac{1}{M(M-1)} \sum_{i,j=1}^{M} |\boldsymbol{R}_i - \boldsymbol{R}_j|, \tag{3.4}$$

where $\boldsymbol{R}_i$ denotes the position of atom i. The average thermal expansion coefficient that we obtain in this way up to 600 K is about $19 \cdot 10^{-6} K^{-1}$, i.e., considerably larger than that of bulk Au (ca. $14 \cdot 10^{-6} K^{-1}$) and bulk Pt (ca. $9 \cdot 10^{-6} K^{-1}$). We also see that the surface atoms contribute the most strongly to the expansion. Thus, NP at finite temperatures are likely to have a "diffuse" surface, and this may contribute to their special catalytic properties.

Finally, having demonstrated the limits of traditional x-ray analysis for Au-Pt NP, we exploit the strength of theoretical simulations to offer direct access to bond length distributions. Thus, we can take a yet closer look at Vegard's law. Fig. 3.11 shows the average bond length as obtained from DFT-based geometry optimizations for 20-atom, 38-atom and 60-atom particles as a function of the Au content. The striking observation in Fig. 3.11 is that for all particles, independent of the size and of whether the atoms are core-shell or randomly distributed, the average bond length increases linearly with increasing Au content. Thus, one might say that for small particles Vegard's law is valid not only for randomly distributed alloys, but also for other types of bimetallic Au-Pt particles, independently of the specific way in which the atoms are arranged.

In summary, we have shown that Vegard's law is ambiguous on the nanoscale, as it may hold not only for random alloys. However, more importantly, we have shown that Vegard's law does not translate into x-ray peaks in the way that has so far been assumed. Even under the ideal conditions that can theoretically be realized an Au-shell in core-shell NP is poorly visible in x-ray scattering. The Au content of core-shell particles is greatly underestimated when analyzing XRD patterns based on Vegard's law. Finite-temperature simulations showed that thermal expansion in 3.5 nm Au-Pt NP is much greater than in the bulk and affects surface atoms most strongly.

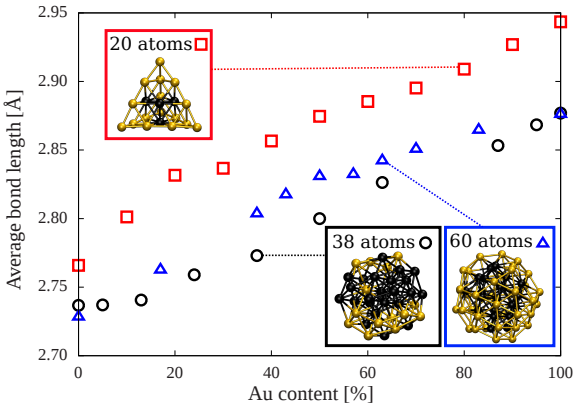

Figure 3.11: Average nearest-neighbor bond length of 20-, 38-, and 60-atom core-shell-like clusters with varying Au contents.

The fact that the low energy structures theoretically predicted for free Au-Pt NP undoubtedly are core-shell structures still does not exclude the possibility that true Au-Pt nanoalloys form in experiments. True Au-Pt nanoalloys have, e.g., recently been observed using element-specific XRD in conjunction with theoretical modeling [129]. However, the theoretical findings suggest that the existence of Au-Pt nanoalloys may be linked to effects beyond the ones present in free particles. These may be external influences such as solvents, supports, and special preparation procedures, possibly in combination with entropical contributions which, at finite temperatures, can limit the probability of observing the lowest energy configuration. First results on the effect of a support interacting with the NP are presented in Appendix A.

3.4 The interplay between fluxionality and electronic structure

Finding an answer to the question why Au-Pt and Au-Pd nanoalloys show synergistic behavior first requires another question to be asked: Which properties does a "good" catalyst have to have? On the one hand, catalysis requires the breaking and the formation of bonds, i.e., interaction between the catalyst and an adsorbate should have an adequate strength. On the other hand, the catalyst should not be consumed during the reaction, i.e., it should have the ability to regenerate itself after the reaction. A property of this type could also be beneficial for the formation of active and element-specific binding sites, e.g., via thermal expansion or surface corrugation. This optimal combination of properties has been recognized as early as 1911 by Sabatier [130], who proposed that the interaction strength between a catalyst and the reactants had to be "just right", i.e., neither too strong nor too weak. *Sabatier's principle* is often reflected in so called *volcano plots* in which

the turnover rate of a reaction is plotted as a function of some catalytic "descriptor" for different catalysts called el1, el2, etc. in Fig. 3.12.

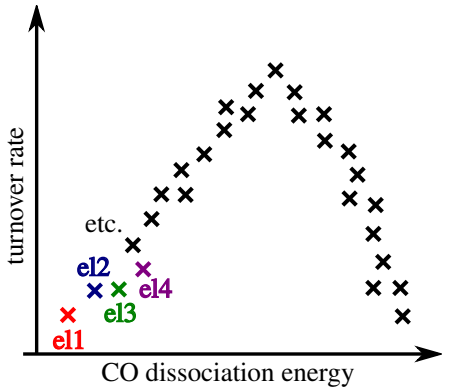

Figure 3.12: Schematic of volcano plot. The "optimal" catalyst corresponds to an optimal dissociation energy and high turnover rates as explained in the text.

Take, e.g., the methanation reaction CO + $3H_2$ → CH_4 + H_2O. Here, the CO activation barrier and the stability of C and O on the catalyst's surface are closely related. The more strongly C and O are bound to the surface, the lower is the barrier for CO dissociation. At the same time this results in a higher barrier for CH_4 and H_2O formation [131]. An optimal catalyst is thus one for which the CO dissociation energy, the catalytic descriptor in this example, is neither too high nor too low, i.e., it sits at the top of the volcano in Fig. 3.12. In our case, the situation is more complex. The NP not only interacts with possible reactands, but also with support molecules and the solvent. Furthermore, typical reactions are carried out at room or even higher temperature. A meaningful simulation of one specific reaction would have to take these effects into account, an at present nearly impossible task for non-empirical DFT. Yet, the volcano picture can elucidate the bimetallic effect seen in Au-Pt (and Au-Pd nanoalloys). By assuming that the Au-Pt ratio can be seen as the catalytic descriptor here, a possible explanation for the finding that Au-Pt nanoalloys show high catalytic activity under many different conditions and for many different reactions could be that there are rather fundamental, basic properties that are not specific to certain reactions and which quite generally can optimize the catalytic behavior of Au-Pt nanoalloys. I will show in Sec. 3.4.4 that the density of states (DOS) at the Fermi level, contributed by Pt, and the atomic mobility or structural flexibility, contributed by Au, are such properties. The Au-Pt ratio then determines how much DOS at the Fermi level and structural flexibility are, in terms of Sabatier's principle, "optimal" for a specific reaction. The results of Sec. 3.4.1 and 3.4.2 are published in Ref. [94] and [132]. Parts of Sec. 3.4.1 already appear in Ref. [109] and will therefore only briefly be treated here.

3.4.1 Electronic structure of Au-Pt nanoalloys

The first electronic property that springs to mind when one deals with metal clusters, is the static electric dipole polarizability α, defined as one third of the trace of the polarizability tensor $\underline{\underline{\boldsymbol{\alpha}}}$. This quantity measures the linear response of the electric dipole moment of a system to an applied electric field $\boldsymbol{p} = \underline{\underline{\boldsymbol{\alpha}}}\boldsymbol{E}$. The static electric dipole polarizability of sodium clusters has been studied intensively both experimentally, e.g., in Ref. [133] and [134], and theoretically, e.g., in Ref. [128] and [135], because of sodium's prototypical metallic properties. The electronic shell closure effects that lead to particularly stable cluster sizes in small sodium clusters (as already mentioned in Sec. 3.2), coincide with "dips" of the static electric dipole polarizability. It is therefore a close-lying assumption that

"special" electronic properties of Au-Pt NP, i.e., properties that could be connected to high catalytic activities at a certain ratio of Au and Pt, could also show up in this quantity.

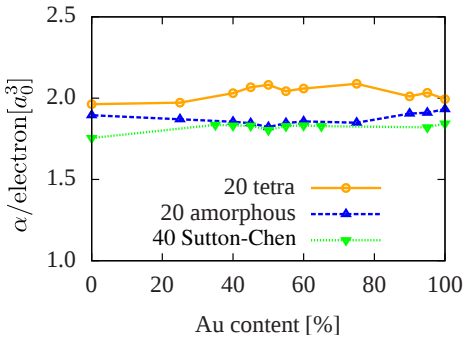

Figure 3.13: The static electric dipole polarizability α per electron for 20-atom tetrahedral and amorphous as well as 40-atom Sutton-Chen potential clusters.

Fig. 3.13 shows α normalized to the number of electrons as a function of the Au content for the 20-atom tetrahedral and amorphous clusters, as well as for the 40-atom Gupta-clusters. For these systems α does not exhibit any special features at a certain Au-Pt ratio, but is nearly constant.

Another property, that has long been known to be directly related to the reactivity of a material is its DOS. The first model that was able to explain the reactivity of a variety of simple and transition metal surfaces towards hydrogen chemisorption was developed by Newns in 1969[2] and is essentially similar to the model Hamiltonian suggested by Anderson to describe the interaction of a single magnetic impurity with a free electron gas [136, 137]. The *Newns-Anderson model* was subsequently simplified to what became known as the *d-band-model* [105, 138]. In this model the adsorbate-surface interaction is formally separated into the interaction of the adsorbate with the metal *s*- and *p*-states and the metal *d*-states. As the former are assumed to be similar for all transition metals, the chemisorption energy finally only depends on the energetic position of the *d*-band center.

Consider, as a simple example, the chemisorption of H_2 on four metal surfaces of very different reactivity (Ni, Pt, Cu and Au). First, the hydrogen $1s$ state interacts with the metal $4s$ (Ni, Cu) or $6s$ (Au, Pt) band[3] leading to a broadening and lowering of the adsorbate-induced level. This part of the interaction should essentially be the same for all four metal surfaces. The adsorbate induced level, in the second step, interacts with the metal-*d*-states.

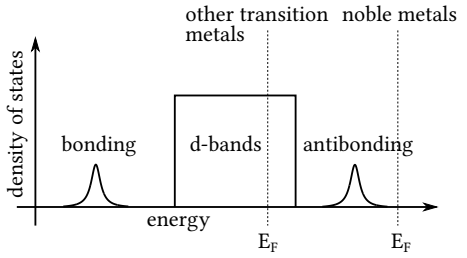

Figure 3.14: Illustration of the *d*-band model adapted from Ref. [105]. The two-step mechanism of an adsorbate interaction with a metal surface is explained in the main text.

As the latter are assumed to be tightly localized, they are modeled as a single level. Thus the interaction between the adsorbate induced level and the *d*-band can be seen as a simple two-level interaction. This results in an energetically deep-lying bonding state and an antibonding state. Fig. 3.14 illustrates that the filling of the antibonding state and thus the chemisorption energy to zeroth order depend on the energetic position of the metal *d*-band with respect to the Fermi energy, because if the metal-*d*-band is close to the Fermi energy, the antibonding state can

[2]Noteworthy here is, that Newns even suggests an explanation for the catalytic conversion of para- to ortho-hydrogen on Au-Pd alloy surfaces.

[3]The terms *s*-band and *d*-band are rooted in the tight binding approach to the solid state. An *s*-band, e.g., arises from weakly interacting atomic *s*-states localized at the lattice points.

be shifted right above it and will therefore be empty. For Pt and Ni this is the case leading to a net attractive interaction between adsorbate and surface, while Au and Cu have filled antibonding states. This finding rationalizes the high inertness of Au, but it has also been used to explain the high catalytic activity of small Au NP [9] as well as that of many other systems (see Ref. [131] and references therein).

Considering the complete *d*-band of Au-Pt nanoalloys requires two assumptions that do not necessarily have to be valid in our case. Firstly, the *d*-band also comprises of unoccupied states above the Fermi energy. The physical interpretability of KS eigenvalues, however, can only safely be assumed for the upper occupied part of the eigenvalue spectrum [48]. Secondly, in small transition metal clusters the definition of a metal-*d*-band in the spirit of the tight binding approach is not *per se* clear. What is typically done in cases like this is, that the atomic-*d*-character of the KS eigenstates is tested by projecting them onto atomic-*d*-orbitals. The DOS is defined as

$$g(\varepsilon) = \sum_i \langle\varphi_i|\varphi_i\rangle \delta(\varepsilon - \varepsilon_i). \tag{3.5}$$

If the KS orbitals $|\varphi_i\rangle$ are expanded in an orthogonal basis of localized atomic functions $|\phi_\mu\rangle$, i.e., $|\varphi_i\rangle = \sum_\mu c_\mu^{(i)} |\phi_\mu\rangle$, then the definition of the projected DOS (PDOS) is straightforward:

$$g_\mu(\varepsilon) = \sum_i |c_\mu^{(i)}|^2 \delta(\varepsilon - \varepsilon_i) = \sum_i |\langle\phi_\mu|\varphi_i\rangle|^2 \delta(\varepsilon - \varepsilon_i). \tag{3.6}$$

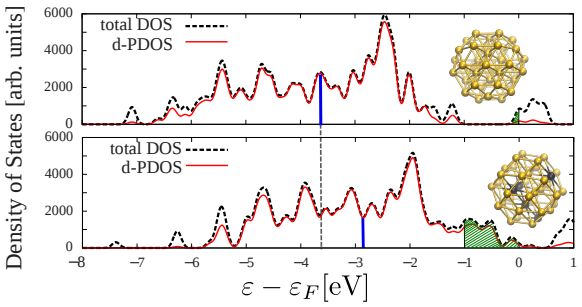

Figure 3.15: The DOS and PDOS for Au_{38} and $Au_{33}Pt_5$.

Here,[4] this is not the case. An overlap matrix element $S_{\mu\nu} = \langle\phi_\mu|\phi_\nu\rangle$ enters the definition of g_μ. There are several ways how to treat these overlap terms, one prominent example being the Mulliken population analysis [139]. As results can differ significantly, depending on which method is chosen, the interpretation of PDOS requires special care and is often only meaningful in comparison with a reference system. We therefore concentrate here on the total DOS close to the Fermi level, which we define as the DOS integrated from the Fermi level down to 1 eV below the Fermi level. The results reported in the following are robust toward changing the integration threshold to slightly smaller or larger values. Reassuringly, Fig. 3.15 illustrates for the truncated octahedral clusters Au_{38} and $Au_{33}Pt_5$ that an increase of the DOS at the Fermi level (indicated by the green shaded area) coincides with an upshift of the center of gravity (vertical blue line) of the d-PDOS for Au-Pt nanoalloys.

[4] Using the TURBOMOLE program package for all calculations in which basis functions do not form an orthogonal set.

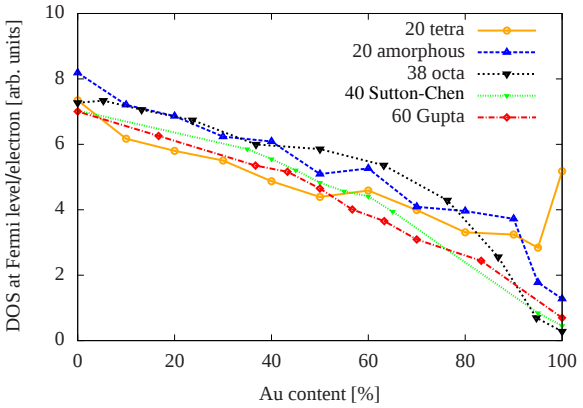

Figure 3.16: The DOS at the Fermi level (integration threshold defined as -1 eV) as a function of the Au content of 20-atom tetrahedral and amorphous, 38-atom truncated octahedral and 40- and 60-atom Gupta-potential clusters.

We can now analyze the DOS at the Fermi level for a variety of Au-Pt NP with different overall geometries and mixing patterns. Fig. 3.16 shows that it increases with increasing Pt content for 20-atom tetrahedral[5] and amorphous clusters (core-shell), for 38-atom truncated octahedra (random) and for 40- and 60-atom Gupta-potential clusters (core-shell). Importantly, this trend is independent of the specific way in which Au and Pt atoms are arranged in the cluster, i.e., the DOS at the Fermi level increases both for core-shell and randomly mixed Au-Pt nanoalloys with increasing Pt content. This finding suggests that the binding energy between Au-Pt nanoalloys and an adsorbate should increase with increasing Pt content and that a pure Pt NP should bind adsorbates most strongly to its surface. From this perspective, a certain Au-Pt ratio could correspond to an optimal binding energy in a specific reaction in terms of Sabatier's principle.

A closer look at the local electronic structure reveals that the addition of Pt is beneficial from yet another perspective. Fig. 3.17 shows isosurface plots of the highest occupied KS orbital (HOMO) of several Au-Pt NP. The HOMO has physical relevance as it asymptotically dominates the density and its exponential decay is governed by the first ionization potential, i.e., it represents the spatial distribution of the energetically highest lying part of the density. Fig. 3.17 reveals that the spatial location of the HOMO is closely related to that of the Pt atoms. The two $Au_{10}Pt_{10}$ clusters at the top of Fig. 3.17 differ only in the position of one Pt atom that sits within the bottom facet on the left side and is moved to the top corner on the right side of Fig. 3.17. This slight rearrangement results in a marked change of the spatial distribution of the HOMO density. The same effect can be seen for the two $Au_{20}Pt_{20}$ homotops at the bottom of Fig. 3.17 and all other systems that we studied. This has two important consequences: Firstly, as the Pt content increases, more Pt atoms are located at the surface of the cluster, so that the HOMO can extend away

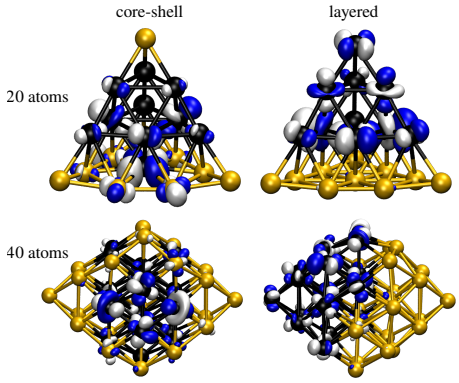

Figure 3.17: Plots of the highest occupied molecular orbital at ± 0.04 $a_0^{-3/2}$. Top: for two just slightly different $Au_{10}Pt_{10}$ clusters. Bottom: $Au_{20}Pt_{20}$ with core-shell and layered mixing pattern, respectively.

[5]Note, that the Au_{20} tetrahedron is the only exception that we found for this observation. We attribute this deviation to the unusual electronic structure of Au_{20} [68].

from the surface. Secondly, the known importance of the surface for catalytic processes is enhanced in Au-Pt nanoalloys, not only due to the increased surface-to-volume ratio on the nanoscale, but also because of the presence of Pt, the many possible distributions of Au and Pt on the surface and the resulting implications for the local electronic structure of the system.

3.4.2 Electronic structure of Au-Pd nanoalloys

Au-Pd nanoalloys show an electronic structure very similar to that of Au-Pt nanoalloys. There is but one point requiring special attention in small Au-Pd nanoalloys that can be neglected in Au-Pt NP: their spin polarization. Bulk Au and Pd are not magnetic, but high magnetic moments have been reported for small Pd clusters [140]. We start from the bilayered ground state of Pd_{13} taken from Ref. [140], step-by-step replacing lowly-coordinated Pd atoms by Au as suggested in Ref. [141, 142]. The resulting Au_nPd_{13-n} (n=0-13) structures were then locally relaxed.

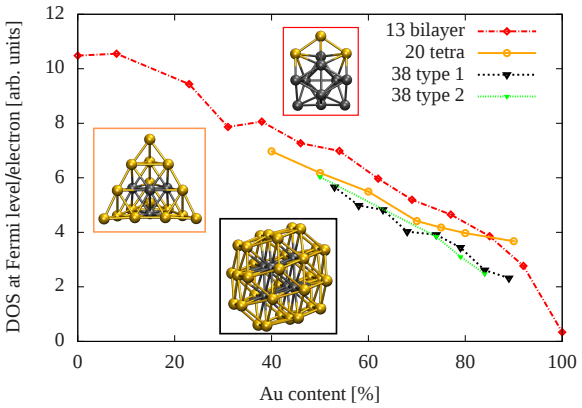

Figure 3.18: The DOS close to the Fermi level as a function of the Au content for Au/Pd particles. For all three sizes (13-atom, 20-atom and 38-atom) the DOS decreases with increasing Au content. For the 38 atomic clusters the DOS for two different structure types is shown. The trend is the same for both types.

We allowed and checked for spin polarization, evaluating the total energy for different multiplicities. We found that for the purposes of this study the magnetization is not decisive, as the DOS at the Fermi level depends only very little on the spin polarization in the cases that we studied. The integrated DOS typically changes by less than 1% for most structures as a function of magnetization, and a few percent at most. For the sake of completeness, some magnetizations are, however, reported in the following. The resulting magnetic moments are $6\,\mu_B$ for Pd_{13}, $3\,\mu_B$ for $Pd_{12}Au_1$, $4\,\mu_B$ for $Pd_{11}Au_2$ and $2\,\mu_B$ for Pd_9Au_4. Clusters with larger Au contents are either singlets or triplets depending on whether their electron number is odd or even. The DOS at the Fermi level is then defined as for Au-Pt NP and shown in Fig. 3.18 as a function of the particles' composition (red diamonds). The red inset depicts the structure of Au_3Pd_{10} as an example. From the figure one can clearly draw the conclusion that again the DOS at the Fermi edge decreases with increasing Au amount.

In order to check whether this behavior of the DOS is general we repeated the procedure for larger clusters. Our choice of further test systems was motivated by similar considerations as in the case of Au-Pt NP. The experimental studies are concerned with relatively large particles that show a bulk-like structure [132]. Therefore, we also theoretically focus on investigating systems where a bulk-like geometry is a reasonable starting point. Furthermore, as bulk Pd and Au are not magnetic, and as the experimentally observed particles are

bulk-like in their structure, it is a plausible assumption that magnetic effects are not important for explaining the catalytic properties. In addition, our study of the 13-atom clusters has shown that the total DOS is not very sensitive to the magnetization. Therefore, we choose for our following investigations always the electronic configuration that has the lowest spin polarization (under the condition that the aufbau principle is respected). From the just described points of view the Au_{20} tetrahedron is again a good starting point for the theoretical investigation. We replaced Au by Pd as explained in Sec. 3.2 with Pt, again observing the rule that high-coordination number sites are energetically favorable for Pd. The orange inset of Fig. 3.18 shows the structure of $Au_{16}Pd_4$ as an example and the DOS at the Fermi level as a function of the Au content. Also in this case an increase with increasing amount of Pd is observed for all mixed Au/Pd particles. This observation does not depend on the specific structural motif.

To demonstrate this explicitly and to check another cluster size we repeated the procedure for the truncated octahedral 38-atom clusters. We studied two lines of structures with 38 atoms. In both of them 6 Pd atoms form the core (see black inset of Fig. 3.18), as this is an energetically favored arrangement. However, the two lines differ in the position of the remaining "surface" Pd atoms. The structures labeled "type 1" in Fig. 3.18 were obtained by randomly replacing surface Au by Pd atoms. In the structures labeled "type 2" the surface Pd atoms were placed such that they occupy the interior parts of the facets. In the literature [141] these latter configurations have been reported as being energetically favorable. Our calculations confirm this finding as structures of type 2 are lower by 0.08 eV for $Au_{30}Pd_8$ and 0.83 eV for $Au_{28}Pd_{10}$ than the corresponding structures of type 1. We observe that all structures have rather small HOMO-LUMO gaps, which may be an indication for further symmetry breaking being energetically favorable. The important finding is that also in the 38-atom faceted cases both types of structures show the same trend: the DOS at the Fermi level increases with increasing Pd content. Again this finding could imply that, in terms of Sabatier's principle, a certain Au-Pd ratio might correspond to optimal adsorbate binding energies in a certain reaction.

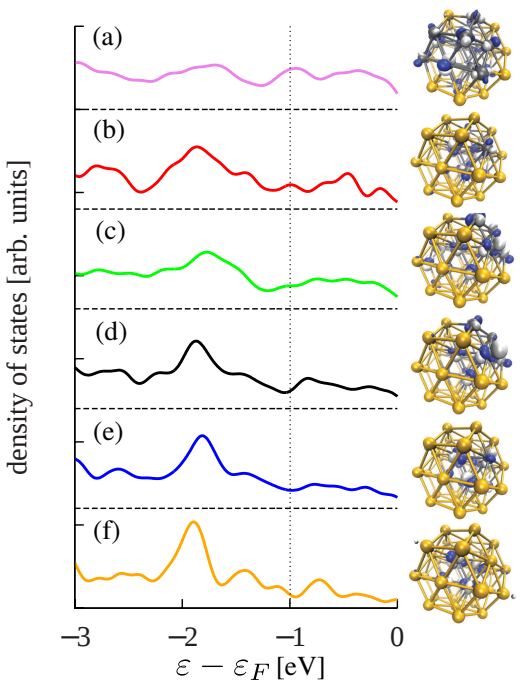

Figure 3.19: Right: geometric structure and isosurface plot of the HOMO of 38-atom particles. From top to bottom: (a) $Au_{19}Pd_{19}$, (b)-(d) 3 different structures for $Au_{28}Pd_{10}$, (e) $Au_{30}Pd_8$, (f) $Au_{32}Pd_6$. White and blue areas represent negative and positive isosurface values of 0.04 $a_0^{-3/2}$. Left: the DOS of each of the clusters.

In the next step, following the same reasoning as before, we investigate the relation between the clusters' geometry and their electronic structure. To this end we take a closer

look at several of the faceted 38-atom particles. The right side of Fig. 3.19 shows from top to bottom structures and HOMO densities of $Au_{19}Pd_{19}$, three different $Au_{28}Pd_{10}$ homotops, $Au_{30}Pd_8$ and $Au_{32}Pd_6$. The left column depicts the occupied DOS with the respective Fermi levels aligned at 0 eV. The vertical line at -1 eV indicates the previously mentioned integration range.

The conclusions that can be drawn from Fig. 3.19 are rather similar to the Au-Pt NP case: First, the HOMO in each case is closely associated with the Pd atoms. Second, an increasing amount of Pd brings an increasing number of Pd atoms to the surface and thus leads to a HOMO that is dominantly located at the surface of the cluster. This is clearly seen, e.g., when comparing the HOMO representation of $Au_{32}Pd_6$ to the one of $Au_{19}Pd_{19}$ and it indicates that Pd atoms at the surface are likely to be favorable in terms of the particles' activity. Third, we carefully inspect three homotops of $Au_{28}Pd_{10}$. Structure (b) as suggested in the literature [141] has the lowest total energy, (d) is higher by 0.83 eV and (c) by 1.64 eV. Independent of these energetic differences, there is an important observation to be made in comparing structures (b)-(d): although the three geometries are overall rather similar, the differences between the HOMOs are quite noticeable. A moderate change in the geometry leads to a significant change of the energetically high-lying part of the density. Thus, a specific arrangement of Au and Pd atoms at the surface can lead to special electronic and thus chemical properties.

3.4.3 The role of Au in Au-Pt nanoalloys

In the spirit of Ref. [131] and as explained in the introductory paragraphs of Sec. 3.4 one could speculate that a synergistic effect in Au-Pt nanoalloys for a specific reaction could in principle be explained by linking a catalytic descriptor of this reaction to the DOS at the Fermi level. One could then argue that the binding energy between Au-Pt NP and the specific reactants must neither be too strong nor too weak for the reaction to take place, in compliance with Sabatier's principle. An optimal Au-Pt mixing ratio would then emerge from these considerations. Even though this point of view is perfectly legitimate and has led to valuable insights into gas-phase catalysis on surfaces under well-controlled conditions, it is not easily applicable in our case as mentioned before. However, as a synergistic effect is observed in many different reactions with different matrices and solvents, we suggest that fundamental properties of Au-Pt NP that are independent of the reaction lead to the special properties of Au-Pt NP. With the DOS at the Fermi level and the spatial arrangement of the HOMO density being determined by Pt as discussed earlier, we now want to ask the question which fundamental catalysis-favorable property is associated to Au.

Here, I want to argue that this property is the mobility of atoms in the Au-Pt systems, or the NP fluxionality. Fluxionality has been recognized to be of crucial importance for the catalytic activity of clusters and surfaces [143]. It can be a primer for the ability to structurally adjust to reactants, form active sites [144] and directly influences turnover rates by affecting the catalysts' ability to regenerate after the reaction. In order to determine how easy it is for atoms to rearrange in Au-Pt systems we performed two types of studies.

In the first one we take the perspective that with respect to catalytic activity, the surface of the NP, which for faceted NP is similar to a bulk surface, is likely their most important

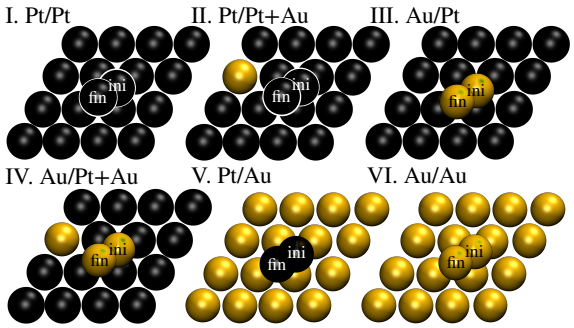

Figure 3.20: Sketch of the setup used for the study of Au and Pt adatom self-diffusion from a fcc (ini) to a hcp (fin) hollow position. The systems we studied were: I. Pt adatom on pure Pt(111) surface, II. Pt adatom on Pt(111) surface with single Au atom in top surface layer, III. Au adatom on pure Pt(111), IV. Au adatom on Pt(111) doped with Au, V. Pt adatom on Au(111) and VI. Au adatom on Au(111).

part. When reactants approach the surface, the surface may structurally react to form active sites. The induction time, i.e., the time that goes by before the reaction starts, seen in NP catalysis can be an indication for such processes [80, 132, 145]. A canonical step in surface restructuring is the movement (diffusion) of atoms on the surface. Therefore, we chose the height of the barriers for the diffusion of Au and Pt adatoms on pure and doped Pt- and Au-surfaces as a measure for the surfaces' ability to restructure. As an aside we note that this line of thinking is also supported by the observation that bimetallic effects as well play a role in Au-Pt surfaces [115] as mentioned before.

system	E_{ads} fcc	E_{ads} hcp	$E_{barrier}$
Pt/Pt	4.60	4.82	312
Pt/Pt+Au	4.61	4.76	287
Au/Pt	2.77	2.87	177
Au/Pt+Au	2.79	2.86	165
Pt/Au	4.05	4.15	143
Au/Au	2.50	2.56	115

Table 3.3: Adsorption energies (in eV) of Pt- and Au-adatoms in pure and doped Pt- and Au surfaces for the start and the end position of each NEB calculation. For a definition of the diffusion barrier (in meV) see text.

For calculating these diffusion barriers we rely on the NEB method (see Sec. 2.5). It allows to determine the minimum energy path between a given initial and final state. If this minimum energy path goes through one or several maxima as a function of the reaction coordinate the largest of these barriers can be regarded the rate-determining step of the reaction. Calculations were carried out with VASP using the PBE GGA [24] and employing the PAW method to describe the electron-ion interaction [64, 67] (see Sec. 2.4). Technical details regarding these calculations can be found in Appendix C. The cutoff-energy for the plane wave basis set was set to 450 eV. Pure and doped Pt and Au fcc(111) surfaces were modeled by 4-layer slabs containing 4x4 atoms in each layer and being separated by 20 Å of vacuum. The bottom two layers were held fixed at the Pt (Au) bulk equilibrium distance of 3.977 (4.174) Å, while the other layers were allowed to fully relax. The Brillouin-zone integrations were performed using Monkhorst-Pack k-point meshes of 5x5x1 size. We considered a diffusion step from a fcc to a hcp hollow site for different combinations of surfaces and adatoms, as depicted in Fig. 3.20. In all cases the diffusion barrier was defined as the energetic difference between the transition state and the hcp adsorption site, this being the largest energy difference and thus determining the rate of this particular diffusion

step. In addition to the diffusion barriers we determined the adsorption energies (see Tab. 3.3) of the adatoms at the fcc and hcp hollow site as

$$E_{\text{ads}} = E_{\text{slab}} + E_{\text{adatom}} - E_{\text{slab+adatom}} \tag{3.7}$$

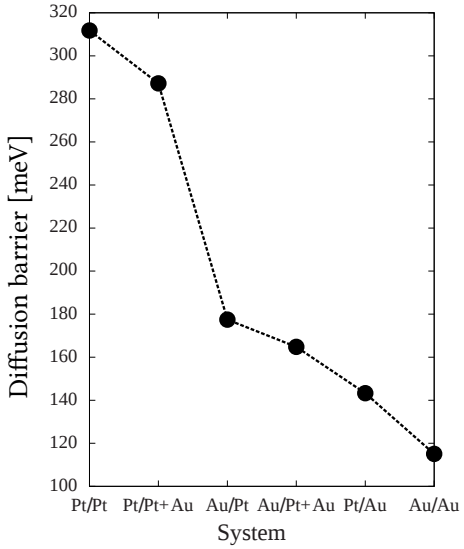

Figure 3.21: Barrier for Pt- and Au-adatom diffusion on Pt-surfaces with and without Au doping and on a pure Au-surface. An explanation of the notation can be found in Fig. 3.20.

Fig. 3.21 shows that diffusion of a Pt adatom on a pure Pt surface has the highest barrier of all considered systems. This is in line with the Pt adatom being most strongly adsorbed to the pure Pt surface. Yet, the insertion of one Au atom into the Pt surface lowers the diffusion barrier by about 25 meV. A similar effect can be seen by comparing the diffusion barrier of an Au adatom on a pure Pt surface and on a Pt surface with one Au dopant. It is particularly interesting that the diffusion barrier decreases even more for a Pt adatom on a Au surface. In this case the adsorption energy is almost as high as that of Pt on Pt(111) leading one to expect an equally high diffusion barrier. The facilitated surface diffusion on surfaces with a higher Au content can therefore not only be explained by Au adatoms being more weakly bound to the surface than Pt adatoms. We interpret this finding as an increased ability of Au-alloyed Pt-surfaces to undergo structural changes and thus as a higher surface fluxionality with increasing Au-content.

In the second type of study that we did in order to show that increasing amounts of Au increase the atomic mobility in Au-Pt NP we moved away from the surface perspective and regarded the NP as finite clusters. The fluxionality of small Au clusters has recently been shown by extensive scans of their potential energy surfaces [146]. This method, however, is not feasible for Au-Pt nanoalloys in the experimentally relevant size range. Therefore, we performed one nanosecond long MD simulations for randomly mixed truncated octahedral clusters (38, 201 and 586 atoms) and for 60-atom and 100-atom Gupta potential based core-shell clusters to obtain a measure of the mobility of the cluster atoms in terms of their mean square displacement (MSD)

$$\langle \hat{r}^2 \rangle = \left\langle \frac{1}{M} \sum_{i=1}^{M} (\boldsymbol{R}_i(t) - \boldsymbol{R}_i(t=0))^2 \right\rangle, \tag{3.8}$$

where M is the number of atoms in the cluster and $\boldsymbol{R}_i(t)$ is the position of atom i at time t. The angle brackets indicate a time average. The MD simulations were done using the DL_POLY program [126] and the NVT Evans ensemble with the same many-body Sutton-Chen potential as in Sec. 3.3 to describe the potential energy of the system.

Randomly mixed Au-Pt NP segregate to $\text{Au}_{\text{shell}}\text{Pt}_{\text{core}}$ structures even at comparably modest temperatures and short simulation times. As our aim was to retain the homogenous

mixing pattern of the truncated octahedra all simulations were carried out at 300 K. This lies well below the melting point of most of these systems [6], meaning that the MSD averaged over the whole simulation time is approximately zero. However, at shorter timescales of 1000 fs a diffusive motion of Au and Pt atoms takes place. The time average in Eq. 3.8 was therefore computed for subsequent time windows of 1000 fs. For each Au-Pt mixing ratio three simulations were carried out to minimize statistical uncertainties. Note that even though this method yields only an approximation to the diffusion of cluster atoms, it can be used to compare the short-time atomic mobility of nanoalloys with varying mixing ratios.

For NP in the size regime that we are concerned with the high surface-to-volume ratio can have significant impact on the average MSD of the NP. Atoms at lowly coordinated positions, e.g., at kinks or edges can show MSDs that are considerably larger than those of highly coordinated volume atoms or atoms in a surface plane. For irregular NP like the 60-atom and the 100-atom NP this effect is more pronounced than it is for the regular truncated octahedra with their magic atom numbers of 38, 210 and 586. To obtain comparable MSD values it is therefore necessary to keep the geometries of NP with the same number of atoms but different Au-Pt ratios as close as possible. For the irregular 60-atom and 100-atom clusters this makes a full geometry optimization prior to MD simulations necessary. Nevertheless, the MSDs of these NP show large statistical variations as compared to the MSDs of the truncated octahedra. For this reason we want to stress that we are not concerned with evaluating the exact value of the MSD in our NP. In contrast, we want to study the trend that the MSD shows with increasing Au content.

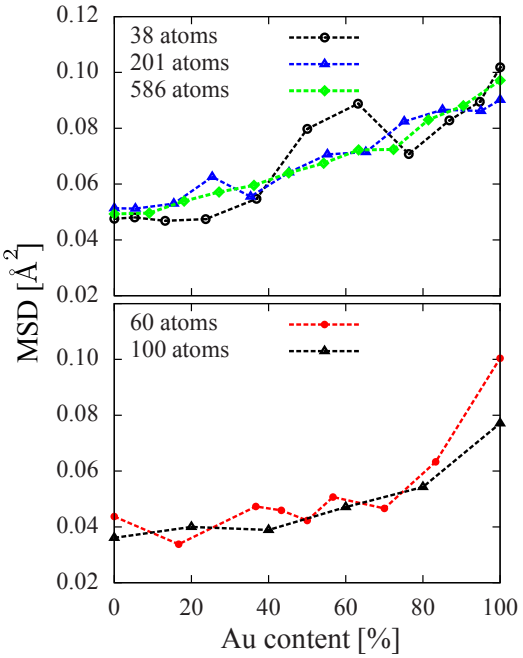

Figure 3.22: Top: MSD from MD simulations of truncated octahedral clusters that are solid solutions of Au and Pt with 38, 201 and 586 atoms. Bottom: MSDs of 60-atom and 100-atom core-shell particles.

The resulting MSDs are depicted in Fig. 3.22: the truncated octahedra at the top and the 60-atom and 100-atom core-shell particles at the bottom. It can clearly be seen that the composition-dependent trend is the same for all clusters: The MSD increases with increasing Au-content. This is again independent of particular geometric configurations or mixing patterns. Thus, although being of very different nature, the MD study confirms the conclusions drawn from the surface diffusion barrier calculations: structural flexibility increases with an increasing amount of Au.

[6] The melting point of the 60-atom clusters lies below 300 K. Therefore in this case MD simulations were carried out at a temperature of 200 K.

3.4.4 Combining electronic structure and fluxionality

We can now put together all the findings. The DOS of Au-Pt NP develops properties that one naturally associates with being favorable for catalysis with increasing Pt content, whereas the structural flexibility increases with increasing Au content. Therefore, for each reaction there can be an ideal ratio of Au and Pt that yields overall optimal properties. This is visualized in Fig. 3.23. It shows the volcano-like plot that one obtains by multiplying a polynomial least squares fit to the DOS at the Fermi level and the MSD. This has here been done for the 38-atom and 60-atom clusters, as for these systems we could access both quantities (see Fig. 3.24).

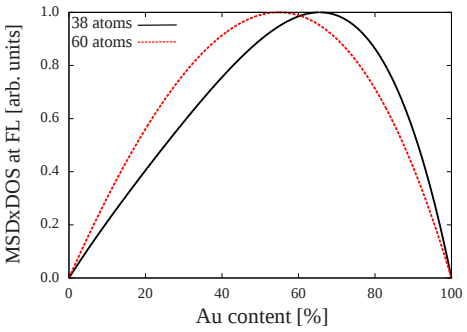

Figure 3.23: Product of a polynomial least squares fit to the DOS at the Fermi level (FL) and MSD for 38-atom and 60-atom Au-Pt clusters as a function of Au content. Quantities are scaled so that for 0 and 100% Au content the curves intersect the y-axis at 0 and have a maximum value of 1.

An ideal Au-Pt mixing ratio emerges as a consequence of the interplay between structural fluxionality provided by Au and a favorable electronic structure contributed by Pt. Of course what this ideal mixing ratio is will sensitively depend on the reaction, experimental conditions, as well as on the exact structure and mixing pattern of the catalysts. Yet, the point that Fig. 3.23 emphasizes is that synergistic effects

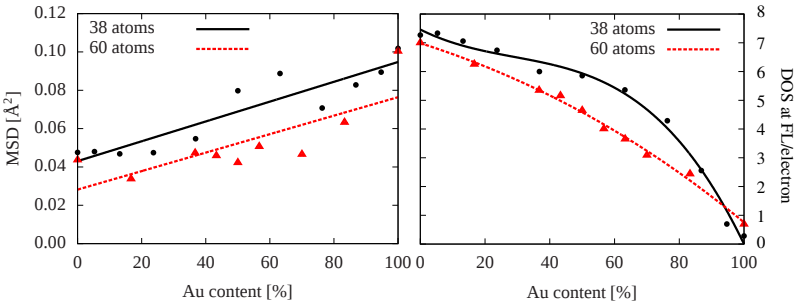

Figure 3.24: Left: MSD and linear fit to MSD of 38-atom (black triangles) and 60-atom (red triangles) clusters. Right: DOS at the Fermi level for 38-atom and 60-atom clusters. For constructing the "volcano" plot the data was fitted with a cubic polynomial.

in Au-Pt NP are expected on rather general grounds and regardless of the specific chemical reaction and environment. Additionally, Fig. 3.23 illustrates another point. We do not expect "the whole to be greater than the sum of its part". The synergistic or rather bimetallic effect in Au-Pt nanoalloys emerges as a consequence of adding up catalysis-favorable fundamental physical properties of Au and Pt. The effect of the combined properties might be amplified by the high surface to volume ratio in NP, the presence of steps and kinks that act as active sites in catalysis [144] and the elongated average bond lengths resulting from thermal expansion (see Sec. 3.3) or NP-matrix interactions (see Appendix A). Different to what the buzzword "synergy" suggests, Au-Pt nanoalloys might not possess special catalytic properties that go beyond a combination of the properties of pure Au and Pt NP.

4

Magnetic-to-nonmagnetic transition in Mn-doped Si-clusters

4.1 Dilute magnetic semiconductors

Semiconductors doped with few impurities that carry a magnetic moment are called dilute magnetic semiconductors. During the last decades they have been subject of intense study, after it had been observed that the introduction of a small fraction of magnetic impurities would leave the favorable transport and optical properties of the semiconductors unchanged, at the same time being accompanied by large magnetic moments and many interesting magnetic order phenomena. To name only one example, it has been shown by Ohno et al., that (Ga,Mn)As exhibits ferromagnetic order up to temperatures as high as 110 K [147]. Later theoretical work provided a model for the origin of this ferromagnetic ordering and predicted materials with Curie temperatures even exceeding room temperature. Even though it is believed today that dilute magnetic semiconductors with such high Curie temperatures may not be realizable, the field nevertheless bears plenty of fundamental questions, many of which are still unanswered.

The seemingly simplest of these questions is how a single magnetic impurity interacts with the semiconducting host, i.e., whether the impurity's magnetic moment is quenched or survives. Pioneering studies have been conducted by Ludwig and Woodbury in the 1960s using electron-paramagnetic resonance spectroscopy to investigate magnetic properties of Si doped with a range of $3d$ transition metal impurities at substitutional and interstitial positions [148]. Furthermore, Ludwig and Woodbury provided a simple and descriptive model to predict quenching or survival of the magnetic moment of the transition metal impurity.

The model (illustrated in Fig. 4.1) assumes that the degenerate atomic $3d$ states of the transition metal impurity are split into three t_g and two e_g levels under the influence of the crystal field of the host material. These levels are then filled according to Hund's rules with all valence electrons that do not participate in bonding. A Mn^+ impurity, e.g., with 6 valence electrons would give rise to a magnetic moment of $4\,\mu_B$ in an interstitial position (top), but only $2\,\mu_B$ in a substitutional position (bottom), where 4 of its 6 valence electrons participate in bonding to the Si host. This simple model has been widely accepted and its microscopic justification and validity range have been tested [149]. Yet, it relies, despite it seeming simplicity, on some *ad hoc* assumptions that might not be justified in general, such as the validity of the crystal field model and the filling of the energy levels according to Hund's rules.

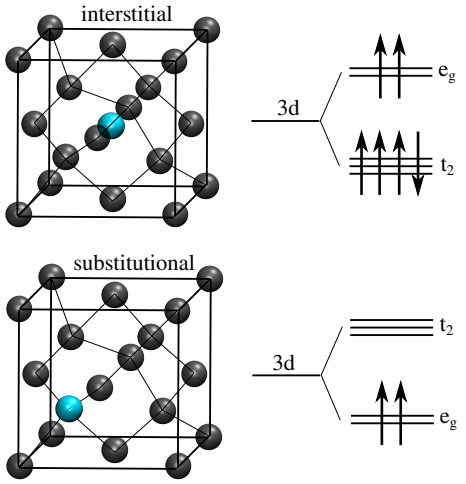

Figure 4.1: Sketch of the Ludwig-Woodbury model for a Mn^+ impurity in bulk Si at an interstitial (top) and a substitutional (bottom position. The $3d$ levels are filled according to Hund's rules with all valence electrons that do not participate in binding, resulting in a total magnetic moment of $4\,\mu_B$ for interstitial and $2\,\mu_B$ for substitutional Mn^+.

In recent years, a wealth of experimental and theoretical studies have been devoted to transition metal doped semiconductors [150–154], nanocrystals [155–157] and clusters [158–162]. While the results of these studies for bulk Si and Si nanocrystals are mostly consistent with each other[1], cluster studies partly arrive at contradictory conclusions. Ngan et al., e.g., predict high magnetic moments for endohedrally doped $MnSi_n^+$ ($n = 12 - 14$) [161], while Palagin et al. show that the magnetic moment of Mn encapsulated in Si cages of the same size range is quenched and can only be restored by considerably increasing the size of the surrounding cages by hydrogen passivation [162]. These inconsistencies are most likely rooted in the notoriously difficult theoretical description of systems containing transition metal elements, as will be explained in Sec. 4.2.

The realization of an experiment which allows to study the local electronic and magnetic properties of a single magnetic impurity with a nonmagnetic host material is complicated by possible inhomogeneities in the host, coalescence of the impurity atoms and long-range interactions between single impurities. One way to overcome these difficulties is to study, instead of bulk samples, size-selected gas-phase clusters with single transition metal impurities as a model system. Furthermore, this approach allows excellent comparability with theoretical predictions, as small clusters, despite difficulties that can arise in conjunction with finding their global minimum structure, are particularly well-defined systems. Our study of the magnetic-to-nonmagnetic transition in Mn-doped Si clusters, that has been carried out in collaboration with experiment, is presented in Sec. 4.3.

[1] Although the prediction of the exact size of the impurity's magnetic moment differs depending on the level of theory and the exact type of system that is studied.

4.2 Strong correlation in Density Functional Theory

From a theoretical point of view dilute magnetic semiconductors belong to a class of systems often dubbed *strongly correlated*. (Strong) correlation between electrons is a problem for most quantum chemistry methods. It is, however, particularly DFT that has become infamous for notoriously yielding wrong results when it comes to strongly correlated materials. While it does not warrant further explanation that an exact DFT treatment would in principle yield exact ground state energies and densities also for strongly correlated systems, the bad reputation of DFT in the "strong correlation community" needs some comment: Firstly, DFT owes its rise and widespread popularity to the overall satisfying results and comparably low computational cost of standard (semi)local functionals for many interesting systems. The very same xc functionals, however, are the ones that fail the most badly for strongly correlated materials. Secondly, also more sophisticated functionals have so far not been able to yield consistently accurate results for different systems in which correlation plays a major role and in fact it is not obvious, why the physics buried in such systems should be exactly representable in terms of an auxiliary system of noninteracting electrons [163].

In quantum chemistry correlation is defined as the difference between the exact total energy and the Hartree-Fock energy of a system $E_\mathrm{c} = E_\mathrm{exact} - E_\mathrm{HF}$. A caveat to this definition is that the single Slater determinant of Hartree-Fock theory of course does include correlations between electrons in the sense that a Slater determinant is a correctly antisymmetrized product wavefunction, and thus obeys the Pauli exclusion principle. Two electrons having the same spin avoid each other and can in this sense be regarded as correlated. From a wavefunction perspective, electron correlation (apart from Pauli exclusion) refers to all many-body effects which make more than a single Slater determinant necessary to capture the system's electronic structure correctly.

Qualitatively these effects can be divided into two groups called *dynamical* and *static* correlation. One speaks of dynamical correlation in situations where a linear combination of many Slater determinants is necessary to describe the Coulomb repulsion between electrons. As this interaction is screened by all other electrons in the system, dynamical correlation is a short-range effect. Static correlation on the other hand arises when only a few degenerate or nearly degenerate Slater determinants cover the electronic structure correctly. A prototypical example is the dissociation of H_2 and other molecules, but also the triple bonds in N_2. This long-range correlation effect is not covered by (semi)local correlation functionals [2].

To gain deeper insight into the failure of many xc functionals in describing strongly correlated systems, we have to get back to a concept already introduced in Sec. 2.5: the

[2]Static correlation can however be mimicked by semilocal exchange functionals [164]. This observation also rationalizes a linear combination of semilocal and exact exchange in one-parameter hybrid functionals as introduced in Sec. 2.5.

SIE. It was mentioned before that the SIE is trivially defined in an one-electron system and that the effective one-electron form of the KS equations suggests a route to remove the one-electron SIE in an orbital-by-orbital fashion (Perdew-Zunger SIC [21]). Yet, despite its success in curing many troublesome features of the underlying xc functional, Perdew-Zunger SIC is by no means able to correctly describe the electronic structure and properties of all systems. In fact, some of its failures can be related to the before mentioned importance of static correlation effects and their modeling by semilocal exchange.

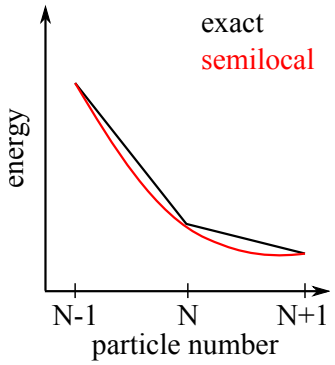

Figure 4.2: Sketch of the total energy of a system as a function of the fractional particle number. For the exact energy functional this has to be a series of straight line segments with kinks at integer particle numbers giving rise to a derivative discontinuity of the chemical potential.

It has therefore been attempted to define a many-electron SIE [165]. The ground for this definition was laid in a seminal work of Perdew et al. [166], in which a system of two initially neutral atoms A and B at large distance was considered. When a fraction of charge δ is transferred from atom A to atom B, the total energy of the system must vary linearly with δ and have a discontinuity at integer particle numbers as illustrated in Fig. 4.2. Otherwise the system could minimize its energy by distributing fractional charges on each of the atoms A and B thereby violating the principle of integer particle preference. This means that

$$E(N+\delta) = (1-\delta)E(N) + \delta E(N+1), \tag{4.1}$$

where $N+\delta$ is the fractional particle number and $0 \leq \delta \leq 1$[3]. The derivative of E with respect to the particle number can be associated with a chemical potential μ. The discontinuity of E implies that μ can jump at integer particle numbers. This behavior is known as the *derivative discontinuity* and it has together with the *straight-line condition* for fractional particle numbers important consequences for the correct description especially of strongly correlated systems within KS DFT.

The first consequence is related to the so called *band gap problem* of DFT. The fundamental gap is defined via the difference of the ionization potential and the electron affinity of the N electron system and can be expressed by virtue of the highest occupied KS eigenvalues of the N and the $N+1$ electron system

$$E_{\mathrm{gap}} = I(N) - A(N) = \varepsilon_{\mathrm{HOMO}}(N+1) - \varepsilon_{\mathrm{HOMO}}(N). \tag{4.2}$$

The energetic difference between the HOMO and the LUMO of the N electron system, the KS-gap, E^{KS} differs from E_{gap} by the derivative discontinuity Δ_{xc} which can hence be expressed as

$$\Delta_{\mathrm{xc}} = \varepsilon_{\mathrm{HOMO}}(N+1) - \varepsilon_{\mathrm{LUMO}}(N). \tag{4.3}$$

The ionization potential and the electron affinity can be related to the derivative of the energy to the left and the right of the discontinuity at N by using the definition of the

[3] Fractional particles numbers can arise as time averages in open systems that can be treated as statistical ensembles.

chemical potential $\mu = \partial E/\partial N$ and the Euler equation of DFT, $\mu = \delta E[n]/\delta n(\boldsymbol{r})$:

$$-A(N) = E(N+1) - E(N) = \lim_{\delta\to 0} \left.\frac{\partial E}{\partial N}\right|_{N+\delta} = \lim_{\delta\to 0} \left.\frac{\delta E[n]}{\delta n(\boldsymbol{r})}\right|_{N+\delta} \tag{4.4}$$

$$-I(N) = E(N) - E(N-1) = \lim_{\delta\to 0} \left.\frac{\partial E}{\partial N}\right|_{N-\delta} = \lim_{\delta\to 0} \left.\frac{\delta E[n]}{\delta n(\boldsymbol{r})}\right|_{N-\delta}. \tag{4.5}$$

From the definition of the fundamental gap Eq. (4.2) and using that only the non-interacting kinetic energy $T_\mathrm{s}[n]$ and the xc energy are discontinuous it follows that

$$E_\mathrm{gap} = \lim_{\delta\to 0} \left[\left[\frac{\delta T_\mathrm{s}[n]}{\delta n(\boldsymbol{r})} + \frac{\delta E_\mathrm{xc}[n]}{\delta n(\boldsymbol{r})} \right]_{N+\delta} - \left[\frac{\delta T_\mathrm{s}[n]}{\delta n(\boldsymbol{r})} + \frac{\delta E_\mathrm{xc}[n]}{\delta n(\boldsymbol{r})} \right]_{N-\delta} \right]. \tag{4.6}$$

Similarly, one obtains for the KS-gap

$$E^\mathrm{KS} = \lim_{\delta\to 0} \left[\left.\frac{\delta T_\mathrm{s}[n]}{\delta n(\boldsymbol{r})}\right|_{N+\delta} - \left.\frac{\delta T_\mathrm{s}[n]}{\delta n(\boldsymbol{r})}\right|_{N-\delta} \right]. \tag{4.7}$$

Hence,

$$\begin{aligned} E_\mathrm{gap} &= \varepsilon_\mathrm{HOMO}(N) - \varepsilon_\mathrm{LUMO}(N) + \lim_{\delta\to 0} \left[v_\mathrm{xc}(\boldsymbol{r})|_{N+\delta} - v_\mathrm{xc}(\boldsymbol{r})|_{N-\delta} \right] \\ &= E^\mathrm{KS} + \Delta_\mathrm{xc}. \end{aligned} \tag{4.8}$$

Eq. (4.8) has important implications. As the exact Δ_xc can only be evaluated from two different ground state calculations of the N and the $N+1$ electron system[4], the KS gap E^KS will differ from the fundamental gap even if the exact xc functional is employed. This feature of KS DFT is particularly severe for systems in which E^KS is very small or even zero, so that $E_\mathrm{gap} \approx \Delta_\mathrm{xc}$ as it is the case for Mott insulators.

The second consequence is directly related to the approximate nature of xc functionals. It has been shown that none of the xc functionals employed today exhibits the exact straight line behavior of the total energy with respect to the fractional particle number for a wide variety of systems. Even more strikingly, the failure of existing xc functionals to correctly describe strongly correlated systems has been illustrated in Ref. [165] by pointing out that these functionals do not correctly describe the dissociation behavior of the seemingly simplest systems of the chemical universe, H_2^+ and H_2. In stretched H_2^+, functionals that do not conform to the straight line condition of Eq. (4.1) energetically favor unphysical situations in which a fraction of the charge is localized at each of the nuclei as pointed out before. The tendency of many approximate functionals to delocalize charge is relevant to strongly correlated systems in which localized electrons play a significant role in determining the electronic and magnetic properties.

In stretched H_2 the already mentioned static correlation plays a decisive role. The true ground state of H_2 should be a singlet with equal spin up and spin down density at all distances. From a wavefunction perspective, there are two wavefunctions that are

[4]Recently, attempts have been made to approximately evaluate Δ_xc from a single KS calculation [167].

orthogonal and degenerate in energy, that describe the electronic structure of H_2: One with a spin-up electron at hydrogen atom 1 and a spin-down electron at hydrogen atom 2 and one with spin-up electron at atom 2 and a spin-down electron at atom 1. Furthermore, every linear combination of these two wavefunctions has to be degenerate in energy too, such as a solution with half a spin-up and half a spin-down electron at each atom. Most existing xc functionals, however, lift this degeneracy and massively overestimate the energy of the "fractional" hydrogen atom. This error can produce qualitatively wrong density distributions just as violations of the straight line condition. These considerations give rise to a so-called *constancy condition* for fractional spins, similar to the straight line condition for fractional particle numbers and it has been argued that only xc functionals fulfilling both the straight line condition *and* the constancy condition for fractional spins might be able to describe all sorts of strongly correlated systems correctly [168].

4.3 A DFT-study of the magnetic-to-nonmagnetic transition in Mn-doped Si-clusters

The experimental study of Si cluster singly doped with a Mn impurity was carried out at the synchroton radiation facility BESSY II. Readers interested in the experimental details are referred to Refs [170] and [13]. The results discussed in this section arose from a collaboration with experiment. The following paragraphs, that intend to give a short overview about the experimental findings, contain results that will also be published shortly in Ref. [171].

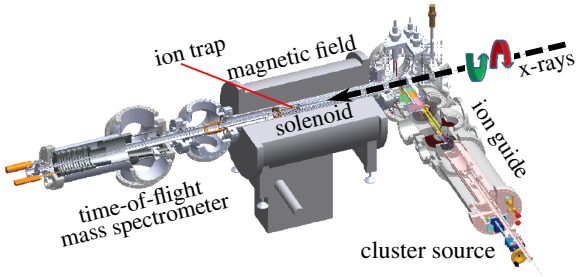

Figure 4.3: Sketch of the experimental setup for XMCD and XAS on free, size-selected $MnSi_n^+$ clusters [169].

Fig. 4.3 illustrates the experimental setup. Mn-doped Si clusters are produced by co-sputtering of a Mn and a Si target. An ion guide leads the clusters into a mass filter, which allows to accumulate clusters of chosen size inside an ion trap, where they are thermalized to 10-20 K. There, x-ray absorption (XAS) and x-ray magnetic circular dichroism (XMCD) spectroscopy probe local $2p \rightarrow 3d$ transitions at the Mn dopant. Upon x-ray absorption the clusters fragment into Mn^+ and Si_2^+ photoions, which are then detected by a reflectron time-of-flight mass spectrometer. Photoion yield spectra are recorded as a function of the incident photon energy yielding a measure for the x-ray absorption cross section. For XMCD spectroscopy additionally a 5 T magnetic field is produced by a superconducting solenoid in order to align the magnetic moments of $MnSi_n^+$. Photoion yield spectra are then obtained for parallel and antiparallel alignment of magnetic field and photon helicity. The resulting XMCD spectrum represents the difference of the photoion yield spectra for parallel and antiparallel alignment of magnetic

field and photon helicity and in principal allows to extract information about spin and orbital magnetic moments of the transition metal dopant using the so called XMCD sum rules [172, 173]. For Mn these sum rules cannot be applied, because the L_2 and the L_3 edges (see Fig. 4.4) are not well separated in energy.

Additionally, the setup allows to extract structural information about $MnSi_n^+$. As Mn and Si have very different reactivities towards oxygen, the depletion of the respective clusters from the cluster beam upon reaction with O_2 can serve as a measure for a change from exohedral to endohedral doping. This is monitored by introducing $\approx 10^{-3}$ mbar partial pressure of O_2 reactant gas into the ion guide. Exohedrally doped clusters react strongly with O_2 and are consequently removed from the cluster beam, while endohedrally doped ones are inert towards O_2, since Mn is surrounded by the less reactive Si atoms in these cases.

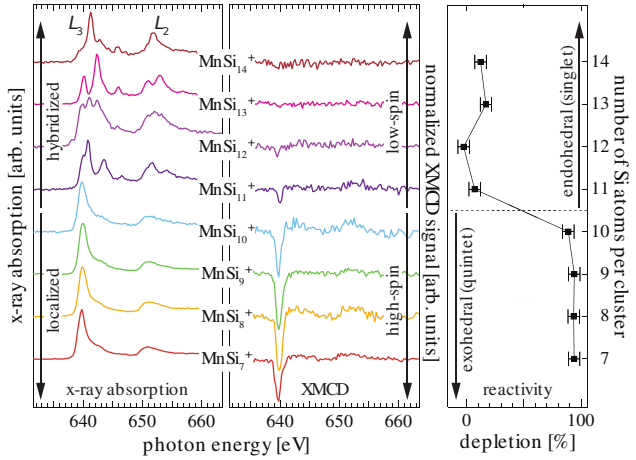

Figure 4.4: Mn $2p$ x-ray absorption (left) and XMCD (center) spectra of $MnSi_n^+ (n = 7-14)$ clusters, indicating quenched magnetic moments for $n \geq 11$; depletion of singly doped clusters in the presence of O_2 as a measure of the exohedral-to-endohedral transition (right).

In Fig. 4.4 the XAS (left panel) and XMCD (center) spectra of $MnSi_n^+$ $(n = 7-14)$ are shown together with the depletion upon reaction with O_2 as a function of cluster size (right). Both the spectra and the depletion study clearly show two size regimes. The depletion of the clusters drops from 89-94 % for $n = 7-10$ to 0-15 % for $n \geq 11$, pointing to a transition from exohedral to endohedral doping from 10 to 11 Si atoms. Likewise, the electronic structure changes considerably between exohedral and endohedral size regime. The very similar absorption spectra of clusters with $n = 7-10$ indicate a similar electronic structure of the Mn dopant, while it is more complex and varies strongly for the endohedrally doped clusters. The XMCD spectra show this transition in electronic structure even more strikingly: the strong XMCD signal of the exohedrally doped clusters, that corresponds to a large magnetic moment of the Mn dopant, is completely quenched upon encapsulation of Mn in the cluster.

Knowledge of the ground state structure of $MnSi_n^+ (n = 7-14)$ is a prerequisite for an in-depth understanding of the magnetic-to-nonmagnetic transition observed in the experiment. To this end, a global geometry optimization was carried out using the simulated annealing and modified big-bang approach introduced in Sec. 2.5. In both cases SPV basis sets were employed. The spin degree of freedom was not held fixed during the simulations. No symmetry constraints were imposed on the structures. All calculations were performed within the TURBOMOLE program suite using the Perdew-Burke-Ernzerhof one parameter hybrid PBE0 [39] in a GKS framework [45] to partly cancel the SIE already at the stage of geometry optimization.

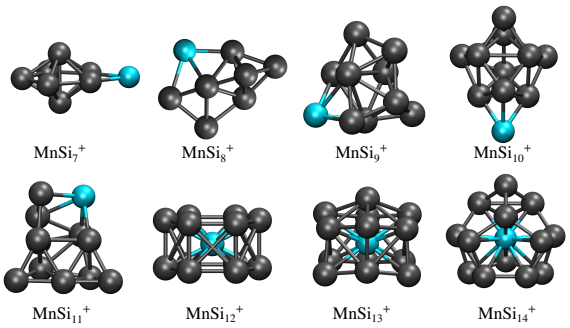

Figure 4.5: Energetically most favorable structures for $MnSi_n^+ (n = 7-14)$ as predicted by PBE0. Contrary to experiment $MnSi_{11}^+$ is exohedrally doped.

For the simulated annealing simulations different starting structures were heated to temperatures between 3500 and 4500 K and propagated at this temperature for 3 ps. Subsequently, the temperature of the system was reduced by a factor of 0.9 every 0.2 ps until it fell below 300 K. At this point the structure usually was trapped in a stiff local minimum. It is therefore of great importance to start simulations from a large number of different geometries to scan as much of the potential energy surface as possible. The lowest energy isomers from these simulations were then locally relaxed using a quasi-Newton method and larger TZVPP basis sets until the total energy changed by less than 10^{-8} Hartree and the forces acting upon the ionic cores were smaller than 0.001 a.u.. The modified big bang approach consisted of randomly generating different sets of starting coordinates with bond lengths compressed by about 10% of the equilibrium bond length and propagating these coordinates at a fixed temperature of 300 K for a short time span of 1.5 ps. Again, lowest energy geometries were locally relaxed as described before.

The energetically lowest lying structures that PBE0 predicts are shown in Fig. 4.5. Consistent with experiment clusters with $n = 7-10$ are exohedrally and clusters with $n = 12-14$ are endohedrally doped. Similarly, in perfect agreement with the XMCD spectra of Fig. 4.4 clusters with $n = 7-10$ exhibit a large magnetic moment of $4\,\mu_B$, while the magnetic moment of those with $n = 12-14$ is completely quenched. $MnSi_{11}^+$ is, contrary to the experimentally predicted exohedral-to-endohedral transition, exohedrally doped. Furthermore, the calculated structure carries a magnetic moment of $2\,\mu_B$ in contradiction to the vanishing XMCD signal of $MnSi_{11}^+$ in Fig. 4.4. The energetically lowest lying endohedral structure, although 1.1 eV higher in energy than the PBE0 ground state, (shown in Fig.4.6) would however agree with experiment.

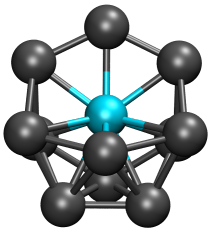

Figure 4.6: Structure of the energetically lowest lying endohedrally doped $MnSi_{11}^+$ as predicted by the PBE0 xc functional.

As the experimentally observed structures are expected to be the ground state structures, a closer look at the theoretical results reveals that the failure of PBE0 for $MnSi_{11}^+$ can indeed be explained in terms of the effect of self-interaction on the eigenvalue spectrum of both isomers. To clarify the situation we calculated the orbital-SIE, Eq. (2.14), as introduced in Sec. 2.2. To determine $e_{i\sigma}$ a local developers version of the program package PARSEC [59] was used to calculate the electronic structure of $MnSi_n^+ (n = 7-14)$. We employed Troullier-Martins pseudopotentials in Kleinman-Bylander form constructed within the PBE GGA [24] with a non-linear core correction as discussed in Sec. 2.4. The pseudopotentials were based on the electronic configuration $4s^{1.75}4p^{0.25}3d^5$ with s/p/d cut-off radii of 1.884/2.573/1.980 a.u. for Mn and $3s^2 3p^2$ with s/p cut-off radii of

2.493/2.390 a.u. for Si. It was tested that the influence of the used pseudopotentials on the eigenvalue spectrum was negligible by comparing them with our all-electron TURBOMOLE calculations. A grid spacing of 0.3 a.u. was used. $e_{i\sigma}$ was evaluated using the PBE GGA xc functional. Following Perdew and Zunger and neglecting the difference between self-interaction corrected and uncorrected orbitals, the self-interaction corrected eigenvalues can be estimated as

$$\varepsilon_{i\sigma} \approx \varepsilon_{i\sigma}^{\text{approx}} - e_{i\sigma}, \tag{4.9}$$

where $\varepsilon_{i\sigma}^{\text{approx}}$ results from a self-consistent calculation using $v_{\text{xc}}^{\text{approx}}$, which is PBE in our case [21]. We can now compare these approximately self-interaction corrected eigenvalues with those that PBE0 yields. The smaller the difference $\Delta\varepsilon_{i\sigma} = \varepsilon_{i\sigma} - \varepsilon_{i\sigma}^{PBE0}$, the more reliable the PBE0 eigenvalues $\varepsilon_{i\sigma}^{\text{PBE0}}$ are.

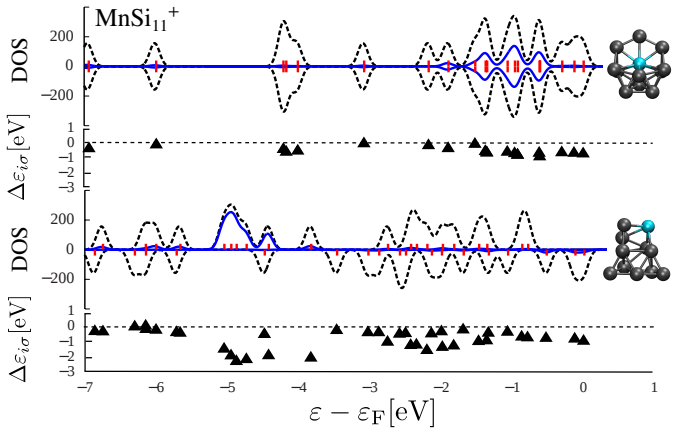

Figure 4.7: Eigenvalue spectrum (bars), total DOS (dotted line), and Mn-projected local DOS (solid line) of endohedral $MnSi_{11}^+$ (top) and the exohedral PBE0 ground state (bottom). $\Delta\varepsilon_i$ is a measure for how much the PBE0 eigenvalues are affected by the SIE.

Fig. 4.7 shows the occupied eigenvalue spectrum interpreted as a DOS and the respective $\Delta\varepsilon_i$ for both $MnSi_{11}^+$ isomers, the endohedrally doped at the top and the exohedrally doped PBE0 ground state at the bottom. While for the endohedrally doped isomer $\Delta\varepsilon_i \approx 0$ for all upper orbitals, the situation is considerably different for the exohedrally doped isomer. Here, the PBE0 eigenvalues are strongly affected by the SIE. This is not only true for the orbitals 4-5 eV below the Fermi level, that can be associated with the Mn dopant[5], but also for higher lying states that participate in bonding. All in all, Fig. 4.7 illustrates that the energetic ordering of $MnSi_{11}^+$ isomers as predicted by PBE0 is unreliable.

In a second step we used a completely different approach to further elucidate the situation. Using the RSH xc functional ωPBE [43] (see Sec. 2.2) as implemented in the QChem program package [174], we checked the energetic ordering of the exohedral and the endohedral $MnSi_{11}^+$ isomers as a function of the range-separation parameter ω. For values of $\omega = 0.2 - 0.4$ a.u. the ωPBE functional predicts the energetic ordering that is in agreement with experiment. This finding highlights the delicate balance of exchange and correlation effects that determines the energetic ordering in $MnSi_{11}^+$.

I will explain in the following, why the SIE, although also plaguing the other exohedral systems, only becomes decisive for the energetic ordering in case of $MnSi_{11}^+$. To this end

[5]This can be done by projecting the KS eigenvalues onto atomic orbitals via a Mulliken population analysis as explained in Sec.3.4.1.

Fig. 4.8 shows the total DOS, the DOS projected onto the Mn-d-orbitals and $\Delta\varepsilon_i$ for $MnSi_7^+$ (top) and $MnSi_{14}^+$ (bottom). These two systems are exemplary for the exohedral and the endohedral size regime, respectively. Additionally, isosurface plots of the orbitals with the largest Mn-3d character and of the HOMO are shown.

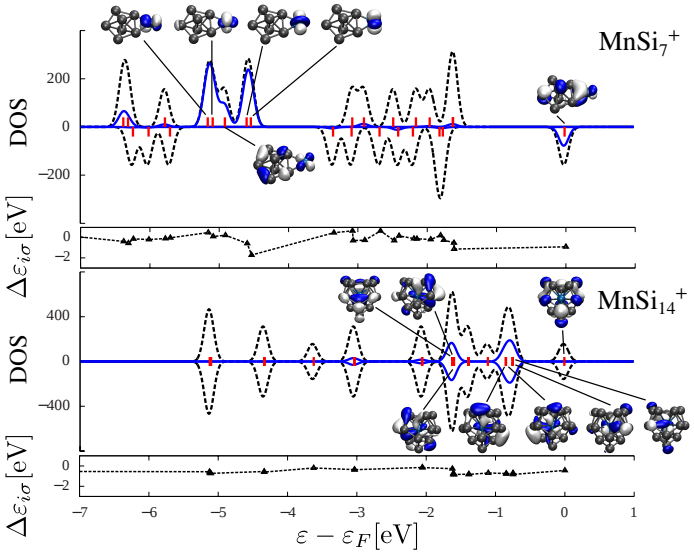

Figure 4.8: Eigenvalue spectrum (bars), total (dotted line), and local Mn 3d-projected (solid line) DOS with isosurface plots (at $\pm$ 0.04 a.u.) of the Mn 3d orbitals and the highest occupied orbital for $MnSi_7^+$ and $MnSi_{14}^+$. Positive (negative) values represent the spin-up (spin-down) channel. The d-like orbitals are localized on the Mn atom in $MnSi_7^+$, whereas they are delocalized in $MnSi_{14}^+$. Also shown is $\Delta\varepsilon_{i\sigma}$, the effect of the SIE on the PBE0 eigenvalues.

Fig. 4.8 illustrates several points. First, for the endohedral size regime, as represented by $MnSi_{14}^+$, PBE0 faithfully predicts the electronic structure, while in the exohedral size regime this is not the case for all relevant states. However, the eigenvalues most severely affected by the SIE (4-5 eV below the Fermi level) are energetically well separated from the Si-states. It is to be expected that the shift of these orbitals in a fully self-interaction corrected calculation would hardly increase the hybridization between the Mn- and the Si-states and therefore the electronic and magnetic properties of these clusters are expected to be only slightly affected. Furthermore, the relative shift between delocalized and localized orbitals that results from the SIE is less critical when structures with localized and delocalized orbitals are energetically well separated [52]. Here, this is the case for all structures except $MnSi_{11}^+$. The latter is the only cluster for which the global geometry optimization resulted in both exohedral and endohedral isomers close in energy. For $MnSi_n^+$ ($n = 7 - 10$) exohedral isomers are consistently lower in energy than endohedral ones.

We checked, however, that the energetic ordering of exohedrally and endohedrally doped isomers remains the same for cluster sizes at the structural transition, i.e., for $MnSi_{10}^+$ and for $MnSi_{12}^+$. To this end we calculated the total energy of the ground state geometry as predicted by PBE0 and the energetically lowest lying endohedral (exohedral) isomer for $MnSi_{10}^+$ ($MnSi_{12}^+$) using ωPBE as before with a range separation parameter of ω=0.2 a.u. as this ω leads to the correct energetic ordering for $MnSi_{11}^+$. Tab. 4.1 shows the energetic difference between exohedrally and endohedrally doped isomers calculated with PBE0 and ωPBE energies for $MnSi_n^+$ (n=10-12) and independently supports the view that the SIE only affects $MnSi_{11}^+$ in such a way as to change the energetic ordering of exohedrally and endohedrally doped isomers. For $MnSi_{10}^+$ and $MnSi_{12}^+$ the energetic ordering as well as the

Table 4.1: Total energies differences of $MnSi_n^+$ (n=10-12) exohedral and endohedral isomers $\Delta E = E^{exo} - E^{endo}$ calculated using PBE0 and ωPBE with a range separation parameter of $\omega = 0.2$ a.u. Positive numbers mean that the endohedral isomer is energetically more favorable.

system	$\Delta E^{\omega PBE}$ in eV	ΔE^{PBE0} in eV
$MnSi_{10}^+$	-0.67	-1.09
$MnSi_{11}^+$	1.67	-1.13
$MnSi_{12}^+$	2.05	1.05

relative energy difference between the exohedral and the endohedral isomer roughly stay the same for PBE0 and ωPBE. Consequently, only $MnSi_{11}^+$ needs special consideration and the endohedral structure shown in Fig. 4.6 can in agreement with experiment considered to be the ground state structure of $MnSi_{11}^+$.

The second point that Fig. 4.8 emphasizes is that the change in local electronic structure of the Mn dopant that was observed in the x-ray absorption spectra (Fig. 4.4) is reflected in the occupied eigenvalue spectrum and also by the shape of the KS orbitals.

For $MnSi_7^+$, the occupied states of Mn $3d$ character are mostly isolated at $\approx 4-5$ eV below the Fermi level and are tightly localized at the Mn dopant, i.e., they largely preserve a (perturbed) atomic character and only weakly interact with Si states, as can be seen from the DOS and the isosurface plots. Note also the similarity between the eigenvalue spectrum of atomic Mn^+ with $4\,\mu_B$ as shown in Fig. 4.9 with the Mn-$3d$-PDOS of $MnSi_7^+$. Because of this weak interaction, the localized orbitals of Mn $3d$ character are qualitatively very similar for all exohedral $MnSi_n^+$ clusters and lead to the nearly identical x-ray absorption spectra in Fig. 4.4.

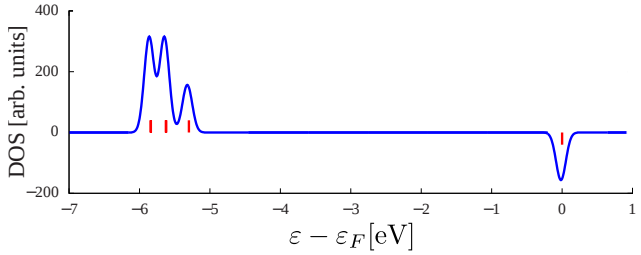

Figure 4.9: Eigenvalue spectrum (bars) and DOS of atomic Mn^+ with 4 unpaired electrons. Note that the ground state of Mn^+ has a spin moment of $6\,\mu_B$.

This notion of, at least partly, atomic Mn $3d$ states is lost in the endohedral size regime, represented by $MnSi_{14}^+$ in Fig. 4.8. Here, orbitals with partial Mn $3d$ character are strongly hybridized with Si states and are shifted to $\approx 0.5-2$ eV below the Fermi level, i.e., they participate strongly in bonding and are delocalized over the Si frame. Consequently, the Mn $3d$ derived PDOS sensitively depends on the structure of the Si cage, which is reflected in the variation of the x-ray absorption spectra of endohedral $MnSi_n^+$ for different n ($n = 11-14$) in Fig. 4.4. The strong *spd* hybridization with the participation of all Mn valence orbitals explains the complete quenching of the magnetic moment from $4\,\mu_B$ in exohedrally to $0\,\mu_B$ in endohedrally doped clusters, which is again in accordance with the experimental XMCD spectra.

Thirdly, Fig. 4.8 is exemplary for the well-known connection between the SIE and the orbital localization [51]. The tightly localized, nearly atomic $3d$-orbitals of $MnSi_7^+$ are more strongly affected by the SIE than the rather delocalized orbitals of $MnSi_{14}^+$, despite the partial Mn-$3d$-character of the latter. For a thorough discussion of orbital localization and self-interaction, the reader is referred to Ref. [51].

The structural change at the exohedral-to-endohedral transition of $MnSi_n^+$ can be quantified by the coordination number N_c of Mn, i.e., the number of Si atoms in the first coordination sphere as exemplified for $MnSi_8^+$ in the inset of Fig. 4.11. In exohedral clusters, Mn adopts a minimal coordination number of $N_c = 2-4$, while in endohedral clusters N_c is maximized to 11−14, i.e., all Si atoms are within the first coordination sphere of Mn.

The average Mn-Si bond length a elucidates why encapsulation of the Mn dopant becomes energetically favorable only for $n \geq 11$: In the ground state structures, the Mn-Si nearest neighbor distance expands from $a = 2.43 - 2.58$ Å in exohedral to $a = 2.53 - 2.67$ Å in endohedral clusters. In contrast, it would be compressed to $a = 2.35$ Å in the energetically most favorable endohedral isomer of $MnSi_{10}^+$ (as illustrated in Fig 4.10). Even though Mn favors high coordination in Si [175], this strain, which becomes even more pronounced in smaller clusters, precludes endohedral ground states for $n \leq 10$.

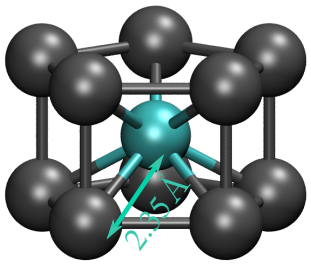

Figure 4.10: Lowest endohedral isomer of $MnSi_{10}^+$. The Mn-Si bond length is compressed to only 2.35 Å in this cluster.

The abrupt change in coordination at the structural transition is interrelated with the quenching of the magnetic moment as illustrated in Fig. 4.11: Here, the calculated magnetic moments of $MnSi_n^+$ are plotted versus the weighted coordination number d_0N_c/a, which takes into account both the number of Si nearest neighbors N_c as well as their average distance a to the Mn atom, normalized to the nearest neighbor distance d_0 in bulk Si. Low-coordinated exohedral clusters with $d_0N_c/a = 1.9 - 3.7$ ($N_c = 2 - 4$) carry a magnetic moment of 4 μ_B, which is quenched to 0 μ_B in high-coordinated species with $d_0N_c/a = 10.2 - 12.3$ ($N_c = 11 - 14$). This relation of magnetic moment and weighted coordination also holds for higher-energy isomers that are included in Fig. 4.11 and mark the transition from magnetic to nonmagnetic impurities around $d_0N_c/a \approx 4$.

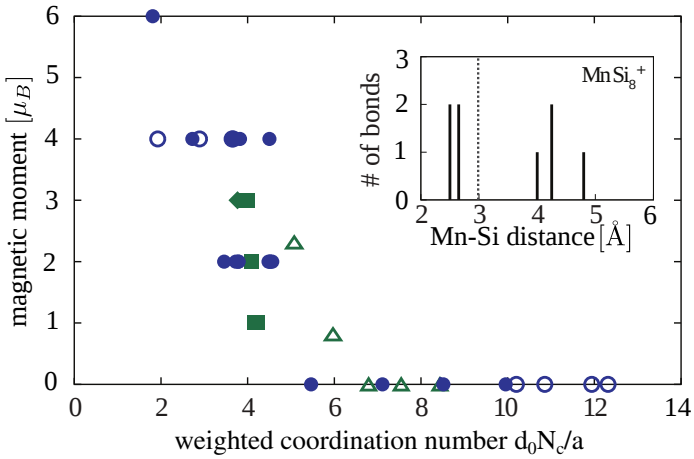

Figure 4.11: Magnetic moment versus weighted coordination d_0N_c/a for ground state (open circles) and higher energy (solid circles) isomers of $MnSi_n^+$ ($n = 7 - 14$), isolated neutral Mn impurities in bulk ([151], solid squares) and amorphous Si ([154], open triangles), and in a Si nanocrystal ([156], solid diamond). Inset: bond length distribution of $MnSi_8^+$ with first coordination sphere (dotted line).

Fig. 4.11 shows that this observation can be generalized to extended systems, i.e., to a neutral Mn impurity at a substitutional site in crystalline Si [151] or in hydrogen-passivated

Si nanocrystals [156]. It also applies to very low concentrations of Mn in amorphous Si, for which a possible relation between magnetic moment and coordination has been pointed out [154]. Yet, although N_c is the leading term, it does not account for the dependence of the local magnetic moment on the nearest-neighbor distance [151] that becomes important around $N_c = 4$ and is included in $d_0 N_c/a$. As can be seen in Fig. 4.11, Mn-doped bulk Si is just at the transition from high-spin to low-spin states and therefore reacts very sensitively to changes in $d_0 N_c/a$. This might explain the large scatter in experimental results on Mn-doped Si and indicates that high-spin states could be stabilized by an appropriate expansion of the lattice parameter, e.g., in ultra-thin films or passivated nanocrystals.

In summary, the magnetic moment of Mn-doped Si has been investigated over a wide range of structural parameters, including extreme coordination numbers from 2 - 14. The study of singly doped, size-selected $MnSi_n^+$ clusters avoids impurity-band formation or interaction between impurities that might be present in experiments on bulk samples, but also in calculations with periodic boundary conditions. Thus the observed quenching of the magnetic moment is not a result of impurity band formation but of the electronic interaction with the Si host. While the SIE strongly affects tightly localized orbitals with Mn-3d character and is thus persistent in exohedrally doped clusters in which the dopant only weakly interacts with the Si host, it only perturbs the energetic ordering of exohedral and endohedral isomers for $MnSi_{11}^+$. Finally, we found an universal correlation of the magnetic moment and the weighted coordination number. Bulk Si doped with Mn lies at the transition from high to low magnetic moments and therefore is particularly sensitive to the nearest neighbor bond lengths of the Mn dopant.

5

Summary and outlook

5.1 Summary

In the present thesis structural and electronic properties of Au-Pt, Au-Pd nanoalloys and Mn-doped Si clusters were studied using non-empirical DFT and MD simulations employing empirical Sutton-Chen potentials. Au-Pt and Au-Pd nanoalloys show a bimetallic effect, i.e., increased activity and selectivity in many different catalytic reactions. This work contributes to the long-standing debate between theory and experiment on the mixing pattern of Au-Pt nanoalloys. We were able to show that a prominent characterization technique based on a combination of XRD and Vegard's law relies on questionable assumptions. $Au_{shell}Pt_{core}$ and homogeneously mixed NP in the experimentally relevant size range of $\approx 4\,\mathrm{nm}$ are indistinguishable in a typical XRD experiment. Furthermore, it was shown that Vegard's law is valid for both types of mixing patterns. Theory consistently predicts core-shell structures as energetically most favorable, but homogeneously mixed Au-Pt nanoalloys are observed in experiment using element-specific characterization techniques. Our findings show that the formation of mixing patterns other than the core-shell one must be linked to effects such as interactions with the support material or the synthesis procedure.

The study of the electronic structure of Au-Pt and Au-Pt nanoalloys showed that the DOS at the Fermi level depends on the Pt and Pd content of the NP, respectively. The DOS at the Fermi level is related to the binding energy between the catalyst and possible adsorbates and it increases with increasing Pt (Pd) content. Additionally, the spatial distribution of the HOMO is connected to the position of the Pt (Pd) atoms. Empirical MD simulations were used to extract the MSD of the atoms in an Au-Pt NP. The MSD is related to the atomic mobility or structural flexibility of the NP. The latter can be beneficial in that it allows the catalyst to structurally adjust to reactants, form element-specific binding sites

and regenerate after a reaction has taken place. It was shown that the MSD increases with increasing Au content. This result could be supported by modeling the NP as surface slabs and studying the diffusion of a single Au or Pt adatom on these surfaces. The activation barrier for adatom diffusion, the simplest type of surface reconstruction, was shown to decrease with increasing Au content.

A combination of the fundamental properties DOS at the Fermi level and atomic mobility might explain why a bimetallic effect is observed for Au-Pt nanoalloys under very varying experimental conditions. A specific Au-Pt ratio could amount to an optimal interaction between catalyst and reactants mediated by an optimal DOS at the Fermi level and an optimal amount of structural flexibility.

In the second part of this thesis the magnetic properties of Mn-doped Si clusters were studied. These systems can be seen as well-defined models for a semiconducting host that interacts with a single magnetic impurity. A global geometry optimization was carried out to identify the ground state structures of $MnSi_n^+$ (n=7-14). In agreement with experiment, it could be shown that a structural transition from exohedral to endohedral doping from $MnSi_{10}^+$ to $MnSi_{11}^+$ is accompanied by complete quenching of the magnetic moment. The size of the magnetic moment is correlated with the coordination number of the Mn dopant weighted with its average nearest neighbor distance. This relation holds also for Mn in amorphous and crystalline Si and suggests ways to stabilize the magnetic moment of a Mn impurity by appropriate lattice expansion.

Systems for which the interaction between strongly localized and delocalized orbitals plays a major role pose serious difficulties to existing approximations of DFT because of the well-known self-interaction problem. By evaluating its orbital-SIE we found that $MnSi_{11}^+$ suffers particularly severely from self-interaction. The one-parameter hybrid xc functional PBE0 which correctly predicted structures and magnetic moments of all other clusters therefore yields a wrong, exohedrally doped ground state structure in this case. By using a RSH functional we saw that the correct energetic ordering of the endohedral and the exohedral isomer is obtained for certain values of the range separation parameter. Together with the orbital-SIE this finding highlights how delicately exchange and correlation effects determine the energetic ordering in $MnSi_{11}^+$.

5.2 An outlook to Ni-Pd nanoalloys

The search for bimetallic catalysts that perform efficiently in large-scale catalysis is frequently guided by the simple principle to find the combination of materials that yields the highest turnover rates and is as cheap as possible. Ni-Pd nanoalloys are in this sense optimal. Additionally, they constitute a system covering a variety of enticing fundamental questions. Firstly, small Ni and Pd clusters are known to exhibit high magnetic moments [11, 140]. The size- and composition-dependent magnetic moment of Ni-Pd nanoalloys is therefore expected to exhibit interesting features. However, Chap. 4.3 showed that the correct description of

Table 5.1: Adsorption energies (in eV) of Pd- and Ni-adatoms on pure and doped Pd- and Ni surfaces for the start (ini) and the end (fin) position of each NEB calculation. The diffusion barrier (in meV) is defined as the energetic difference between the inital position and the saddle point of the minimum energy path.

system	E_{ads} ini	E_{ads} fin	$E_{barrier}$
Pd/Pd	2.70	2.70	70
Pd/Pd+Ni	2.72	2.69	76
Ni/Pd	3.48	3.38	296
Pd/Ni	3.14	3.14	65
Ni/Ni+Pd	3.63	3.69	380
Ni/Ni	3.63	3.63	80

the geometrical and electronic structure even of allegedly simple magnetic transition metal compounds is a huge challenge for theory. DFT studies of small Ni-Pd clusters have up to now only been carried out using standard semilocal xc functionals [176, 177] and global geometry optimizations are rare [178] for these systems. Attempts to construct a reliable pseudopotential for Ni that could be used in conjunction with orbital-dependent functionals have so far proved challenging as well [179].

Secondly, a bimetallic effect in catalysis has recently been observed for Ni-Pd nanoalloys immobilized in so-called metal-organic frameworks [180] as well as in other reactions [78]. A close lying question is therefore whether the general concepts that apply for Au-Pt nanoalloys, are also suited to explain the special properties of Ni-Pd particles. This would again require a faithful description of their electronic structure, at least close to the Fermi level. Furthermore, the atomic mobility or fluxionality of Ni-Pd systems has to be tested. Initial steps into this direction have been taken following a similar line of argument as described in Sec. 3.4.3. Pure and doped Ni- and Pd-surfaces have been modeled by 4x4x4-layer slabs with equilibrium lattice parameters of 3.520 Å for Ni and 3.939 Å for Pd. A surface diffusion step between two equivalent hcp hollow sites as depicted in Fig. 5.1 has been considered.

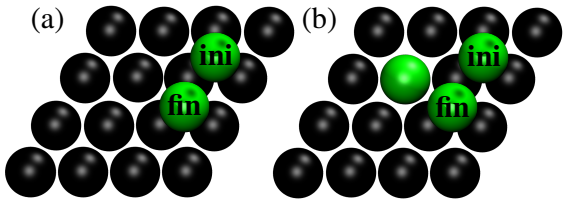

Figure 5.1: Setup for Pd/Ni adatom diffusion on Ni/Pd surface (a) without and (b) with a single Pd/Ni atom in the upper surface layer. The diffusion step takes place from one hcp hollow to another hcp hollow site.

CI-NEB calculations were carried out in order to determine the activation energy of this diffusion step (see Sec. 2.5). Furthermore, the adsorption energies of the adatom at the inital and the final position have been determined using Eq. (3.7). The resulting barriers and adsorption energies are listed in Tab. 5.1. Note that both the adsorption energies and the barriers are considerably smaller than for Au-Pt surfaces (cf. Tab. 3.3). This finding is in line with the recent observation that large Ni-Pd clusters (with diameters of $\approx 4\,\mathrm{nm}$) preferably form solid solutions and that their surface is corrugated due to the large lattice mismatch of Ni and Pd [180]. The strong tendency for segregation of the two components found in Au-Pt NP thus seems not to be present in Ni-Pd NP. Furthermore, no specific trend of the diffusion barriers can be seen in Tab. 5.1. Exceptions to the overall small barriers of between 65 and 80 meV are found for the diffusion of a Ni adatom on Pd with a barrier of almost 300 meV and diffusion of a Ni adatom on a Ni surface doped with a

Pd impurity with 380 meV. The reason might again lie in the large size difference between Ni and Pd. Whether these unusually high diffusion barriers are only an artifact of the inadequate description of the systems' electronic structure by the PBE GGA should be tested by re-calculating the diffusion barriers of Tab. 5.1 using the one-parameter hybrid functional PBE0.

It has been shown that the inherent strain in decahedral Au NP results in a significant shift of their *d*-band center in the direction of the Fermi level. By virtue of the *d*-band model (see Sec. 3.4.1) this finding was used to explain the high catalytic activity of these NP [9]. It could be speculated whether a similar effect also plays a role in Ni-Pd NP as a result of Ni and Pd's considerable lattice mismatch. Similarly, the atomic mobility from a finite cluster perspective, i.e., along the lines of the mobility study presented in Sec. 3.4.3, seems worthwhile to explore.

There is a yet different perspective that makes Ni-Pd clusters a particularly interesting model system. It has been debated that heterogeneous liquid-phase catalysis might not take place at the surface of clusters themselves, but rather on ultra-small cluster fragments or even single atoms that are leached out the parent cluster in solution [181]. This fundamental question of liquid-phase catalysis could be studied using Ni-Pd catalysts, as for very small clusters or single ions high magnetic moments are expected, which could be detected (in liquid phase) using Xenon-NMR (nuclear magnetic resonance). Yet again, a meaningful comparison of this enticing experimental idea with theoretical results, requires a reliable theoretical description of small, magnetic systems. Further studies should therefore focus on the latter, e.g., by using advanced xc functionals such as RSHs or the SIC. The transition metal all-rounder Ni-Pd promises insights into the theoretical description of magnetic transition metal compounds as well as into fundamental questions of heterogeneous liquid-phase catalysis.

Appendices

A

Temperature and support effects

In Sec. 3.4, two fundamental properties of Au-Pt NP were established, a combination of which might result in superior chemical and catalytic features as compared to pure Au and Pt NP: a high DOS at the Fermi level, associated with Pt, and a high atomic mobility or structural fluxionality, associated with Au. However, the experimental conditions under which Au-Pt nanoalloys are applied as catalysts are complex and are expected to have significant impact on the catalysts' properties. NP are usually stabilized by a support that prevents coagulation of individual NP, facilitates the handling of the catalysts and is beneficial to their re-usability. The use of highly active NP allows reactions to take place at mild experimental conditions, i.e., at room temperature and in aqueous solution. Still, interactions between NP and the corresponding support as well as a finite temperature render understanding liquid phase heterogeneous catalysis a complex, dynamical process. In the following two sections, I want to discuss the influence of a specific finite temperature effect, namely thermal expansion, on the DOS at the Fermi level. Additionally, first results on how small Au and Au-Pt NP interact with support molecules, are presented.

A.1 Temperature dependence of the electronic structure

In Sec. 3.3 it was shown that thermal expansion in Au-Pt NP is considerably larger than in the respective bulk systems. The linear thermal expansion coefficient is defined via Eq. (3.3) and 3.4 in Sec. 3.3. While β is $9 \cdot 10^{-6}\,K^{-1}$ for bulk Pt and $14 \cdot 10^{-6}\,K^{-1}$ for bulk Au, it is ca. $19 \cdot 10^{-6} K^{-1}$ up to 600 K for Au-Pt nanoalloys as has been shown in Sec. 3.3. The importance of the DOS at the Fermi level for the catalytic activity of Au-Pt NP was discussed in Sec. 3.4.1. Here, we will evaluate how it changes upon thermal expansion of the cluster.

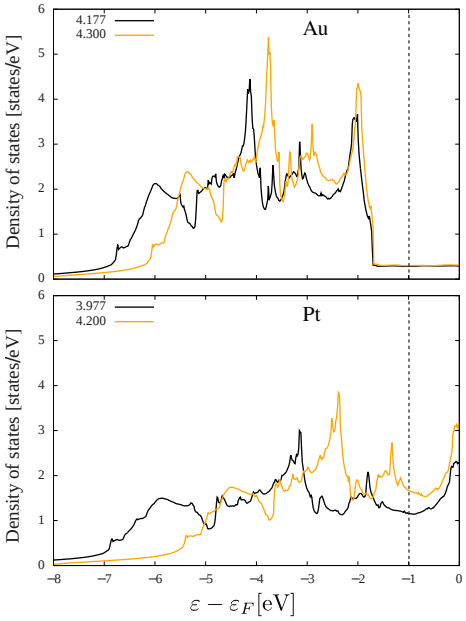

Figure A.1: DOS of bulk Au (top) and Pt (bottom) for the respective equilibrium (black) and a considerably increased lattice parameter (orange). The black dotted line indicates the integration threshold of 1 eV.

To answer this question, consider first the Au and Pt bulk DOS, as depicted in Fig. A.1. The electronic structure was calculated using the PBE GGA as implemented in VASP. The electron-ion interaction was treated within the PAW framework. Further computational details can be found in App. C. The black curves in Fig. A.1 are the DOS of the respective bulk system at its equilibrium lattice parameter, while the orange curves represent the DOS for a considerably expanded lattice. Two main points can immediately be seen in Fig. A.1. Firstly, the DOS at the Fermi level (integration threshold defined as -1 eV as in Sec. 3.4.1) of Au is much smaller than that of Pt. Secondly, upon increasing the lattice parameter, the DOS at the Fermi level hardly changes for Au, while a considerable increase of $\approx 22\%$ can be seen for Pt.

Bulk Au can be considered a good $6s$ free electron metal [2]. Using the dispersion relation of the free electron gas

$$\varepsilon(k) = \frac{\hbar^2 k^2}{2m}, \tag{A.1}$$

in which k is the wave vector and m the electron mass, the DOS per unit volume of a three-dimensional free electron gas can be written as

$$g(\varepsilon) = \frac{m}{\hbar^2 \pi^2}\sqrt{\frac{2m\varepsilon}{\hbar^2}} \propto \sqrt{\varepsilon}. \tag{A.2}$$

The Fermi energy ε_F up to which all energy levels are occupied at zero temperature, corresponds to the Fermi wavenumber via $\varepsilon_F = \hbar^2 k_F^2/2m$. k_F in turn is determined by the electron density by $n = k_F^3/3\pi^2$. Hence, the Fermi energy can be expressed as a function of the electron density

$$\varepsilon_F = \frac{\hbar^2}{2m}(3\pi^2 n)^{\frac{2}{3}}. \tag{A.3}$$

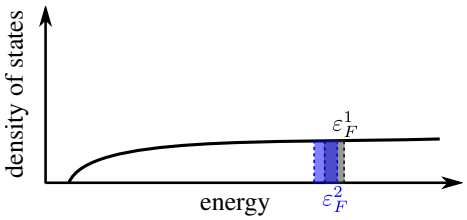

Figure A.2: Upon lattice expansion the Fermi energy of the free electron gas decreases. The integrated DOS at the Fermi level changes only slightly, because of the flatness of $g(\varepsilon)$.

An increasing lattice parameter results in a decrease of the electron density which gives rise to a decrease of the Fermi energy. Fig. A.2 illustrates how thermal expansion of the lattice affects the DOS at the Fermi level of a free electron gas. As $g(\varepsilon)$ is very flat close to the Fermi energy, a shift of the latter only slightly changes the integrated DOS close to the Fermi energy. This explains why it barely changes for bulk Au upon thermal expansion.

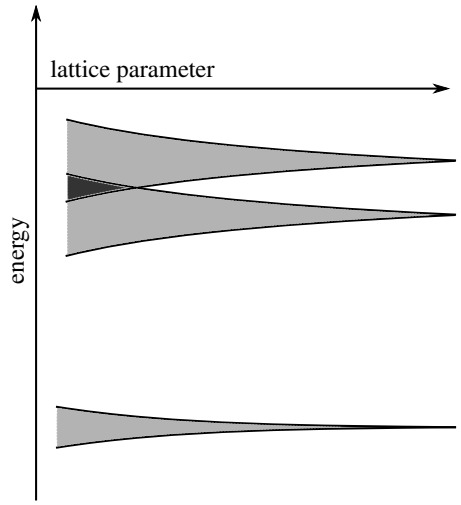

Figure A.3: Schematic of energy levels of a periodic lattice of N atoms as a function of the lattice parameter. The larger the interatomic distance becomes, the narrower become the energy bands. In the limit of infinite separation, the atomic energy levels are completely degenerate.

On the contrary, bulk Pt cannot be described as a free electron gas. To understand the drastic increase of the DOS at the Fermi level of Pt consider the tight binding model of solid state physics in which it is assumed that close to the lattice points the Hamiltonian of the crystal can be represented by the atomic Hamiltonian of atoms localized at the lattice points. The bound eigenstates of the atomic Hamiltonian are assumed to be strongly localized at the atomic sites. Consider a periodic arrangement of M atoms on a lattice with lattice parameter a. If the lattice parameter is sufficiently large, the atomic energy levels are nearly degenerate as illustrated in Fig. A.3. With decreasing interatomic distance, the overlap integrals between single atomic sites become larger and thus the degenerate atomic energy levels are broadened and form energy bands. Thus, one can rationalize the increase of the DOS at the Fermi level for bulk Pt with increasing lattice parameter by noting that a narrowing of the energy bands is followed by an increase of the number of states per energy unit. Additionally, similar to bulk Au, Pt's Fermi level decreases with increasing lattice parameter.

We will now determine, how large the effect of thermal expansion on the DOS at the Fermi level is, by assuming realistic linear thermal expansion coefficients both for the bulk metals, as well as for Au-Pt clusters. For a temperature difference of $\Delta T = 600\,K$ and a linear thermal expansion coefficient of $\beta_{\mathrm{Pt}} = 9 \cdot 10^{-6}\,K^{-1}$, the relative change in the mean interatomic distance $\Delta L/L$ corresponds to an increased lattice parameter of $a^{600\,K} = 3.998\,\text{Å}$. For bulk Au one similarly obtains $a^{600\,K} = 4.212\,\text{Å}$. The corresponding increase of the DOS at the Fermi level is 3% for Pt and negligibly small for Au.

For the clusters, a temperature change of 600 K corresponds to an increase of the mean interatomic distance by $\approx 1\%$. Exemplary, 20-atom, 38-atom and 60-atom clusters each with 0%, 100% and 80–90% Au content were considered. The electronic structure of these clusters with accordingly increased interatomic distances was computed using the PBE GGA and a TZVPP basis set. With the exception of Au_{60}, the relative DOS increase is larger, the higher the Pt content of the system is and ranges between 0.5 and 7%. This is consistent with what one would expect from the above mentioned considerations for the respective bulk systems and also with the d-band model, introduced in Sec. 3.4.1.

The slightly larger increase of the clusters' DOS at the Fermi level as compared to bulk Au and Pt can be attributed to the larger linear thermal expansion coefficient. Fig. A.4 illustrates that the DOS at the Fermi level increases linearly with increasing lattice parameter for bulk Au and Pt. If the increase of the DOS at the Fermi level is now evaluated using the cluster thermal expansion coefficient of $19 \cdot 10^{-6}$ K^{-1} for the bulk, similar values are obtained as for the small clusters. In conclusion, it should be mentioned that even the

Figure A.4: DOS at the Fermi level with increasing lattice parameter for bulk Au (left) and Pt (right). Different integration thresholds are shown, that demonstrate that the Au bulk DOS increases more rapidly, as soon as the 5*d*-derived DOS is taken into account.

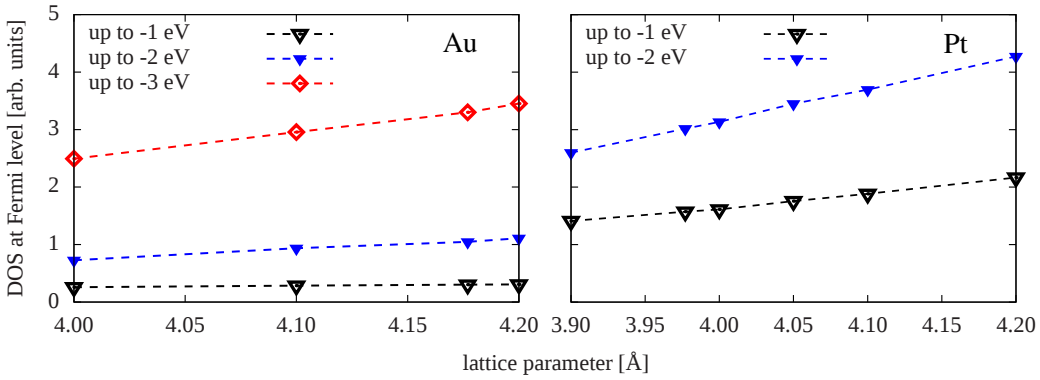

substitution of one Au atom in, e.g., Au_{38} by a Pt atom (upon which the mean interatomic distance even decreases, as shown in Sec. 3.3), leads to a relative increase of the DOS at the Fermi level of nearly 100%, while the position of the Fermi level remains approximately constant. The effect of thermal expansion on the electronic structure of Au-Pt NP is therefore negligibly small as compared to the increase that is observed for alloying Au clusters with Pt atoms.

A.2 Influence of the nanoparticle support

The practical usefulness of catalytic NP is often dictated by how successfully they can be stabilized against coagulation, by their handling and their re-usability. Stabilization by end groups that strongly interact with the NP's surface can severely alter and even limit the catalytic activity. Recently, it has been shown that highly catalytically active Au-Pt nanoalloys with a diameter of ≈ 3-4 nm can be synthesized and immobilized in so-called spherical polyelectrolyte brushes (SPBs) [80]. SPBs consist of a solid polystyrene core onto which long cationic polyelectrolyte chains are densely grafted as sketched in Fig. A.5. The polyelectrolyte is 2-amino-ethyl methacrylate (AEMH) which is positively charged in aqueous solution. Cl^- anions represent the counterions which are mostly confined to the surface layer of the SPB, that is indicated in light gray in Fig. A.5. The Cl^- counterions can be replaced by metal ions like $[AuCl_4]^-$ and $[PtCl_6]^{-2}$. These are then reduced to elemental Au and Pt using $NaBH_2$. During the process of Au-Pt nanoalloy formation the surface layer considerably decreases from about 70 nm to only 20 nm. This can be attributed to the nanoalloys carrying a negative surface charge and therefore strongly interacting with the cationic polyelectrolyte chains. However, this interaction seems to be weak enough not to obstruct the catalytic activity of the Au-Pt nanoalloys [80].

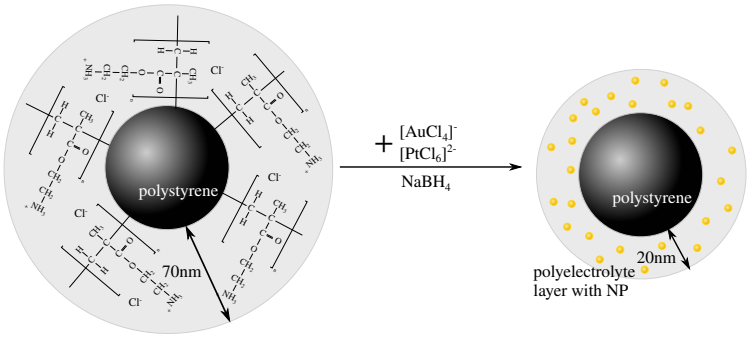

Figure A.5: Au-Pt nanoalloys can be synthesized within the dense polyelectrolyte layer of a spherical polyelectrolyte brush.

In this section, I want to present first results on how the interaction between the NP and the SPB support affects the fundamental structural and electronic properties of the Au-Pt nanoalloys that have been established in the main part of this thesis. As the simplest possible model setup we assume that the metal NP interact with monomeric AEMH units and that the combined system consisting of NP and AEMH units is neutral. The polystyrene core is assumed to be inert and will not be considered here. Furthermore, we disregard the aqueous solution in which the reaction takes place, as we want to concentrate on the effect of the NP-AEMH interaction.

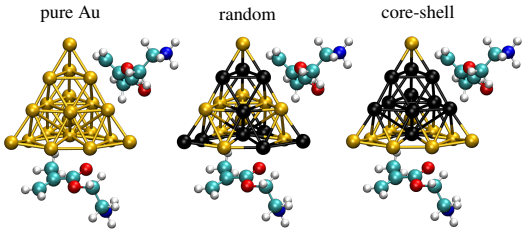

Figure A.6: Two AEMH monomer units are placed close to the surface of an Au_{20}, a randomly mixed $Au_{10}Pt_{10}$ and a core-shell $Au_{10}Pt_{10}$ cluster.

Our first model setup is shown in Fig. A.6. Two AEMH monomer units are placed close to the surface of an Au_{20}, a randomly mixed $Au_{10}Pt_{10}$ and a core-shell like $Au_{10}Pt_{10}$ cluster[1]. The dynamical evolution of these systems is simulated using constant temperature MD simulations via a Nosé-Hoover thermostat of 300 K temperature.

In the original formulation of Nosé, a canonical ensemble is achieved by augmenting the classical Hamiltonian by a time scale variable s, its conjugate momentum p_s and a parameter Q

$$H_{\text{Nosé}} = \sum_{i=1}^{M} \frac{p_i^2}{2m_i s^2} + U(q_1, ..., q_M) + \frac{p_s}{2Q} + (N_f + 1)k_B T \ln s. \tag{A.4}$$

The time scale variable s fluctuates which amounts to a coupling to a heat bath of temperature T. N_f is the number of degrees of freedom. It can be shown that the microcanonical distribution in the augmented set of variables is equivalent to a canonical distribution of the variables $\{q_1, ..., q_M\}$, $\{p'_1, ..., p'_M\}$, where $p'_i = p_i/s$ [182]. As it is inconvenient to work with fluctuating time intervals in practical simulations, one often uses the formulation of Hoover, in which p_s/Q is replaced by a thermodynamic friction

[1]Similar to Sec. 3.2, the label "core-shell" indicates that all Pt atoms are as highly coordinated and all Au atoms are as lowly coordinated as possible.

coefficient η, which can be expressed via a phenomenological relaxation time τ [183]

$$\eta = \frac{p_s}{N_f k_B T \tau^2}, \tag{A.5}$$

which is here chosen four times as large as the simulation time step $\Delta t = 80\,\text{a.u.} \mathrel{\widehat{=}} 1.9\,\text{fs}$.

All systems were propagated for about 16 ps. The electronic structure in each timestep was calculated using the PBE GGA and a SVP basis set augmented as implemented in the TURBOMOLE program package [184]. As van-der-Waals forces are expected to play a role in the interaction between the Au-Pt nanoalloys and the AEMH molecules, the empirical dispersion correction of Grimme was employed [185], which adds a term

$$E_{\text{disp}} = -s_6 \sum_{i=1}^{M-1} \sum_{j=i+1}^{M} \frac{C_6^{ij}}{R_{ij}^6} f_{\text{damp}}(R_{ij}) \tag{A.6}$$

to the total energy of the system. Here, s_6 is a global scaling parameter, which depends on the xc functional employed, C_6^{ij} are empirical dispersion coefficients of atom pair i and j, $R_{ij} = |\boldsymbol{R}_i - \boldsymbol{R}_j|$, f_{damp} is a damping function that avoids singularities at small interatomic distances R_{ij} and M denotes the number of atoms. To differentiate between the effects of temperature and those of the AEMH monomer units, a second set of MD simulations of just the bare systems without AEMH molecules was carried out.

Fig. A.7 provides a visual impression of the first important result of these simulations. It shows an exemplary structure snapshot taken at the end of the simulation. The geometry of all three systems is considerably different from the tetrahedral structure we started with. That this is not only an effect of temperature can be seen by comparison with the structures of the bare Au_{20} and $Au_{10}Pt_{10}$ systems that overall retain their tetrahedral shape. The structure of the bare system is even stable up to temperatures of 600 K, as mentioned in Sec. 3.2 and Ref. [94]. In fact, during the whole simulation strong structural changes take place in the combined NP-AEMH system, while in the bare systems mainly vibrations of the atoms about their equilibrium positions can be seen.

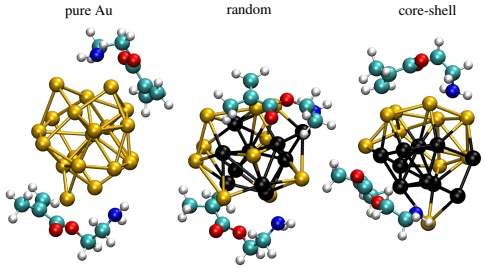

Figure A.7: Structure snapshot taken at the end of each simulation, showing that considerable structural changes have severely distorted the tetrahedral geometry of all three systems.

To quantify these effects we calculated the average nearest neighbor bond length for the NP with and without AEMH monomers for every timestep. Fig. A.8 shows the nearest neighbor bond length of Au_{20} (left), randomly mixed $Au_{10}Pt_{10}$ (middle) and core-shell $Au_{10}Pt_{10}$ (right). The nearest neighbor bond length was defined as the average distance of every atom to its four nearest neighbors. Note that the relaxed core-shell $Au_{10}Pt_{10}$ was taken as the initial geometry for all NP. For Au_{20} all Pt atoms in this NP were then replaced by Au atoms. For the randomly mixed cluster, the Pt atoms were redistributed over the cluster as depicted in Fig. A.6. This means, that one has to compare the nearest

Figure A.8: Average nearest neighbor bond length for every time step of the simulation for the Au_{20} (left), the $Au_{10}Pt_{10}$ randomly mixed (middle) and the $Au_{10}Pt_{10}$ core-shell system with (top) and without (bottom) AEMH monomers. The yellow line, a moving window average, is a guide to the eye.

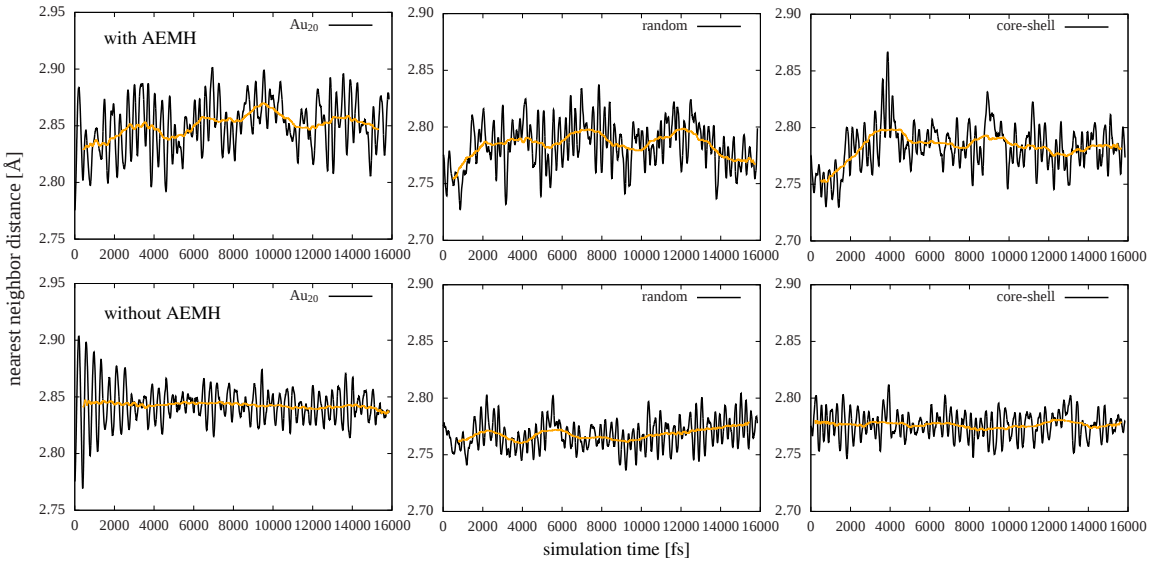

neighbor bond length of the NP-AEMH system with the equilibrium bond length of the bare NP, after all transient processes have decayed. On average, the nearest neighbor bond length increases from 2.84 Å to 2.85 Å in Au_{20}, from 2.78 Å to 2.79 Å in the randomly mixed $Au_{10}Pt_{10}$ cluster and from 2.78 Å to 2.80 Å in the core-shell $Au_{10}Pt_{10}$ cluster. More significant than this slight increase of the average bond length by less than 1% is that the nearest neighbor bond length fluctuates much more strongly in the NP-AEMH systems than in the bare clusters. This is consistent with the larger structural changes in the former.

Additionally, we counted the number of Au-Au, Au-Pt and Pt-Pt bonds of the two $Au_{10}Pt_{10}$ systems in each simulation step. A bond is here defined as every interatomic distance $\leq$ 2.9 Å. For the bare NP these numbers are constant during the whole simulation. For the combined NP-AEMH systems one has to distinguish two time domains, similarly as for the nearest neighbor bond length. The transient time domain from 0 to $\approx$ 6000 fs and the steady state until the end of the simulation. Of course, transient effects are also present for the bare clusters, but they do not affect the number of Au-Au, Au-Pt and Pt-Pt bonds here. Tab. A.1 shows the average steady state number of bonds and the respective standard deviations for $Au_{10}Pt_{10}$ with and without AEMH monomers. Again, we compare the average number of bonds of the combined NP-AEMH system with the number of bonds of the bare NP. For both $Au_{10}Pt_{10}$+AEMH systems the number of Au-Au bonds decreases as compared to their bare counterparts. For the randomly mixed cluster also the number of Au-Pt bonds decreases, while the number of Pt-Pt bonds increases. For the core-shell cluster the number of Au-Pt bonds slightly increases and the number of Pt-Pt bonds decreases. I want to stress that the overall number of Au-Au, Au-Pt and Pt-Pt bonds is too small to allow conclusive

without AEMH	random	core-shell
Au-Au	4 ± 1	8 ± 1
Au-Pt	22 ± 2	13 ± 2
Pt-Pt	12 ± 1	19 ± 1
with AEMH	random	core-shell
Au-Au	2 ± 1	5 ± 2
Au-Pt	20 ± 2	14 ± 2
Pt-Pt	14 ± 1	16 ± 1

Table A.1: Number of Au-Au, Au-Pt and Pt-Pt bonds ≤ 2.9 Å of randomly mixed and core-shell clusters without and with two AEMH monomers. The averages for the bare system is taken over the complete simulation time. For the combined system the average was computed from 6000 to 16 000 fs.

statements here. A first cautious interpretation of these results, however, indicates that the core-shell cluster partly looses its clear Pt-core/Au-shell characteristics, while the randomly mixed cluster undergoes structural changes making it more core-shell like. In other words, in the combined NP-AEMH system the differentiation between randomly mixed and core-shell clusters is not meaningful anymore. Firstly, because on average clusters will exhibit an intermediate mixing pattern in between core-shell and a random distribution of Au and Pt. Secondly, at realistic experimental conditions, i.e., at finite temperature and embedded in a supporting matrix, Au-Pt nanoalloys cannot be described in a static, monostructure fashion anymore [146]. Indeed, in our case at 300 K interaction with the AEMH monomers seems to be the dominant factor that induces structural fluxionality.

Figure A.9: Total energy of randomly mixed and core-shell $Au_{10}Pt_{10}$ in the MD simulation of the combined NP-AEMH system and the bare NP system.

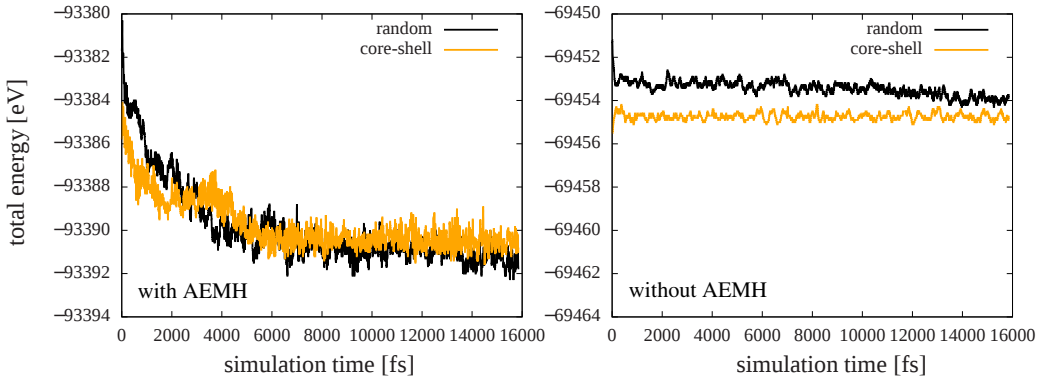

These conclusions are further supported by considering the total energy of the two $Au_{10}Pt_{10}$ systems with and without AEMH support as depicted in Fig. A.9. For the bare system the total energy of the core-shell cluster is consistently lower than that of the randomly mixed particles. This result is not surprising considering that structure and mixing pattern in these simulations remain largely undisturbed. The situation is completely different for the combined NP-AEMH system. Here the core-shell cluster-AEMH system is energetically more favorable at the beginning of the simulation. From $\approx$ 6000 fs on the total energies of the two systems are nearly identical.

Finally, we will take a closer look at the electronic structure of our model system. To

this end, we took 11 structure snapshots of each system, being 194 fs apart from each other ($\hat{=}$ 100 MD steps) starting at 13 545 fs. The electronic structure of these systems was calculated using a TZVPP basis set. No structural relaxation was carried out, as we are interested in the electronic structure of each particular snapshot here. For each structure snapshot we calculated the total DOS and the metal DOS of the combined NP-AEMH system (in the following called metal-PDOS), which is obtained by projecting the total DOS onto the Au and Pt atoms.

Fig. A.10 shows the total DOS of the bare Au_{20} and $Au_{10}Pt_{10}$ systems and the respective metal-PDOS of the combined NP-AEMH systems. The depicted DOS's represent the arithmetic mean of the DOS's of each of the 11 structure snapshots of each system. The metal-PDOS of the combined system is interesting, because we assume that possible reactants in a catalytic process are adsorbed to the NP and react at its surface. Thus, following the considerations of Sec. 3.4.1, the interaction strength between the catalysts and the adsorbates is governed by the metal-PDOS at the Fermi level.

Figure A.10: Total DOS of bare NP (black) and DOS projected onto the metal atoms of the combined NP-AEMH system (yellow) averaged over 11 structure snapshots each, as explained in the text.

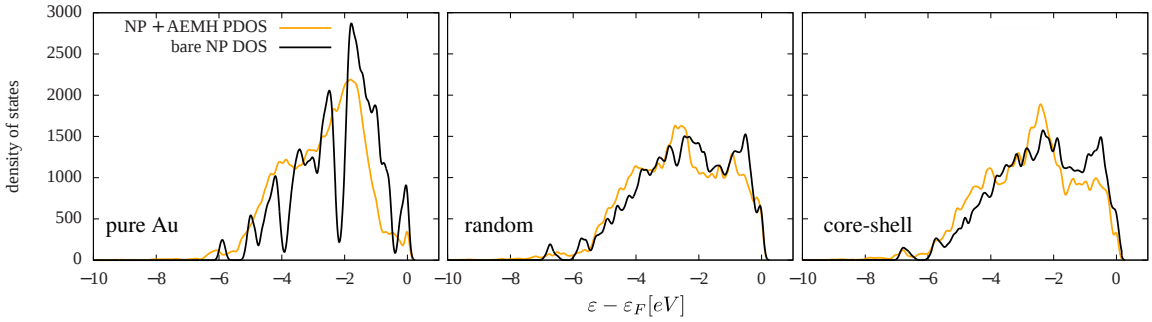

The left panel of Fig. A.10 again demonstrates the special electronic structure of the bare Au_{20} tetrahedron [68]. It's DOS exhibits discrete features and is high close to the Fermi level as compared to other Au clusters (see Sec. 3.4.1). In contrast, the DOS of the bare $Au_{10}Pt_{10}$ clusters, is more continuous and band-like. Note that contrary to the visual impression the DOS at the Fermi level of $Au_{10}Pt_{10}$ is significantly higher than that of Au_{20} in accordance with the results of Sec. 3.4.1. Noticeably, Fig. A.10 shows that the metal-PDOS at the Fermi level is considerably reduced as compared to the bare NP case. This is most pronounced for Au_{20}. Here, the metal-PDOS is more continuous than that of the bare NP. More importantly, the metal-PDOS at the Fermi level is reduced by 60% as compared to the total DOS of the bare NP. The same effect, though less distinct, is seen for $Au_{10}Pt_{10}$. The metal-PDOS at the Fermi level is reduced by 16% for the randomly mixed and by 30% for the core-shell cluster. The large deviations between the DOS reduction of the two $Au_{10}Pt_{10}$ systems can be ascribed to the overall small number of structural snapshots for which the DOS was evaluated. A reduction of the DOS at the Fermi level is expected to lead to weaker interactions with possible adsorbates. Whether it results in an increased or decreased catalytic activity, however, depends on the specific reaction one is interested in. Quite generally the results of this section indicate that the interaction of

our 20-atom Au and Au-Pt NP with AEMH monomer units leads to a marked increase of the fluxionality of the clusters on the one hand. On the other hand the DOS at the Fermi level decreases in the combined NP-AEMH system. In terms of the volcano picture introduced in Sec. 3.4.4, this might correspond to a shift of the volcano peak as compared to the bare NP case. Our findings support the notion that liquid-phase catalysis cannot be modeled using the same concepts that have successfully been applied to gas-phase catalysis on surfaces [131]. Under realistic experimental conditions the description of supported Au-Pt nanoalloys as static entities being governed by their (vacuum and zero-temperature) ground state properties is likely to be flawed.

Yet, even though the results presented in this section allow valuable first insights into the interaction between support molecules and Au-Pt NP further simulations have to be carried out to achieve conclusive results and to judge the significance of the findings presented above. First, simulations have to be done for larger NP, e.g., 40-atom Au-Pt nanoalloys, possibly with a less "special" geometry than the tetrahedron, which has only surface and no volume atoms and is therefore expected to be particularly reactive. Second, it has to be clarified how significant the type of NP support in terms of the reported effects is. Typical supports that could be modeled with reasonable computational effort are, e.g., carbon [87] or silica [79] supports.

B

Optical properties of Au-Pt nanoalloys

The use of finely dispersed Au particles in ruby glass and the colorful stained-glass windows of European's medieval cathedrals shows that their special optical properties have been known for centuries. The first scientific examination of the subject is attributed to Michael Faraday, who studied the interaction of light with colloidal Au particles, as well as thin Au films and leaves as early as 1857 [186]. Today it is well understood that the beautiful color of suspensions of colloidal Au is a result of collective excitations of the conduction electrons that dominate the absorption spectrum, accumulating in a so called *Mie resonance* or *surface plasma resonance*[1]. The position of the Mie resonance depends on the size of the Au colloids, but the optical material functions that describe the linear response of the clusters to electromagnetic waves, are largely size-independent and similar to the bulk values. With these optical material functions one can determine the optical response of (rather large) NP using classical electrodynamics and the so called Mie theory [188].

For NP smaller than $\approx 10\,\mathrm{nm}$, that are still too large to assess them with quantum chemical methods such as time-dependent DFT, the situation is more difficult. The optical response functions become size dependent and can deviate substantially from the bulk. A comprehensive account on optical properties of metal clusters is given in Ref. [187] and pertinent references therein. Here, the focus will be on spherical clusters of 10 nm diameter ($R = 5\,\mathrm{nm}$) interacting with visible light of wavelength λ, i.e., $R \ll \lambda$. The optical response of clusters in this size range can be determined by virtue of Mie theory. For $R \ll \lambda$ (quasi-static case) phase retardation effects and higher multipole orders can be neglected and the absorption cross section in the dipolar limit is

$$\sigma(\omega) = \frac{4\pi\omega}{c\sqrt{\varepsilon_m}}\Im[\alpha(\omega)], \tag{B.1}$$

[1]The term surface plasma resonance refers to the surface polarization being the main restorative force in clusters. This surface polarization is due to charges within the electronic screening length [187].

where $\Im[\alpha(\omega)]$ is the imaginary part of the polarizability of the cluster, which for a homogeneous sphere is

$$\alpha^{\text{homogeneous}}(\omega) = \frac{\varepsilon - \varepsilon_m}{\varepsilon + 2\varepsilon_m} \varepsilon_m R^3. \tag{B.2}$$

In Eq. (B.1) and (B.2), ε is the (complex and ω-dependent) dielectric function of the cluster. We will here assume that ε is similar to its bulk value. The validity of this assumption will be discussed below. The real and imaginary part of the dielectric function $\varepsilon = \varepsilon_1 + i\varepsilon_2$ describe polarization and energy dissipation of matter, respectively, and are related by the famous Kramers-Kronig relations. Fig. B.1 shows ε_1 and ε_2 for bulk Au and Pt as tabulated in Ref. [189] and [190]. Furthermore, Eq.(B.1) and B.2 contain the relative permittivity ε_m of the matrix in which the particle is embedded. For all following calculations $\varepsilon_m = 2.7$ was used, which corresponds to the relative permittivity of polystyrene, one of the major ingredients of the polyelectrolyte matrices used for Au-Pt nanoalloys stabilization in Ref. [80]. Finally, c is the vacuum speed of light.

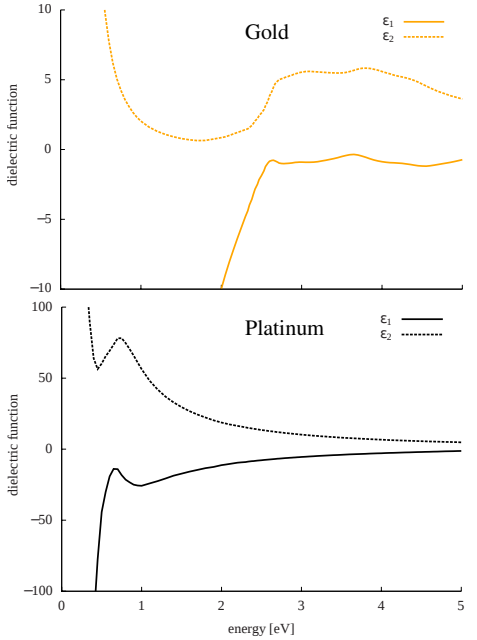

Figure B.1: Real and imaginary part of the dielectric function of bulk Au and Pt, taken from Ref. [189] and [190].

Fig. B.2 depicts the optical absorption spectra of a pure Au and a pure Pt NP of 10 nm diameter. The Mie resonance of the Au NP can clearly be seen at around 2.25 eV. The Pt NP exhibits no Mie resonance in the visible energy range.

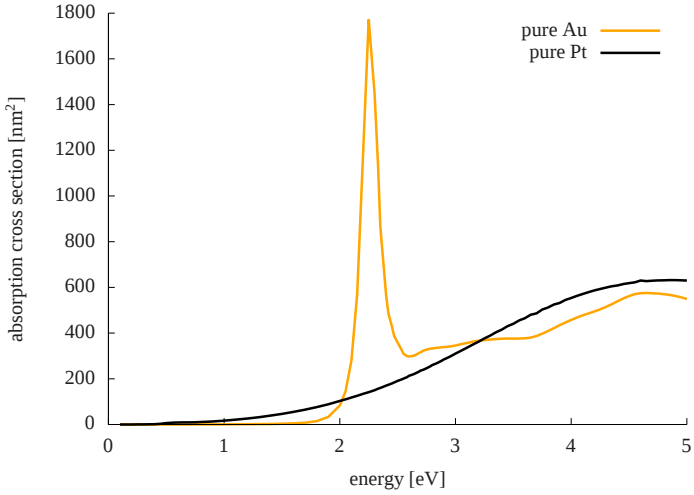

Figure B.2: Optical absorption spectrum calculated using Mie theory in the dipolar limit for spherical metal spheres of 10 nm diameter. Contrary to Pt, Au NP show a pronounced Mie resonance.

At this point the question arises how the optical response of an Au-Pt nanoalloy will evolve as a function of the Au/Pt ratio and how the mixing pattern of Au and Pt influences the optical absorption spectrum of the NP. The optical properties of Au-Pt NP have been studied experimentally [191, 192] and for core-shell clusters also theoretically using Mie-theory as will be explained in the following [192]. Our approach follows a study of Ni-Ag clusters by Gaudry et al. [193].

Mie theory can be extended to the scattering of an electromagnetic wave by two concentric spheres [194]. In the dipolar limit one then obtains for the polarizability

$$\alpha^{\text{core-shell}}(\omega) = \frac{(\varepsilon_{\text{shell}} - \varepsilon_m)(\varepsilon_{\text{core}} + 2\varepsilon_{\text{shell}}) + f_v(\varepsilon_{\text{core}} - \varepsilon_{\text{shell}})(\varepsilon_m + 2\varepsilon_{\text{shell}})}{(\varepsilon_{\text{shell}} + 2\varepsilon_m)(\varepsilon_{\text{core}} + 2\varepsilon_{\text{shell}}) + 2f_v(\varepsilon_{\text{shell}} - \varepsilon_m)(\varepsilon_{\text{core}} - \varepsilon_{\text{shell}})}\varepsilon_m R^3, \quad \text{(B.3)}$$

where $\varepsilon_{\text{core}}$ and $\varepsilon_{\text{shell}}$ are the dielectric functions of the core and the shell, respectively. Here, $f_v = R_c/R$ and R_c is the radius of the core, that one can estimate using the Au-Pt ratio $(1-x)/x$ and the atomic radii of Au and Pt for a $\text{Au}_{\text{shell}}\text{Pt}_{\text{core}}$ cluster

$$V_{\text{core}} = \frac{4}{3}\pi R_c^3 \quad \text{(B.4)}$$

$$V_{\text{shell}} = \frac{4}{3}\pi(R^3 - R_c^3). \quad \text{(B.5)}$$

Assuming the cluster to consist of M_{Au} Au and M_{Pt} Pt atoms

$$M_{\text{Au}} = \frac{V_{\text{shell}}}{V_{\text{Au}}} \quad \text{(B.6)}$$

$$M_{\text{Pt}} = \frac{V_{\text{core}}}{V_{\text{Pt}}}, \quad \text{(B.7)}$$

where $V_{\text{Au,Pt}} = \frac{4}{3}\pi r_{\text{Au,Pt}}^3$ is the volume occupied by a single Au or Pt atom, one obtains

$$\frac{M_{\text{Au}}}{M_{\text{Pt}}} = \frac{1-x}{x} = \frac{r_{\text{Pt}}^3}{r_{\text{Au}}^3}\frac{R^3 - R_c^3}{R_c^3}. \quad \text{(B.8)}$$

With this, the core radius is determined to be approximately

$$R_c = R\sqrt[3]{\frac{x r_{\text{Pt}}^3}{(1-x)r_{\text{Au}}^3 + x r_{\text{Pt}}^3}}. \quad \text{(B.9)}$$

For $\varepsilon_{\text{core}}$ and $\varepsilon_{\text{shell}}$ we take the bulk dielectric functions for Pt and Au. This might not be justified, notably for the shell region and only small percentages of Au. However, for the case of Ni-Ag NP (R=1–2.5 nm) this approximation reproduced the experimentally observed Mie resonance and its blueshift with increasing Ni-content qualitatively well [193].

For a Au-Pt solid solution, the optical absorption can be determined using Eq. (B.1) and (B.2) with an averaged dielectric function [187]

$$\varepsilon = \varepsilon_{\text{Pt}_{x'}\text{Au}_{1-x'}}(\omega) = x'\varepsilon_{\text{Pt}}(\omega) + (1-x')\varepsilon_{\text{Au}}(\omega), \quad \text{(B.10)}$$

in which the volumic proportion x' is defined as

$$x' = \frac{x r_{\mathrm{Pt}}^3}{x r_{\mathrm{Pt}}^3 + (1-x) r_{\mathrm{Au}}^3}. \tag{B.11}$$

The resulting spectra for clusters with varying Pt content x are presented in Fig. B.3. Clearly, it can be seen that the pronounced Mie resonance of the pure Au cluster is considerably damped even for rather low Pt concentrations both for the homogeneously mixed and the core-shell cluster.

Figure B.3: Optical absorption spectrum calculated using (extended) Mie theory in the dipolar limit for spherical metal spheres of 10 nm diameter. The Pt-content of the nanoalloys is denoted by x. Left: Core-shell particle. Right: Solid solution of Au and Pt using an averaged dielectric function $\varepsilon(\omega)$ (see text).

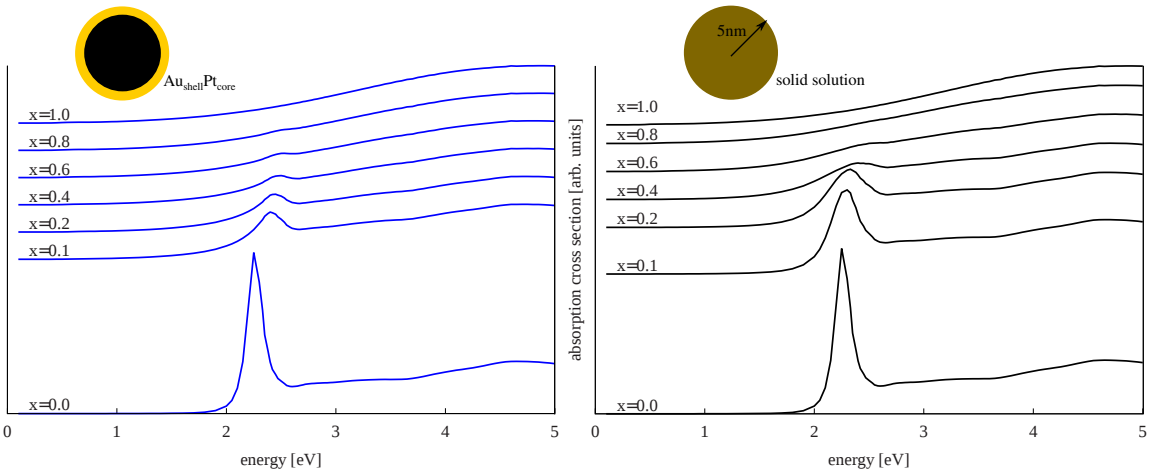

However, the height of the resonance in Fig. B.3 indicates that this damping is much more pronounced for the core-shell cluster. This visual impression is confirmed by integrating the optical absorption over the entire spectral range (up to 5 eV) as shown in Fig. B.4 for NP with varying Pt content.

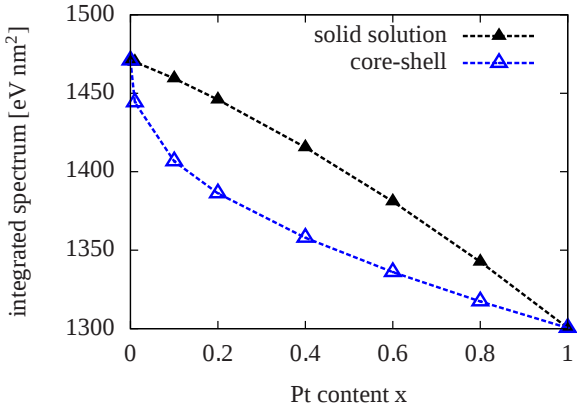

Figure B.4: The optical absorption of a core-shell (hollow triangles) and a homogeneously mixed (filled triangles) NP integrated over the entire spectral range shown in Fig. B.3. Absorption of the core-shell NP is more strongly damped than that of the homogeneously mixed NP. The dashed lines are a guide to the eye.

For a qualitative understanding of this result, consider the polarizabilities Eq. (B.2) and (B.3). Using $R_c^3 = R^3 x'$, one can establish $\Im[\alpha]$ in both cases as a function of the core radius, which for the homogeneously mixed NP is of course only a fictitious quantity corresponding to a certain volumic proportion x'. Fig. B.5 depicts $\Im[\alpha]/R^3\varepsilon_m$ which is proportional to the absorption cross section σ at the Mie resonance (bottom) and for a representative off-resonant case (top).

It can be seen that $\Im[\alpha]/R^3\varepsilon_m$ is smaller for the core-shell cluster for all possible R_c at the resonance. For all other excitation energies, $\Im[\alpha]/R^3\varepsilon_m$ of the core-shell NP can exceed $\Im[\alpha]/R^3\varepsilon_m$ of the homogeneously mixed particle, but only for small volumic proportions of Pt, corresponding to Pt ratios of as little as $\approx 1\%$. Thus, the NP volume can be considered to contribute more strongly to the NP's optical absorption than the surface. In the homogeneously mixed case a fraction of the dielectric function of Au is assumed to be "smeared out" over the complete NP volume, while for a $Au_{shell}Pt_{core}$ NP the full dielectric function of Au is assumed for only a very small volume fraction of the NP: its shell. A stronger damping of the Mie resonance with increasing Pt content in the latter case seems therefore reasonable also from general considerations.

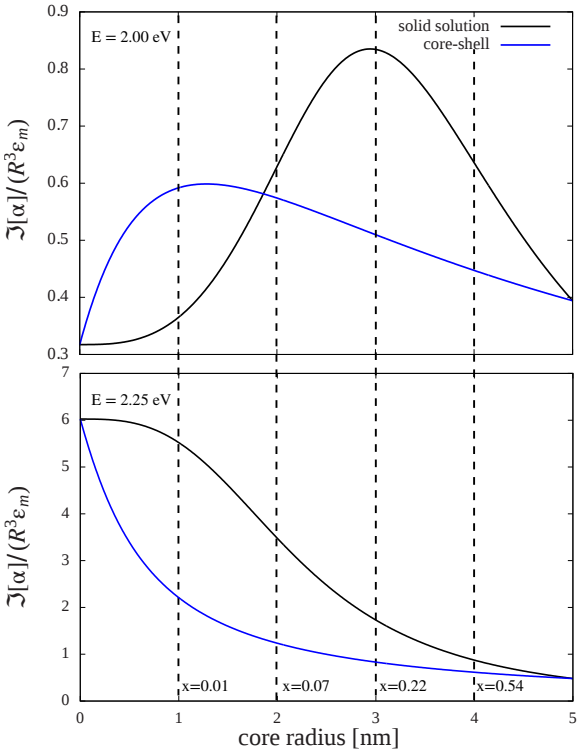

Figure B.5: Imaginary part of the electric dipole polarizablity of a homogeneously mixed and a core-shell NP off-resonance (top) and at the Mie resonance (bottom).

Note, however, that as with decreasing Au content the use of the Au bulk dielectric function becomes increasingly questionable, the results of this chapter should be taken with care. To characterize experimentally observed Au-Pt nanoalloys based on a comparison of experimental and simulated optical absorption spectra, a more advanced treatment of the dielectric functions seems necessary. Additionally, a first principles based approach for clusters consisting of a few tens of atoms could be interesting.

C

Surface slab calculations with VASP

In Sec. 3.2 is was explained that surface slab models can be used to study certain properties of Au-Pt nanoalloys. They are particularly useful for studying properties related to catalytic processes, as reactions take place at the surface of Au-Pt nanoalloys and the high surface/volume ratio of NP contributes to their high catalytic activities in many reactions. In Sec. 3.4.3 a surface slab model was used to determine the activation energy of a simple diffusion step as an indicator for how easily surface rearrangement processes take place in Au-Pt nanoalloys. However, these calculations require some preliminary considerations in order to gain physically meaningful results. Firstly, calculations for the respective bulk material have to be performed to determine the bulk equilibrium lattice parameter and sensible values for the plane wave expansion energy cutoff and the k-points mesh. Secondly, the desired surface has to be constructed and thirdly, the surface slab size (number of surface layers, vacuum height between adjacent unit cells) has to be determined. The following sections give an outline of technical and computational details regarding these issues. A Pt(111) surface slab was chosen as an example.

C.1 Bulk calculations

The prerequisite for a quantitatively reliable slab calculation with VASP is a well-converged bulk calculation. Next to finding an appropriate k-point mesh and cutoff energy for the plane wave expansion, one has to determine the equilibrium lattice parameter, as the slab is supposed to model the bulk far away from the surface. The parameters that primarily determine speed and accuracy of the calculation are the number of k-points used to sample the Brillouin zone and the energy cutoff of the plane wave expansion. The free energy of the bulk should be well-converged for these quantities. In the present thesis the optimal

parameters for ENCUT (energy cutoff) and the k-point mesh for Au and Pt were determined as follows: First, the cutoff energy of the plane wave basis was fixed at a high value (here: 450 eV) and the free energy was converged with respect to the k-point mesh (see left panel of Fig. C.1). Second, the number of k-points was kept fix at a high value (here: 15x15x15. The free energy was converged with respect to the energy-cutoff (see middle panel of Fig. C.1 middle). Third, both the k-points mesh and the energy-cutoff were set to their final values. The lattice parameter is most easily determined by simply computing the free energy as a function of different lattice parameters as depicted in the right panel of Fig. C.1.

Using the PBE GGA this gives an energy-cutoff of 450 eV, a 15x15x15 k-point mesh and a lattice parameter of 3.977 Å for Pt and 4.174 Å for Au as optimal parameters. Note, that electronic structure calculations, e.g., of the DOS or the band structure should be done using an even larger k-point mesh to ensure high accuracy. The DOS of bulk Au and Pt shown in Fig. A.1 were, e.g., calculated using a 21x21x21 k-point mesh.

Figure C.1: Convergence tests for bulk calculations with VASP illustrated for Pt. Left: free energy as a function of k-points (in one dimension). Middle: free energy as a function of energy cutoff of plane wave expansion. Right: free energy as a function of the lattice parameter.

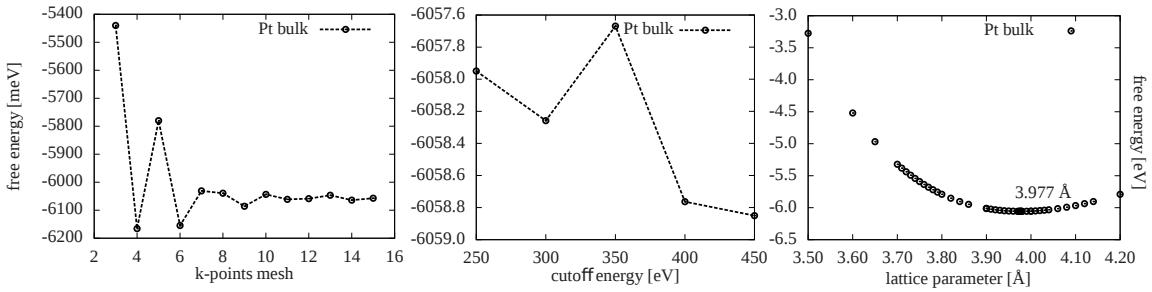

C.2 Slab construction

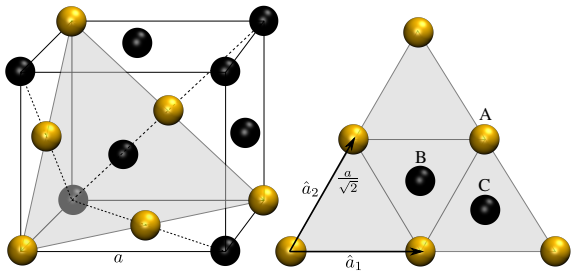

Figure C.2: Left: fcc unit cell with layer A of fcc(111) surface marked in light grey. Atoms in layer A are drawn in yellow, while all other atoms (in layers B and C) are black. Right: Topview on the fcc(111) A layer that shows the surface lattice vectors $\hat{a}_1$ and $\hat{a}_2$. The stacking sequence of the three symmetry inequivalent layers is ABCABC.

In the following, I will outline how to construct a fcc(111) surface slab. The left hand side of Fig. C.2 shows a fcc unit cell with lattice parameter a. There are three symmetry

inequivalent layers as indicated in the right hand side of Fig. C.2. The first fcc(111) surface layer (A) is marked in light grey. Lattice positions lying within this first surface layer are occupied by yellow atoms in this sketch. The surface lattice vectors $\hat{a}_1$ and $\hat{a}_2$ are

$$\hat{a}_1 = \left(\frac{a}{\sqrt{2}}, 0, 0\right) \quad \text{and} \quad \hat{a}_2 = \left(\frac{a}{\sqrt{8}}, \sqrt{\frac{3}{8}}a, 0\right) \tag{C.1}$$

as one can determine from Fig. C.2. The distance between the layers is $a/\sqrt{3}$. That means one can first construct all layers A using $\hat{a}_1$ and $\hat{a}_2$. For layer B these atomic positions have to be moved by

$$\left(0, \frac{2}{3}\sqrt{\frac{3}{8}}a, \frac{a}{\sqrt{3}}\right)$$

and finally for layer C they have to be moved by

$$\left(\frac{1}{\sqrt{8}}a, \frac{1}{3}\sqrt{\frac{3}{8}}a, \frac{2a}{\sqrt{3}}\right). \tag{C.2}$$

A VASP coordinate file (POSCAR) for a 4x4x4 surface slab (showing explicitly only the bottom layer) looks, e.g., like

```
Pt(111) slab                                    #1 comment line
3.977                                           #2 universal scaling factor
 +1.4142135624  +0.0000000000  +0.0000000000    #3
 +0.7071067812  +1.2247448714  +0.0000000000    #4 definition of unit cell
 +0.0000000000  +0.0000000000  +8.4930162690    #5
Pt                                              #6 atomic species
64                                              #7 number of atoms
Cartesian                                       #8 Cartesian or Direct
Selective Dynamics                              #9 flag T or F
 +0.0000000000  +0.0000000000  +0.0000000000 T T T
 +0.3535500000  +0.6123700000  +0.0000000000 T T T
 +0.7071100000  +1.2247400000  +0.0000000000 T T T
 +1.0606600000  +1.8371200000  +0.0000000000 T T T
 +0.7071100000  +0.0000000000  +0.0000000000 T T T
 +1.0606600000  +0.6123700000  +0.0000000000 T T T
 +1.4142100000  +1.2247400000  +0.0000000000 T T T
 +1.7677700000  +1.8371200000  +0.0000000000 T T T
 +1.4142100000  +0.0000000000  +0.0000000000 T T T
 +1.7677700000  +0.6123700000  +0.0000000000 T T T
 +2.1213200000  +1.2247400000  +0.0000000000 T T T
 +2.4748700000  +1.8371200000  +0.0000000000 T T T
 +2.1213200000  +0.0000000000  +0.0000000000 T T T
 +2.4748700000  +0.6123700000  +0.0000000000 F F F
 +2.8284300000  +1.2247400000  +0.0000000000 F F F
 +3.1819800000  +1.8371200000  +0.0000000000 F F F
 ...
```

The selective dynamics flag allows to determine which atomic positions are supposed to be kept fixed during a geometry optimization or a transition state search using the NEB method (see Sec. 2.5). Fixing, e.g., the bottom few layers of the surface slab at the bulk equilibrium lattice constant can reduce computational cost considerably and simultaneously improve the convergence performance. This, however, has to be tested carefully, as will be explained in the following section. Similarly, the number of atoms per surface layer depends on the specifics of the problem one is interested in. In the present work 4x4 atoms per layer were necessary to avoid interactions between adatoms in adjacent unit cells.

C.3 Slab calculations

Prior to any slab calculation one has to determine the number of k-points that yield accurate results at reasonable computational cost. In the direction normal to the surface one k-point is usually sufficient[1]. In the two other directions one can start with the bulk values and then test convergence of the free energy when decreasing the value along these two directions. For the 4x4x4 atoms surface slabs a 5x5x1 k-point mesh was used throughout all calculations.

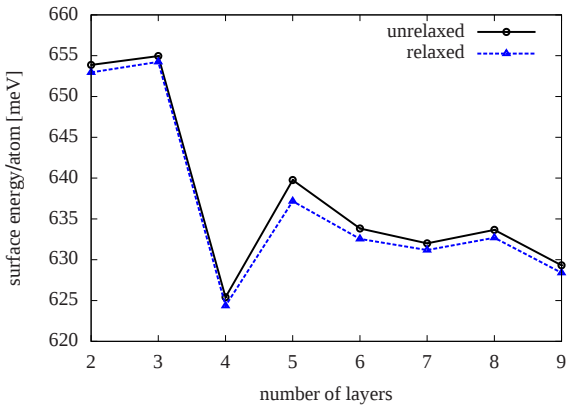

Figure C.3: Surface energy per atom of a 2x2 atoms per layer Pt(111) slab as a function of the number of layers.

One then has to determine how many layers of bulk are necessary to get converged results for the surface energy

$$\sigma = \frac{1}{2}(E_{\text{slab}} - ME_{\text{bulk}}), \qquad \text{(C.3)}$$

where E_{slab} is the free energy of the slab, E_{bulk} is the free energy per atom of the bulk system and M is the number of atoms used for construction of the surface slab. The factor 1/2 arises as a consequence of the surface slab having two surfaces. Fig. C.3 depicts σ per atom as a function of the number of layers (using 4 atoms per layer) of a Pt(111) surface slab. As 16 atoms per layer were used for the final calculations, a minimum number of 4 layers is chosen. Note, that even this seemingly small setup yields unit cells containing 64 atoms which in the case of a pure Pt slab, using the PAW method to describe the electron-ion interaction (see Sec. 2.4), corresponds to a total of 640 electrons. The computational cost can be reduced by fixing the bottom two layers at the equilibrium lattice parameter of the bulk using VASP's selective dynamics flag. It was tested that reaction barriers change only insignificantly as compared to a full relaxation of the slab.

[1] Using more than one k-point in this direction only improves the description of the interaction between adjacent unit cells that has to be minimized anyway by choosing an adequate amount of vacuum space in between neighboring slabs.

Finally, the convergence with respect to the vacuum height in between neighboring slabs has to be tested. Fig. C.4 shows the free energy of a 2x2x7 layer Pt(111) slab as a function of vacuum height. For the final calculations a vacuum height of 20 Å was chosen.

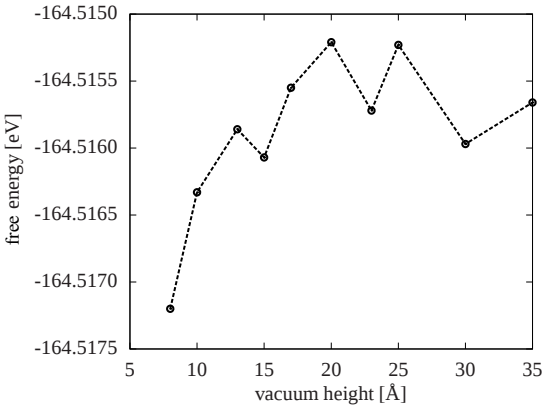

Figure C.4: Free energy of a 2x2x7 Pt(111) surface slab as a function of the vacuum between adjacent unit cells.

The initial and final configuration between which the NEB algorithm is supposed to find a transition state, have to be relaxed prior to setting up the NEB calculation. The initial guess for the elastic band can be a linear interpolation between start and end configuration. If one is interested in the energy of the saddle point it is recommended to use the CI-NEB together with a minimum amount of elastic band images. For the simple diffusion step considered in case of the Au-Pt surfaces one single image was sufficient to determine the reaction barrier. Using three instead of one image did not change the height of the barrier significantly. However, if a truthful map of the MEP is required, more images might be necessary depending on the particulars of the system one is interested in. A typical input file used for the NEB calculations presented in Sec. 3.4 is

```
SYSTEM = Pt/Pt(111)  #insert system name
ENCUT = 450          #plane wave cutoff
ISTART = 0           #start calculation from scratch
ISPIN = 2            #allow spin polarized solution
PREC = accurate      #controls several precision parameters
#relax
NSW = 100            #maximum of 100 ionic steps
IBRION = 2           #conjugate gradient algorithm
EDIFFG = -0.02       #relax tolerance
SPRING = -5          #turns on NEB
IMAGES = 1           #number of images
LCLIMB = .TRUE.      #turn on CI-NEB
IALGO=48             #algorithm for electronic relaxation
LREAL=auto           #projection operators evaluated in real space
LCHARG=.TRUE.        #write electronic density
LWAVE=.TRUE.         #write wavefunctions
                     #these can be turned off if memory is an issue
```

List of abbreviations

AEMH 2-amino-ethyl-methacrylate

Au Gold

(CI)-NEB (Climbing-image)-Nudged Elastic Band

DFT Density Functional Theory

GGA Generalized gradient approximation

(G)KS (Generalized) Kohn-Sham

HOMO Highest occupied (generalized) Kohn-Sham orbital

LDA Local density approximation

LUMO Lowest unoccupied (generalized) Kohn-Sham orbital

MEP Minimum energy path

Mn Manganese

MD Molecular dynamics

Ni Nickel

NP Nanoparticle(s)

OEP Optimized effective potential

PAW Projector augmented waves

PBE xc functional of Perdew, Burke and Ernzerhof

Pd Palladium

Pt Platinum

RSH Range-separated hybrid

SIC Self-interaction correction

SIE Self-interaction error

Si Silicon

SVP Split valence basis set

TZVPP Triple-ζ basis set

VASP Vienna-Ab-initio-Simulation Package

XAS X-ray absorption spectroscopy

xc exchange-correlation

XMCD X-ray magnetic circular dichroism

XRD X-ray diffraction

List of Publications

1. V. Zamudio-Bayer, **L. Leppert**, K. Hirsch, A. Langenberg, J. Rittmann, M. Kossick, R. Richter, A. Terasaki, T. Möller, B. v. Issendorff, S. Kümmel, and J. T. Lau. Coordination-driven magnetic-to-nonmagnetic transition in manganese-doped silicon clusters. Phys. Rev. B, **88**, 115425 (2013).

2. **L. Leppert**, R. Q. Albuquerque, A. S. Foster, and S. Kümmel. The interplay of electronic structure and atomic mobility in nanoalloys of Au and Pt. J. Phys. Chem. C **117**, 17268 (2013).

3. **L. Leppert**, R. Q. Albuquerque, and S. Kümmel. Gold-platinum alloys and Vegard's law on the nanoscale. Phys. Rev. B, **86**, 241403(R) (2012).

4. J. Kaiser, **L. Leppert**, H. Welz, F. Polzer, S. Wunder, N. Wanderka, M. Albrecht, T. Lunkenbein, J. Breu, S. Kümmel, Y. Lu, and M. Ballauff. Catalytic activity of nanoalloys from gold and palladium. Phys. Chem. Chem. Phys. **14**, 6487 (2012).

5. **L. Leppert**, S. Kümmel. The Electronic Structure of Gold-Platinum Nanoparticles: Collecting Clues for Why They Are Special. J. Phys. Chem. C **115**, 6694 (2011).

References

[1] R. Pool, "Clusters: Strange Morsels of Matter", Science **248**, 1186 (1990).

[2] H. Häkkinen, "Atomic and electronic structure of gold clusters: understanding flakes, cages and superatoms from simple concepts.", Chem. Soc. Rev. **37**, 1847 (2008).

[3] J. A. Alonso, "Electronic and atomic structure, and magnetism of transition-metal clusters.", Chem. Rev. **100**, 637 (2000).

[4] M. Haruta, "Size- and support-dependency in the catalysis of gold", Catal. Today **36**, 153 (1997).

[5] M. Haruta, T. Kobayashi, H. Sano, and N. Yamada, "Novel Gold Catalysts for the oxidation of carbon monoxide at a temperature far below 0 °C", Chem. Lett., 405 (1987).

[6] P. Pyykkö, "Theoretical chemistry of gold.", Ang. Chem. (Int. Ed.) **43**, 4412 (2004).

[7] A. Sanchez, S. Abbet, U. Heiz, W.-D. Schneider, H. Häkkinen, R. N. Barnett, and U. Landman, "When gold is not noble: nanoscale gold catalysts", J. Phys. Chem. A **103**, 9573 (1999).

[8] A. A. Herzing, C. J. Kiely, A. F. Carley, P. Landon, and G. J. Hutchings, "Identification of active gold nanoclusters on iron oxide supports for CO oxidation.", Science **321**, 1331 (2008).

[9] M. J. Walsh, K. Yoshida, A. Kuwabara, M. L. Pay, P. L. Gai, and E. D. Boyes, "On the structural origin of the catalytic properties of inherently strained ultrasmall decahedral gold nanoparticles.", Nano Lett. **12**, 2027 (2012).

[10] A. S. K. Hashmi, "Gold-catalyzed organic reactions.", Chem. Rev. **107**, 3180 (2007).

[11] I. M. Billas, A Châtelain, and W. A. de Heer, "Magnetism from the atom to the bulk in iron, cobalt, and nickel clusters.", Science **265**, 1682 (1994).

[12] I. M. L. Billas, A. Châtelain, and W. A. de Heer, "Magnetism of Fe , Co and Ni clusters in molecular beams", J. Magn. Magn. Mater. **168**, 64–84 (1997).

[13] M. Niemeyer, K. Hirsch, V. Zamudio-Bayer, A. Langenberg, M. Vogel, M. Kossick, C. Ebrecht, K. Egashira, A. Terasaki, T. Möller, B. v. Issendorff, and J. Lau, "Spin coupling and orbital angular momentum quenching in free iron clusters", Phys. Rev. Lett. **108**, 057201 (2012).

[14] W. Kohn, "Nobel Lecture: Electronic structure of matter - wave functions and density functionals", Rev. Mod. Phys. **71**, 1253 (1999).

[15] P. Hohenberg and W. Kohn, "Inhomogeneous electron gas", Phys. Rev. **136**, B864 (1964).

[16] W. Kohn and L. J. Sham, "Self-consistent equations including exchange and correlation effects", Phys. Rev. **385**, A1133 (1965).

[17] E. Engel and R. M. Dreizler, *Density Functional Theory - An Advanced Course* (Springer, Berlin, Heidelberg, 2011).

[18] S. Kümmel and L. Kronik, "Orbital-dependent density functionals: Theory and applications", Rev. Mod. Phys. **80**, 3 (2008).

[19] D. M. Ceperley and B. J. Alder, "Ground state of the electron gas by a stochastic method", Phys. Rev. Lett. **45**, 566 (1980).

[20] S. H. Vosko, L. Wilk, and M. Nusair, "Accurate spin-dependent electron liquid correlation energies for local spin density calculations: a critical analysis", Can. J. Phys. **58**, 1200 (1980).

[21] J. P. Perdew and A. Zunger, "Self-interaction correction to density functional approximations for many-electron systems", Phys. Rev. B **23**, 5048 (1981).

[22] J. P. Perdew and Y. Wang, "Accurate and simple analytic representation of the electron-gas correlation energy", Phys. Rev. B **45**, 13244 (1992).

[23] O. Gunnarsson and B. I. Lundqvist, "Exchange and correlation in atoms, molecules, and solids by the spin-density-functional formalism", Phys. Rev. B **13**, 4274 (1976).

[24] J. P. Perdew, K. Burke, and M. Ernzerhof, "Generalized Gradient Approximation made simple.", Phys. Rev. Lett. **77**, 3865 (1996).

[25] A. D. Becke, "Density-functional exchange-energy approximation with correct asymptotic behavior", Phys. Rev A **38**, 3098 (1988).

[26] C. Lee, W. Yang, and R. Parr, "Development of the Colle-Salvetti correlation-energy formula into a functional of the electron density", Phys. Rev. B **37**, 785 (1988).

[27] L. H. Thomas, "The calculation of atomic fields", Proc. Cambridge Philos. Soc. **23**, 542 (1927).

[28] E. Fermi, "Eine statistische Methode zur Bestimmung einiger Eigenschaften des Atoms und ihre Anwendung auf die Theorie des periodischen Systems der Elemente", Z. Phys. **48**, 73 (1928).

[29] J. P. Perdew, "Orbital functional for exchange and correlation: self-interaction correction to the local density approximation", Chem. Phys. Lett. **64**, 127 (1979).

[30] J. B. Krieger, Y. Li, and G. J. Iafrate, "Construction and application of an accurate local spin-polarized Kohn-Sham potential with integer discontinuity: Exchange-only theory", Phys. Rev. A **45**, 101 (1992).

[31] T. Körzdörfer, S. Kümmel, and M. Mundt, "Self-interaction correction and the optimized effective potential.", J. Chem. Phys. **129**, 014110 (2008).

[32] T. Körzdörfer, S. Kümmel, N. Marom, and L. Kronik, "When to trust photoelectron spectra from Kohn-Sham eigenvalues: The case of organic semiconductors", Phys. Rev. B **79**, 201205 (2009).

[33] T. Körzdörfer, S. Kümmel, N. Marom, and L. Kronik, "Erratum: When to trust photoelectron spectra from Kohn-Sham eigenvalues: The case of organic semiconductors", Phys. Rev. B **82**, 129903 (2010).

[34] M. Johansson, A. Lechtken, D. Schooss, M. Kappes, and F. Furche, "2D-3D transition of gold cluster anions resolved", Phys. Rev. A **77**, 053202 (2008).

[35] J. Tao, J. Perdew, V. Staroverov, and G. Scuseria, "Climbing the density functional ladder: nonempirical meta-generalized gradient gpproximation designed for molecules and solids", Phys. Rev. Lett. **91**, 146401 (2003).

[36] A. D. Becke, "A new mixing of Hartree-Fock and local density-functional theories", J. Chem. Phys. **98**, 1372 (1993).

[37] M. Levy, "Electron densities in search of Hamiltonians", Phys. Rev. A **26**, 1200 (1982).

[38] J. P. Perdew, M. Ernzerhof, and K. Burke, "Rationale for mixing exact exchange with density functional approximations", J. Chem. Phys. **105**, 9982 (1996).

[39] C. Adamo and V. Barone, "Toward reliable density functional methods without adjustable parameters: The PBE0 model", J. Chem. Phys. **110**, 6158 (1999).

[40] A. D. Becke, "Density-functional thermochemistry. IV. A new dynamical correlation functional and implications for exact-exchange mixing", J. Chem. Phys. **104**, 1040 (1996).

[41] P. J. Stephens, F. J. Devlin, C. F. Chabalowski, and M. J. Frisch, "Ab Initio Calculation of Vibrational Absorption and Circular Dichroism Spectra Using Density Functional Force Fields", J. Phys. Chem. **98**, 11623 (1994).

[42] M. Rohrdanz and J. Herbert, "Simultaneous benchmarking of ground- and excited-state properties with long-range-corrected density functional theory.", J. Chem. Phys. **129**, 034107 (2008).

[43] T. M. Henderson, B. G. Janesko, and G. E. Scuseria, "Generalized gradient approximation model exchange holes for range-separated hybrids.", J. Chem. Phys. **128**, 194105 (2008).

[44] L. Kronik, T. Stein, S. Refaely-Abramson, and R. Baer, "Excitation Gaps of Finite-Sized Systems from Optimally Tuned Range-Separated Hybrid Functionals", J. Chem. Theory Comp. **8**, 1515 (2012).

[45] A. Seidl, A. Görling, P. Vogl, J. A. Majewski, and M. Levy, "Generalized Kohn-Sham schemes and the band-gap problem.", Phys. Rev. B **53**, 3764 (1996).

[46] A. Görling, "Density-functional theory for excited states", Phys. Rev. A **54**, 3912 (1996).

[47] A. Görling and M. Levy, "Exact Kohn-Sham scheme based on perturbation theory", Phys. Rev. A **50**, 196 (1994).

[48] D. P. Chong, O. V. Gritsenko, and E. J. Baerends, "Interpretation of the Kohn-Sham orbital energies as approximate vertical ionization potentials", J. Chem. Phys. **116**, 1760 (2002).

[49] J. F. Janak, "Proof that $\partial E/\partial n_i = \varepsilon_i$ in density-functional theory", Phys. Rev. B **18**, 7165 (1978).

[50] C.-O. Almbladh and U. von Barth, "Exact results for the charge and spin densities, exchange-correlation potentials, and density-functional eigenvalues", Phys. Rev. B **31**, 3231 (1985).

[51] T. Körzdörfer, "On the relation between orbital-localization and self-interaction errors in the density functional theory treatment of organic semiconductors.", J. Chem. Phys. **134**, 094111 (2011).

[52] T. Körzdörfer and S. Kümmel, "Single-particle and quasiparticle interpretation of Kohn-Sham and generalized Kohn-Sham eigenvalues for hybrid functionals", Phys. Rev. B **82**, 155206 (2010).

[53] E. Fermi, "Displacement by pressure of the high lines of the spectral series", Nuovo Cimento **11**, 157 (1934).

[54] P. Pyykkö, "Relativistic Effects in Structural Chemistry", Chem. Rev. **88**, 563 (1988).

[55] L. Kleinman, "Relativistic norm-conserving pseudopotential", Phys. Rev. B **21**, 2630 (1980).

[56] D. R. Hamann, M. Schlüter, and C. Chiang, "Norm-conserving pseudopotentials", Phys. Rev. Lett. **43**, 1494 (1979).

[57] G. B. Bachelet, D. R. Hamann, and M. Schlüter, "Pseudopotentials that work: From H to Pu", Phys. Rev. B **26**, 4199 (1982).

[58] N. Troullier and J. L. Martins, "Efficient pseudopotentials for plane-wave calculations", Phys. Rev. B **43**, 1993 (1991).

[59] L. Kronik, A. Makmal, M. L. Tiago, M. M. G. Alemany, M. Jain, X. Huang, Y. Saad, and J. R. Chelikowsky, "PARSEC – the pseudopotential algorithm for real-space electronic structure calculations: recent advances and novel applications to nano-structures", Phys. Stat. Sol. B **243**, 1063 (2006).

[60] S. G. Louie, S. Froyen, and M. L. Cohen, "Nonlinear ionic pseudopotentials in spin-density-functional calculations", Phys. Rev. B **26**, 1738 (1982).

[61] E. Engel, A. Höck, R. N. Schmid, R. M. Dreizler, and N. Chetty, "Role of the core-valence interaction for pseudopotential calculations with exact exchange", Phys. Rev. B **64**, 125111 (2001).

[62] Turbomole, V6.0.2 (2009).

[63] D. Andrae, M. Dolg, H. Stoll, and H. Preub, "Energy-adjusted ab initio pseudopotentials for the second and third row transition elements", Theor. Chim. Acta **77**, 123 (1990).

[64] P. E. Blöchl, "Projector augmented wave method", Phys. Rev. B **50**, 17953 (1994).

[65] N. A. W. Holzwarth, G. E. Matthews, R. B. Dunning, a. R. Tackett, and Y. Zeng, "Comparison of the projector augmented-wave, pseudopotential, and linearized augmented-plane-wave formalisms for density-functional calculations of solids", Phys. Rev. B **55**, 2005 (1997).

[66] G. Kresse, "From ultrasoft pseudopotentials to the projector augmented-wave method", Phys. Rev. B **59**, 1758 (1999).

[67] G. Kresse and J. Furthmüller, "Efficient iterative schemes for ab initio total-energy calculations using a plane-wave basis set.", Phys. Rev. B **54**, 11169 (1996).

[68] J. Li, X. Li, H.-J. Zhai, and L.-S. Wang, "Au_{20}: a tetrahedral cluster.", Science **299**, 864 (2003).

[69] S. Kirkpatrick, C. D. Gelatt, and M. P. Vecchi, "Optimization by simulated annealing.", Science **220**, 671 (1983).

[70] V. Černý, "Thermodynamical approach to the traveling salesman problem : an efficient simulation algorithm", J. Opt. Theor. Appl. **45**, 41 (1985).

[71] L. Verlet, "Computer "experiments" on classical fluids. I. Thermodynamical properties of Lennard-Jones molecules", Phys. Rev. **159**, 159 (1967).

[72] K. Jackson, M. Horoi, I. Chaudhuri, T. Frauenheim, and A. Shvartsburg, "Unraveling the shape transformation in silicon clusters", Phys. Rev. Lett. **93**, 013401 (2004).

[73] M. Yang, K. A. Jackson, C. Koehler, T. Frauenheim, and J. Jellinek, "Structure and shape variations in intermediate-size copper clusters.", J. Chem. Phys. **124**, 024308 (2006).

[74] H. Jónsson, G. Mills, and K. W. Jacobsen, *Classical and quantum dynamics in condensed phase simulations - proceedings of the international school of physics* (World Scientific Publishing Co. Pte. Ltd., 1998), pp. 385–404.

[75] H. Eyring, "The activated complex in chemical reactions", J. Chem. Phys. **3**, 107 (1935).

[76] D. Sheppard, R. Terrell, and G. Henkelman, "Optimization methods for finding minimum energy paths.", J. Chem. Phys. **128**, 134106 (2008).

[77] J. C. Polanyi, "Location of energy barriers. I. Effect on the dynamics of reactions A + BC", J. Chem. Phys. **51**, 1439 (1969).

[78] R. Ferrando, J. Jellinek, and R. L. Johnston, "Nanoalloys: from theory to applications of alloy clusters and nanoparticles.", Chem. Rev. **108**, 845 (2008).

[79] C. Mihut, C. Descorme, D. Duprez, and M. D. Amiridis, "Kinetic and spectroscopic characterization of cluster-derived supported Pt-Au catalysts", J. Catal. **212**, 125 (2002).

[80] M. Schrinner, S. Proch, Y. Mei, R. Kempe, N. Miyajima, and M. Ballauff, "Stable bimetallic Gold-Platinum nanoparticles immobilized on spherical polyelectrolyte brushes: synthesis, characterization, and application for the oxidation of alcohols", Adv. Mater. **20**, 1928 (2008).

[81] Z. Peng and H. Yang, "PtAu bimetallic heteronanostructures made by post-synthesis modification of Pt-on-Au nanoparticles", Nano Res. **2**, 406 (2009).

[82] Y. Lou, M. M. Maye, L. Han, J. Luo, and C.-J. Zhong, "Gold-platinum alloy nanoparticle assembly as catalyst for methanol electrooxidation", Chem. Comm. **2001**, 473 (2001).

[83] J. Luo, P. N. Njoki, Y. Lin, D. Mott, L. Wang, and C.-J. Zhong, "Characterization of carbon-supported AuPt nanoparticles for electrocatalytic methanol oxidation reaction.", Langmuir **22**, 2892 (2006).

[84] P. Hernandez-Fernandez, S. Rojas, P. Ocon, J. Gomez de la Fuente, J. San Fabian, J. Sanza, M. Pena, F. Garcia-Garcia, P. Terreros, and J. Fierro, "Influence of the preparation route of bimetallic Pt-Au nanoparticle electrocatalysts for the oxygen reduction reaction", J. Phys. Chem. C **111**, 2913 (2007).

[85] D. Mott, J. Luo, P. Njoki, Y. Lin, L. Wang, and C. Zhong, "Synergistic activity of gold-platinum alloy nanoparticle catalysts", Catal. Today **122**, 378 (2007).

[86] J. Zhang, H. Ma, D. Zhang, P. Liu, F. Tian, and Y. Ding, "Electrocatalytic activity of bimetallic platinum-gold catalysts fabricated based on nanoporous gold.", en, Phys. Chem. Chem. Phys. **10**, 3250 (2008).

[87] G. Selvarani, S. V. Selvaganesh, S. Krishnamurthy, G. V. M. Kiruthika, P. Sridhar, S. Pitchumani, and A. K. Shukla, "A methanol-tolerant carbon-supported Pt-Au alloy cathode catalyst for direct methanol fuel cells and its evaluation by DFT", J. Phys. Chem. C **113**, 7461 (2009).

[88] D. F. Yancey, E. V. Carino, and R. M. Crooks, "Electrochemical synthesis and electrocatalytic properties of Au@Pt dendrimer-encapsulated nanoparticles.", J. Am. Chem. Soc. **132**, 10988 (2010).

[89] B. Du, O. Zaluzhna, and Y. J. Tong, "Electrocatalytic properties of Au@Pt nanoparticles: effects of Pt shell packing density and Au core size.", Phys. Chem. Chem. Phys. **13**, 11568 (2011).

[90] L. Kuai, B. Geng, S. Wang, and Y. Sang, "A general and high-yield galvanic displacement approach to Au-M (M = Au, Pd, and Pt) core-shell nanostructures with porous shells and enhanced electrocatalytic performances.", Chem. Eur. J. **18**, 9423 (2012).

[91] C. Damle, K. Biswas, and M. Sastry, "Synthesis of Au-core/Pt-shell nanoparticles within thermally evaporated fatty amine films and their low-temperature alloying", Langmuir **17**, 7156 (2001).

[92] S. Suzuki, T. Suzuki, Y. Tomita, M. Hirano, K.-I. Okazaki, S. Kuwabata, and T. Torimoto, "Compositional control of AuPt nanoparticles synthesized in ionic liquids by the sputter deposition technique", CrystEngComm **14**, 4922 (2012).

[93] J. Luo, M. M. Maye, V. Petkov, N. N. Kariuki, L. Wang, P. Njoki, D. Mott, Y. Lin, and C.-J. Zhong, "Phase properties of carbon-supported Gold-Platinum nanoparticles with different bimetallic compositions", Chem. Mater. **17**, 3086 (2005).

[94] L. Leppert and S. Kümmel, "The electronic structure of Gold-Platinum nanoparticles: Collecting clues for why they are special", J. Phys. Chem. C **115**, 6694 (2011).

[95] X. J. Kuang, X. Q. Wang, and G. B. Liu, "Structural, electronic and magnetic properties of Au_nPt (n = 1–12) clusters in comparison with corresponding pure Au_{n+1} (n = 1–12) clusters", Eur. Phys. J. D **63**, 111 (2011).

[96] D. T. Tran and R. L. Johnston, "Study of 40-atom Pt-Au clusters using a combined empirical potential-density functional approach", Proc. R. Soc. A **467**, 2004 (2011).

[97] S. J. Wang, X. Y. Kuang, C. Lu, Y. F. Li, and Y. R. Zhao, "Geometries, stabilities, and electronic properties of Pt-group-doped gold clusters, their relationship to cluster size, and comparison with pure gold clusters.", Phys. Chem. Chem. Phys. **13**, 10119 (2011).

[98] N. Braidy, G. R. Purdy, and G. A. Botton, "Equilibrium and stability of phase-separating Au-Pt nanoparticles", Acta Mater. **56**, 5972 (2008).

[99] H. B. Liu, U. Pal, and J. A. Ascencio, "Thermodynamic stability and melting mechanism of bimetallic Au-Pt nanoparticles", J. Phys. Chem. C **112**, 19173 (2008).

[100] Z. Yang, X. Yang, and Z. Xu, "Molecular Dynamics Simulation of the Melting Behavior of Pt-Au Nanoparticles with Core-Shell Structure", J. Phys. C **112**, 4937 (2008).

[101] B. H. Morrow and A. Striolo, "Supported bimetallic Pt-Au nanoparticles: Structural features predicted by molecular dynamics simulations", Phys. Rev. B **81**, 155437 (2010).

[102] A. Logsdail, L. O. Paz-Borbón, and R. L. Johnston, "Structures and stabilities of Platinum-Gold nanoclusters", J. Comp. Theo. Nano. **6**, 857 (2009).

[103] C. Song, Q. Ge, and L. Wang, "DFT studies of Pt/Au bimetallic clusters and their interactions with the CO molecule.", J. Phys. Chem. B **109**, 22341 (2005).

[104] W. Q. Tian, M. Ge, F. Gu, T. Yamada, and Y. Aoki, "Binary clusters AuPt and Au6Pt: structure and reactivity within density functional theory.", J. Phys. Chem. A **110**, 6285 (2006).

[105] B. Hammer and J. K. Norskov, "Why gold is the noblest of all metals", Nature **376**, 238 (1995).

[106] M. J. Piotrowski, P. C. Piquini, and J. Da Silva, "Platinum-Based Nanoalloys PtTM (TM = Co, Rh, Au): A Density Functional Theory Investigation", J. Phys. Chem. C **116**, 18432 (2012).

[107] L. Kesavan, R. Tiruvalam, M. H. Ab Rahim, M. I. bin Saiman, D. I. Enache, R. L. Jenkins, N. Dimitratos, J. A. Lopez-Sanchez, S. H. Taylor, D. W. Knight, C. J. Kiely, and G. J. Hutchings, "Solvent-free oxidation of primary carbon-hydrogen bonds in toluene using Au-Pd alloy nanoparticles.", Science **331**, 195 (2011).

[108] J. S. Jirkovský, I. Panas, E. Ahlberg, M. Halasa, S. Romani, and D. J. Schiffrin, "Single atom hot-spots at Au-Pd nanoalloys for electrocatalytic H_2O_2 production.", J. Am. Chem. Soc. **133**, 19432 (2011).

[109] L. Leppert, "Untersuchung der geometrischen und elektronischen Struktur von Au-Pt Nanopartikeln", Diploma thesis (University of Bayreuth, 2009).

[110] P. Gruene, D. M. Rayner, B. Redlich, A. F. G. van der Meer, J. T. Lyon, G. Meijer, and A. Fielicke, "Structures of neutral Au_7, Au_{19}, and Au_{20} clusters in the gas phase.", Science **321**, 674 (2008).

[111] D. J. Wales, J. P. K. Doye, A. Dullweber, M. P. Hodges, F. Y. Naumkin, F. Calvo, J. Hernández-Rojas, and T. F. Middleton, *The Cambridge Cluster Database*.

[112] W. D. Knight, K. Clemenger, W. A. de Heer, W. A. Saunders, M. Y. Chou, and M. L. Cohen, "Electronic shell structure and abundances of sodium Clusters", Phys. Rev. Lett. **52**, 2141 (1984).

[113] T. Martin, "Shells of atoms", Phys. Rep. **273**, 199 (1996).

[114] S. Kümmel, M. Brack, and P.-G. Reinhard, "Ionic and electronic structure of sodium clusters up to N=59", Phys. Rev. B **62**, 7602 (2000).

[115] M. O. Pedersen, S. Helveg, A. Ruban, I. Stensgaard, and F. Besenbacher, "How a gold substrate can increase the reactivity of a Pt overlayer", Surf. Sci. **426**, 395 (1999).

[116] L. Leppert, R. Q. Albuquerque, and S. Kümmel, "Gold-platinum alloys and Vegard's law on the nanoscale", Phys. Rev. B **86**, 241403(R) (2012).

[117] L. Vegard, "Die Konstitution der Mischkristalle und die Raumfüllung der Atome", Z. Phys. **5**, 17 (1921).

[118] B. E. Warren, *X-ray diffraction* (Addison-Wesley Publishing Company, 1969).

[119] P. Debye, "Zerstreuung von Röntgenstrahlen", Ann. Phys. **351**, 809 (1915).

[120] I. Waller, "Zur Frage der Einwirkung der Wärmebewegung auf die Interferenz von Röntgenstrahlen", Z. Phys. **17**, 398 (1923).

[121] A. P. Sutton and J. Chen, "Long-range Finnis-Sinclair potential", Phil. Mag. Lett. **61**, 139 (1990).

[122] S. J. Mejia-Rosales, C. Fernandez-Navarro, E. Perez-Tijerina, J. M. Montejano-Carrizales, and M. Jose-Yacaman, "Two-stage melting of Au-Pd nanoparticles", J. Phys. Chem. B **110**, 12884 (2006).

[123] S. K. R. S. Sankaranarayanan, V. R. Bhethanabotla, and B. Joseph, "Molecular dynamics simulation study of the melting of Pd-Pt nanoclusters", Phys. Rev. B **71**, 195415 (2005).

[124] Z. Yang, X. Yang, Z. Xu, and S. Liu, "Structural evolution of Pt-Au nanoalloys during heating process: comparison of random and core-shell orderings.", Phys. Chem. Chem. Phys. **11**, 6249 (2009).

[125] D. J. Evans and G. P. Morriss, "Non-Newtonian molecular dynamics", Comp. Phys. Rep. **1**, 297 (1984).

[126] W. Smith and T. R. Forester, "DL_POLY_2.0: a general-purpose parallel molecular dynamics simulation package.", J. Mol. Graph. **14**, 136 (1996).

[127] A. J. C. Wilson and E. Prince, eds., *International tables for x-ray crystallography vol. iii*, 2nd (Kluwer Academic Publishers, Dordrecht, Boston, London, 1999), p. 556.

[128] S. Kümmel, J. Akola, and M. Manninen, "Thermal expansion in small metal clusters and its impact on the electric polarizability", Phys. Rev. Lett. **84**, 3827 (2000).

[129] V. Petkov, B. N. Wanjala, R. Loukrakpam, J. Luo, L. Yang, C.-J. Zhong, and S. Shastri, "Pt-au alloying at the nanoscale.", Nano Lett. **12**, 4289 (2012).

[130] P. Sabatier, "Hydrogenations et deshydrogenations par catalyse", Ber. Deutsch. Chem. Gesell. **44**, 1984 (1911).

[131] J. K. Norskov, T. Bligaard, J. Rossmeisl, and C. H. Christensen, "Towards the computational design of solid catalysts", Nat. Chem. **1**, 37 (2009).

[132] J. Kaiser, L. Leppert, H. Welz, F. Polzer, S. Wunder, N. Wanderka, M. Albrecht, T. Lunkenbein, J. Breu, S. Kümmel, Y. Lu, and M. Ballauff, "Catalytic activity of nanoalloys from gold and palladium.", Phys. Chem. Chem. Phys. **14**, 6487 (2012).

[133] W. D. Knight, K. Clemenger, W. A. de Heer, and W. A. Saunders, "Polarizability of alkali clusters", Phys. Rev. B **31**, 2539 (1985).

[134] J. Bowlan, A. Liang, and W. A. de Heer, "How metallic are small sodium clusters?", Phys. Rev. Lett. **106**, 043401 (2011).

[135] L. Kronik, I. Vasiliev, and J. R. Chelikowsky, "Ab initio calculations for structure and temperature effects on the polarizabilities of Na_n ($n \leq 20$) clusters", Phys. Rev. B **62**, 9992 (2000).

[136] P. W. Anderson, "Localized magnetic states in metals", Phys. Rev. **124**, 41 (1961).

[137] D. M. Newns, "Self-consistent model of hydrogen chemisorption", Phys. Rev. **178**, 1123 (1969).

[138] B. Hammer and J. K. Norskov, "Electronic factors determining the reactivity of metal surfaces", Surf. Sci. **343**, 211 (1995).

[139] R. S. Mulliken, "Electronic Population Analysis on LCAO-MO Molecular Wave Functions", J. Chem. Phys. **23**, 1833 (1955).

[140] A. M. Köster, P. Calaminici, E. Orgaz, D. R. Roy, J. U. Reveles, and S. N. Khanna, "On the ground state of Pd_{13}.", J. Am. Chem. Soc. **133**, 12192 (2011).

[141] I. V. Yudanov and K. M. Neyman, "Stabilization of Au at edges of bimetallic PdAu nanocrystallites.", Phys. Chem. Chem. Phys. **12**, 5094 (2010).

[142] F. Pittaway, L. O. Paz-Borbon, R. L. Johnston, H. Arslan, R. Ferrando, C. Mottet, G. Barcaro, and A. Fortunelli, "Theoretical Studies of Palladium-Gold Nanoclusters: Pd-Au Clusters with up to 50 Atoms", J. Phys. Chem. C **113**, 9141 (2009).

[143] H. Häkkinen, S. Abbet, A. Sanchez, U. Heiz, and U. Landman, "Structural, electronic, and impurity-doping effects in nanoscale chemistry: supported gold nanoclusters.", Ang. Chem. Int. Ed. **42**, 1297 (2003).

[144] R. Gaspari, C. Pignedoli, R. Fasel, M. Treier, and D. Passerone, "Atomistic insight into the adsorption site selectivity of stepped Au(111) surfaces", Phys. Rev. B **82**, 041408 (2010).

[145] S. Wunder, Y. Lu, M. Albrecht, and M. Ballauff, "Catalytic activity of faceted gold nanoparticles studied by a model reaction: evidence for substrate-induced surface restructuring", ACS Catal. **1**, 908 (2011).

[146] E. C. Beret, L. M. Ghiringhelli, and M. Scheffler, "Free gold clusters: beyond the static, monostructure description", Faraday Discuss. **152**, 153 (2011).

[147] H. Ohno, A. Shen, F. Matsukura, A. Oiwa, A. Endo, S. Katsumoto, and Y. Iye, "(Ga,Mn)As: A new diluted magnetic semiconductor based on GaAs", Appl. Phys. Lett. **69**, 363 (1996).

[148] G. W. Ludwig and H. H. Woodbury, "Electron Spin Resonance in Semiconductors", Solid State Phys. **13**, edited by H. Ehrenreich, F. Seitz, and D. Turnbull, 223 (1962).

[149] F. Beeler, O. K. Andersen, and M. Scheffler, "Electronic and magnetic structure of 3d-transition-metal point defects in silicon calculated from first principles", Phys. Rev. B **41**, 1603 (1990).

[150] H. Wu, P. Kratzer, and M. Scheffler, "Density-Functional Theory study of half-metallic heterostructures: interstitial Mn in Si", Phys. Rev. Lett. **98**, 117202 (2007).

[151] Z. Zhang, B. Partoens, K. Chang, and F. Peeters, "First-principles study of transition metal impurities in Si", Phys. Rev. B **77**, 1–8 (2008).

[152] M. Shaughnessy, C. Y. Fong, R. Snow, K. Liu, J. E. Pask, and L. H. Yang, "Origin of large moments in Mn_xSi_{1-x} at small x", Appl. Phys. Lett. **95**, 022515 (2009).

[153] F. Küwen, R. Leitsmann, and F. Bechstedt, "Mn and Fe doping of bulk Si: Concentration influence on electronic and magnetic properties", Phys. Rev. B **80**, 045203 (2009).

[154] L. Zeng, J. Cao, E. Helgren, J. Karel, E. Arenholz, L. Ouyang, D. Smith, R. Wu, and F. Hellman, "Distinct local electronic structure and magnetism for Mn in amorphous Si and Ge", Phys. Rev. B **82**, 165202 (2010).

[155] X. Huang, A. Makmal, J. Chelikowsky, and L. Kronik, "Size-dependent spintronic properties of dilute magnetic semiconductor nanocrystals", Phys. Rev. Lett. **94**, 236801 (2005).

[156] R. Leitsmann, C. Panse, F. Küwen, and F. Bechstedt, "Ab initio characterization of transition-metal-doped Si nanocrystals", Phys. Rev. B **80**, 104412 (2009).

[157] X. Chen, X. Pi, and D. Yang, "Silicon nanocrystals doped with substitutional or interstitial manganese", Appl. Phys. Lett. **99**, 193108 (2011).

[158] S. Khanna, B. Rao, and P. Jena, "Magic numbers in metallo-inorganic clusters: Chromium encapsulated in Silicon cages", Phys. Rev. Lett. **89**, 016803 (2002).

[159] W. Zheng, J. M. Nilles, D. Radisic, and K. H. Bowen, "Photoelectron spectroscopy of chromium-doped silicon cluster anions.", J. Chem. Phys. **122**, 071101 (2005).

[160] L.-J. Guo, G.-F. Zhao, Y.-Z. Gu, X. Liu, and Z. Zeng, "Density-functional investigation of metal-silicon cage clusters MSi_n (M=Sc, Ti, V, Cr, Mn, Fe, Co, Ni, Cu, Zn; n=8-16)", Phys. Rev. B **77**, 195417 (2008).

[161] V. T. Ngan, E. Janssens, P. Claes, J. T. Lyon, A. Fielicke, M. T. Nguyen, and P. Lievens, "High magnetic moments in Manganese-doped Silicon clusters.", Chem. Eur. J. **18**, 15788 (2012).

[162] D. Palagin and K. Reuter, "Evaluation of endohedral doping of hydrogenated Si fullerenes as a route to magnetic Si building blocks", Phys. Rev. B **86**, 045416 (2012).

[163] F. Malet and P. Gori-Giorgi, "Strong correlation in Kohn-Sham Density Functional Theory", Phys. Rev. Lett. **109**, 246402 (2012).

[164] O. V. Gritsenko, P. R. T. Schipper, and E. J. Baerends, "Exchange and correlation energy in density functional theory: Comparison of accurate density functional theory quantities with traditional Hartree-Fock based ones and generalized gradient approximations for the molecules Li_2, N_2, F_2", J. Chem. Phys. **107**, 5007 (1997).

[165] P. Mori-Sánchez, A. J. Cohen, and W. Yang, "Many-electron self-interaction error in approximate density functionals.", J. Chem. Phys. **125**, 201102 (2006).

[166] J. P. Perdew, R. G. Parr, M. Levy, and J. L. Balduz, "Density Functional Theory for fractional particle number: Derivative Discontinuities of the Energy", Phys. Rev. Lett. **4**, 1691 (1982).

[167] J.-D. Chai and P.-T. Chen, "Restoration of the derivative discontinuity in Kohn-Sham Density Functional Theory: an efficient scheme for energy gap correction", Phys. Rev. Lett. **110**, 033002 (2013).

[168] A. J. Cohen, P. Mori-Sánchez, and W. Yang, "Challenges for Density Functional Theory", Chem. Rev. **112**, 289 (2012).

[169] K. Hirsch, *Private communication*, 2013.

[170] K. Hirsch, J. T. Lau, P. Klar, A. Langenberg, J. Probst, J. Rittmann, M. Vogel, V. Zamudio-Bayer, T. Möller, and B. von Issendorff, "X-ray spectroscopy on size-selected clusters in an ion trap: from the molecular limit to bulk properties", J. Phys. B **42**, 154029 (2009).

[171] Ph.D. thesis of V. Zamudio-Bayer at Technische Universität Berlin.

[172] B. T. Thole, P. Carra, F. Sette, and G. van der Laan, "X-Ray Circular Dichroism as a probe of orbital magnetization", Phys. Rev. Lett. **68**, 1943 (1992).

[173] P. Carra, B. T. Thole, A. Massimo, X. X. Wang, and M. Altarelli, "X-Ray Circular Dichroism and local magnetic fields", Phys. Rev. Lett. **70**, 694 (1993).

[174] Y. Shao, L. F. Molnar, Y. Jung, J. Kussmann, C. Ochsenfeld, S. T. Brown, A. T. B. Gilbert, and et al., "Advances in methods and algorithms in a modern quantum chemistry program package", Phys. Chem. Chem. Phys. **8**, 3172 (2006).

[175] H. Wu, M. Hortamani, P. Kratzer, and M. Scheffler, "First-Principles study of ferromagnetism in epitaxial Si-Mn thin films on Si(001)", Phys. Rev. Lett. **92**, 237202 (2004).

[176] Q. Wang, Q. Sun, J. Z. Yu, Y. Hashi, and Y. Kawazoe, "First-principles studies on magnetism of Ni clusters coated and alloyed with Pd", Phys. Lett. A **267**, 394 (2000).

[177] A. Chutia and M. Tokuyama, "Orbital interaction and local stability of Ni substituted Pd nanoalloys", Chem. Phys. Lett. **515**, 96 (2011).

[178] V. Forster, "Struktur und Eigenschaften von Nickel-Palladium Clustern", Bachelor thesis (University of Bayreuth, 2012).

[179] T. Aschebrock, "Konstruktionsprinzip und Test von first-principles Pseudopotentialen", Bachelor thesis (University of Bayreuth, 2012).

[180] J. Hermannsdörfer, M. Friedrich, N. Miyajima, R. Q. Albuquerque, S. Kümmel, and R. Kempe, "Ni/Pd@MIL-101: Synergetische Katalyse mit kavitätenkonformen Ni/Pd-Nanopartikeln", Ang. Chem. **124**, 11640 (2012).

[181] P.-P. Fang, A. Jutand, Z.-Q. Tian, and C. Amatore, "Au-Pd core-shell nanoparticles catalyze Suzuki-Miyaura reactions in water through Pd leaching", Ang. Chem. Int. Ed. **123**, 12184 (2011).

[182] S. Nosé, "A unified formulation of the constant temperature molecular dynamics methods", J. Chem. Phys. **81**, 511 (1984).

[183] W. G. Hoover, "Canonical dynamics: Equilibrium phase-space distributions", Phys. Rev. A **31**, 1695 (1985).

[184] Turbomole, V6.4.2 (2012).

[185] S. Grimme, "Accurate description of van der Waals complexes by density functional theory including empirical corrections", J. Comp. Chem. **25**, 1463 (2004).

[186] M. Faraday, "The Bakerian Lecture: Experimental relations of Gold (and other metals) to light", Phil. Trans. R. Soc. Lond. **147**, 145 (1857).

[187] U. Kreibig and M. Vollmer, *Optical Properties of Metal Clusters*, edited by P. Toennies (Springer-Verlag, Berlin, Heidelberg, 1995).

[188] G. Mie, "Beiträge zur Optik trüber Medien, speziell kolloidaler Metalllösungen", Ann. Phys. **25** (1908).

[189] E. D. Palik, *Handbook of Optical Constants of Solids* (Academic Press, New York, 1985).

[190] J. H. Weaver, "Optical properties of Rh, Pd, Ir, and Pt", Phys. Rev. B **11**, 1416 (1975).

[191] A. Henglein, "Preparation and optical absorption spectra of $Au_{core}Pt_{shell}$ and $Pt_{core}Au_{shell}$ colloidal nanoparticles in aqueous solution", J. Phys. Chem. B **104**, 2201 (2000).

[192] L. M. Liz-Marzan and A. P. Philipse, "Stable hydrosols of metallic and bimetallic nanoparticles immobilized on imogolite fibers", J. Phys. Chem. **99**, 15120 (1995).

[193] M. Gaudry, E. Cottancin, M. Pellarin, J. Lermé, L. Arnaud, J. Huntzinger, J. Vialle, M. Broyer, J. Rousset, M. Treilleux, and P. Mélinon, "Size and composition dependence in the optical properties of mixed (transition metal/noble metal) embedded clusters", Phys. Rev. B **67**, 155409 (2003).

[194] A. L. Aden and M. Kerker, "Scattering of electromagnetic waves from two concentric spheres", J. Appl. Phys. **22**, 1242 (1951).

Acknowledgment

I thank the following people for their help and support with this thesis:

Stephan Kümmel. I have it on good authority, that ≈ 8.23 out of 10 of my sentences during an average week in the last couple of years started with "Stephan says that...". I thank him for the most inspiring quantum mechanics lecture of all time (in my second year of undergraduate study), for convincing me to stay just a little bit longer in Bayreuth (in my third and fifth year) and for all the advice, discussions and patience during the last years that were of inestimable value to me.

Rodrigo Albuquerque, who has been incredibly patient in performing yet another molecular dynamics run. I thank him for inspiring discussions about the bimetallic effect in Au-Pt nanoalloys, valuable insight into molecular dynamics simulations and his indestructible enthusiasm for our project.

Adam Foster, for always lending a hand when it came to Nudged Elastic Band calculations. I enjoyed his and his group's hospitality in Tampere, Finland, for six winterly weeks and learned a lot about VASP, transition state search and (not so) Finnish beer.

Tobias Lau and **Vicente Zamudio-Bayer**, for countless physics discussions, the most amusing science gossip, a desk in Tobias' office whenever I traveled to Berlin, for more support than I ever expected to receive and for letting me convince them that DFT can actually be a lot of fun.

Andreas Karolewski has been my best friend for the last 8 years and the best office vis-à-vis one could wish for. From physics to politics and especially "beyond"; there is little that Andreas does not know about. He always impressed me with his great curiosity and stamina. Besides, he's just pretty cool.

Matthias Dauth, **Tobias Schmidt** and all the other members and alumni of the **Kümmel group**. I thank you for making these last years most exciting and instructive but first and foremost for making them an awful lot of fun. Furthermore, I thank Andreas, Matthias and Tobias for their thorough proof-reading of parts of this thesis.

Markus Hilt, **Bernhard Winkler** and **Monika Birkelbach** for technical and administrative support whenever it was needed.

My family, but especially **Karena** and **Jörg**, the second physicist in the family, who aroused an early interest for physics in me.

Konstantin Hirsch, for patient proof-reading of this thesis and for many helpful comments, advice and discussion. Most of all, I want to thank him for proving an easy and a difficult thing to me, that changed my life in countless ways: 1. Only a physicist can be a physicist. 2. All can be well.

For financial and intellectual support I am grateful to the **SFB 840** of the DFG, the **Wilhelm und Else Heraeus Stiftung** and the **Elite Study Programme Macromolecular Science**.

Erklärung

Hiermit erkläre ich, dass ich die vorliegende Arbeit selbstständig verfasst und keine anderen als die angegebenen Quellen und Hilfsmittel verwendet habe. Die Arbeit wurde weder in gleicher noch in ähnlicher Form bei anderen Prüfungsbehörden zur Erlangung eines akademischen Grades vorgelegt.

Ich erkläre, dass ich keine Hilfe von gewerblichen Promotionsberatern bzw. -vermittlern oder ähnlichen Dienstleistern in Anspruch genommen habe und auch nicht beabsichtige diese zukünftig in Anspruch zu nehmen.

Weiterhin erkläre ich, dass ich bisher keinen anderweitigen Promotionsversuch unternommen habe.

Bayreuth, den 29. Mai 2013 Linn Leppert